KONRAD GILBERT HEINRICH VIEBAHN

QUASICRYSTALLINE OPTICAL LATTICES FOR ULTRACOLD ATOMS

THIS DISSERTATION IS SUBMITTED FOR THE DEGREE OF DOCTOR OF PHILOSOPHY.

TRINITY COLLEGE, OCTOBER 2018

CAVENDISH LABORATORY, UNIVERSITY OF CAMBRIDGE

“THE MOST ESSENTIAL PART OF A LIVING CELL – THE CHROMOSOME FIBRE – MAY SUITABLY BE CALLED AN APERIODIC CRYSTAL. IN PHYSICS WE HAVE DEALT HITHERTO ONLY WITH PERIODIC CRYSTALS. TO A HUMBLE PHYSICIST’S MIND, THESE ARE VERY INTERESTING AND COMPLICATED OBJECTS; THEY CONSTITUTE ONE OF THE MOST FASCINATING AND COMPLEX MATERIAL STRUCTURES BY WHICH INANIMATE NATURE PUZZLES HIS WITS. YET, COMPARED WITH THE APERIODIC CRYSTAL, THEY ARE RATHER PLAIN AND DULL. THE DIFFERENCE IN STRUCTURE IS OF THE SAME KIND AS THAT BETWEEN AN ORDINARY WALLPAPER IN WHICH THE SAME PATTERN IS REPEATED AGAIN AND AGAIN IN REGULAR PERIODICITY AND A MASTERPIECE OF EMBROIDERY, SAY A RAPHAEL TAPESTRY, WHICH SHOWS NO DULL REPETITION, BUT AN ELABORATE, COHERENT, MEANINGFUL DESIGN TRACED BY THE GREAT MASTER.”

ERWIN SCHRÖDINGER, “WHAT IS LIFE?”

Declaration

This dissertation is the result of my own work and includes nothing which is the outcome of work done in collaboration except as declared in the Preface and specified in the text.
It is not substantially the same as any that I have submitted, or, is being concurrently submitted for a degree or diploma or other qualification at the University of Cambridge or any other University or similar institution except as declared in the Preface and specified in the text. I further state that no substantial part of my dissertation has already been submitted, or, is being concurrently submitted for any such degree, diploma or other qualification at the University of Cambridge or any other University or similar institution except as declared in the Preface and specified in the text.
This thesis does not exceed the word limit of sixty thousand words, including abstract, tables, footnotes and appendices, set out by the Faculty of Physics and Chemistry.

Abstract

Quasicrystals are long-range ordered and yet non-periodic. This interplay results in a wealth of intriguing physical phenomena, such as the inheritance of topological properties from higher dimensions, self-similarity, and the presence of non-trivial structure on all scales. The concept of aperiodic order has been extensively studied in mathematics and geometry, exemplified by the celebrated Penrose tiling. However, the understanding of physical quasicrystals (the vast majority of them are intermetallic compounds) is still incomplete owing to their complexity, regarding both growth processes and stability.

Ultracold atoms in optical lattices offer an ideal, yet untested environment for investigating quasicrystals. Optical lattices, i.e. standing waves of light, allow the defect-free formation of a large variety of potential landscapes, including quasiperiodic geometries. In recent years, optical lattices have become one of the most successful tools in the large-scale quantum simulation of condensed-matter problems.

This study presents the first experimental realisation of a two-dimensional quasicrystalline potential for ultracold atoms, based on an eightfold symmetric optical lattice. It is aimed at bringing together the fields of ultracold atoms and quasicrystals – and the more general concept of aperiodic order. The first part of this thesis introduces the theoretical aspects of aperiodic order and quasicrystalline structure. The second part comprises a detailed account of the newly designed apparatus that has been used to produce quantum-degenerate gases in quasicrystalline lattices. The third and final part summarises the matter-wave diffraction experiments that have been performed in various lattice geometries. These include one- and two-dimensional simple cubic lattices, one-dimensional quasiperiodic lattices, as well as two-dimensional quasicrystalline lattices. The striking self-similarity of this quasicrystalline structure has been directly observed, in close analogy to Shechtman's very first discovery of quasicrystals using electron diffraction. In addition, an in-depth study of the diffraction dynamics reveals the fundamental differences between periodic and quasicrystalline lattices, in excellent agreement with ab initio theory. The diffraction dynamics on short timescales constitutes a continuous-time quantum walk on a homogeneous four-dimensional tight-binding lattice.

On the one hand, these measurements establish a novel experimental platform for investigating quasicrystals proper. On the other hand, ultracold atoms in quasicrystalline optical lattices are worth studying in their own right: Possible avenues include the observation many-body localisation and Bose glasses, as well as the creation of topologically non-trivial systems in higher dimensions.

Contents

Introduction: quasicrystalline potentials for ultracold atoms

Quasicrystals are long-range ordered without being periodic [1–4]. Their order manifests itself in sharp diffraction peaks, exactly as in their periodic counterparts. However, diffraction patterns from quasicrystals often reveal rotational symmetries, most notably fivefold, eightfold, and tenfold, that are incompatible[1] with translational symmetry. Therefore it immediately follows that long-range order in quasicrystals results not from a periodic arrangement of unit cells but from a different paradigm. Quasicrystalline order can be seen as an incommensurate projection of a higher-dimensional periodic lattice; this enables investigation of physics of higher dimensions, in particular in the context of topology [5–7]. For instance, one-dimensional (1D) quasiperiodic models, such as the Fibonacci chain and the Aubry-Andre model, are closely connected to the celebrated two-dimensional Harper model [6].

[1] crystallographically 'forbidden'

An alternative approach to constructing quasicrystals was described by Penrose [8] who discovered a pentagonal tiling. Using a particular set of tiles and associated matching rules[2] it is possible to cover a plane with an infinite tiling, in which non-periodicity is enforced by the matching rules [9]. The fivefold symmetric Penrose tiling and the closely related eightfold symmetric Ammann-Beenker tiling [10] (also called 'octagonal tiling' [9]) have become paradigms of 2D quasicrystals [9, 11]. In addition to their dis allowed rotational symmetries, these tilings have the remarkable feature of being self-similar in both real and reciprocal space [3]. Self-similarity upon scaling in length by a certain factor (the silver mean $1 + \sqrt{2}$ in case of the octagonal tiling) implies that non-trivial structure is present on arbitrarily large scales. Correspondingly, diffraction patterns from quasicrystals display sharp peaks at arbitrarily small momenta.

[2] imagine a puzzle game

To date, quasicrystals have been extensively studied in material science, condensed-matter, and crystallography [11, 12]. Various quasicrystalline model systems have been created, most notably in photonic systems [13] and optical lattices [14–17]. Optical lattices are particularly adept for emulating quasicrystals since high rotational symmetries can easily be imposed [17]. However, this advantage has yet remained unexplored in the field of quantum gases.

Ultracold gases in optical lattices

Quantum gases of neutral atoms are one of today's most exciting experimental frontiers in quantum many-body physics. Sparked by the observation of a quantum phase transition using ultracold atoms in an optical lattice [18] there has been much progress towards Feynman's original proposal of a quantum simulator [19]. A quantum simulator is a machine that solves numerically intractable quantum-mechanical problems[3] by mapping them to another quantum mechanical system with experimentally accessible observables. Quantum gases are ideally suited for this application due to the exquisit control of external parameters, such as dimensionality, type and strength of interaction, and geometry.[4] The current experimental realisations of 'quantum simulators' [20, 21] have implemented a multitude of theoretically relevant models, in which numerical simulations are either very hard or impossible [22–25], particularly in dimensions higher than one.

[3] such as the dynamics of the doped fermionic Hubbard model

[4] both in lattices and in bulk systems

But there is more: quantum simulation is just one interpretation of quantum gas experiments. Ultracold atoms have recently been used to create previously unseen phases of matter, such as supersolids [26, 27] and unitary Bose gases [28]. Quantum gases in lattices offer a controllable and clean environment to probe novel systems, such as Floquet-engineered hamiltonians [29]. Therefore, these novel quantum systems are worth pursuing in their own right and it is expected that they play an important role in future applications of quantum technology [21, 30].

Scope

The experimental apparatus described in this thesis is aimed at bridging the two fields of quantum gases and quasicrystals, thereby creating a new platform to study aperiodic order with ultracold atoms. Drawing from established techniques and concepts in both fields, there are numerous directions in which experimentation can progress. In particular, the ability to create arbitrarily complex quantum systems by employing aperiodic order [31], and the possibility of inheriting topological properties from higher dimensions [6] are most promising.

Outline

This thesis offers a comprehensive review of all experimental methods that were used to create the first quasicrystalline optical lattice for ultracold atoms. A very brief overview of the whole experimental apparatus is given in Chapter 2. The methods chapters focus on initial cooling from room temperature to the µK regime (Chapter 3), reaching quantum degeneracy in the optical dipole trap (Chapter 4), and the setup of the eightfold symmetric optical

lattice (Chapter 5). Afterwards, the main experimental outcomes of this work are discussed in Chapter 6, namely matter-wave experiments. They highlight the self-similarity of our quasicrystalline optical lattice, and its ability to simulate quantum walks in higher dimensions.

Initially, quasicrystals in one and two dimensions will be introduced (Chapter 1), thereby summarising key concepts such as aperiodicity, self-similarity, non-periodic diffraction patterns, the cut-and-project scheme, phasonic excitations and the role of rotational symmetries. The current state-of-the-art in quasicrystal research is reviewed at the end of Chapter 1.

Contributions

The apparatus as it is described in this thesis was jointly designed, implemented, and characterised by the author and Matteo Sbroscia, under supervision of Dr. Ulrich Schneider. Major contributions were made by Dr. Stephen Topliss (electronics engineer), Hendrik von Raven, Oliver Brix, Edward Carter, Max Melchner, Michael Höse, and Jr-Chiun Yu.

1
Quasicrystals and aperiodic order

The aim of this chapter is to provide an accessible introduction to the topic of quasicrystals and the concept of aperiodic order. It will form the theoretical basis for the experimental results (Chapter 6). On the path towards understanding quasicrystals we will follow these steps:

1.1 What is a quasicrystal? The definition of quasicrystals. The notion of aperiodic order.

1.2 A pedagogical example of a one-dimensional quasicrystal: the Fibonacci chain. In this section two important concepts will be introduced: self-similarity, and the cut-and-project method.

1.3 Quasicrystals in two dimensions. Crystallographic restriction and the role of rotational symmetries in quasicrystals. The octagonal aperiodic tiling (or Ammann-Beenker tiling).

1.4 Quasicrystalline materials. What is known about physical quasicrystals? Classification of quasicrystals and open questions in quasicrystal research. What could our experiment contribute to these questions?

1.1 *What is aperiodic order? What is a quasicrystal?*

What is a black hole? What is a magnetic field? What is an atom? Ask these questions to a group of physicists and you will get more or less consistent answers.[1] Of course, the depths of research are always full of intricacies and, consequently, the answers to some of these questions may depend on context. But overall, a quick look into standard literature will bring clarity.

Defining quasicrystals is much trickier. First, this is due to some initial confusion after the discovery of quasicrystals [12]. Second, literature on quasicrystals is scattered over many different fields,[2] including crystallography [11], condensed-matter physics [12], and mathematics [9]. Third, even after 35 years of research on quasicrystals and their descendants, there are still many open questions [11]. Finally, there has been a paradigm shift in the community from 'quasicrystals' to the more general concept of 'aperiodic order' [9, 12]. We will get back to this at the end of the chapter.

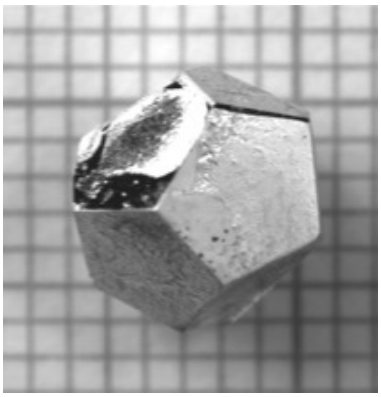

Figure 1.1: Is this a crystal? The image shows a single grain of icosahedral Zn-Mg-Dy. Courtesy M. Feuerbacher, Forschungszentrum Jülich.

[1] If you do not have a group of physicists at hand, Wikipedia will do.

[2] see ref. [9] for a comprehensive list

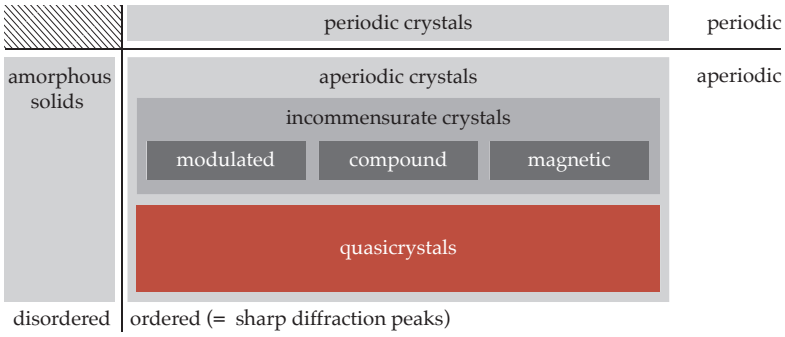

Figure 1.2: Crystallographic definition of crystals and quasicrystals [32]. The discovery of quasicrystals contributed the distinction between periodic and aperiodic crystals to this classification. Up until then order had been thought to be synonymous with periodicity.

Let us start by defining the terms 'crystal' and 'aperiodic crystal' according to the International Union of Crystallography (IUCr) [33, 34].

Definition. *In the following by 'crystal' we mean any solid having an essentially discrete diffraction diagram, and by 'aperiodic crystal' we mean any crystal in which three-dimensional lattice periodicity can be considered to be absent.*

Although the term 'essentially' is deliberately vague,[3] the overall message is clear: long-range order – in this case embodied by crystalline solids – is defined by sharp diffraction peaks. The association of 'order' with 'sharp diffraction peaks' was introduced in the wake of the discovery of quasicrystals, which proved that the previous paradigm ('order ⇔ periodicity') had been false. After some initial debate (see ref. [12] for a review) a paradigm shift took place in the community of crystallography. Nowadays there is broad consensus about the definition of crystals by the existence of sharp diffraction peaks. There can be no doubt that the images shown in Fig. 1.3, which were obtained from a single grain of Zn-Mg-Dy (Fig. 1.1), are indeed signatures of a type of crystal.

However, the image in Fig. 1.3C displays a tenfold rotational symmetry which is forbidden for periodic crystals.[4] Therefore this material must be aperiodic *and* ordered. We will expand more on the notion of aperiodic order in section 1.2.

What about quasicrystals then? Are they the same as aperiodic ordered structures? The IUCr dictionary offers two different definitions of a quasicrystal, with a varying degree of overlap with the class of aperiodic ordered materials [32].

Definition A. *A quasicrystal is an aperiodic crystal that is not an incommensurate modulated crystal, nor an incommensurate composite crystal. Often, quasicrystals have crystallographically 'forbidden' symmetries. These are rotations of order different from 2, 3, 4 and 6.*

This definition explicitly sets quasicrystals apart from two other classes of aperiodic crystals, namely 'incommensurate modulated crystals' and 'incommensurate composite crystals', as shown in Fig. 1.2. Incommensurate modulated crystals represent crystals with reciprocal lattices that include at least two incommensurate wave vectors [36]. Incommensurate composite crystals are

[3] "*The word essentially means that most of the intensity of the diffraction is concentrated in relatively sharp Bragg peaks, besides the always present diffuse scattering.*" [34, 35]

[4] we will prove this later

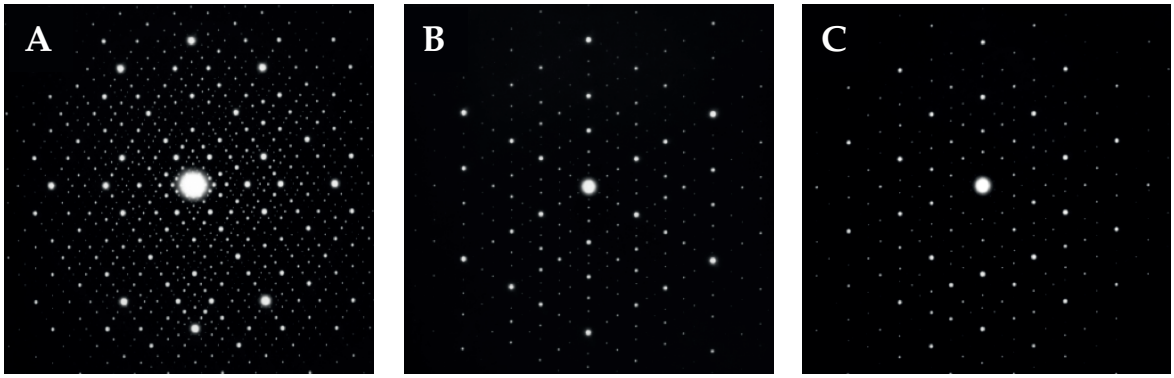

Figure 1.3: Electron diffraction images of icosahedral Zn-Mg-Dy (Fig. 1.1) along a twofold- (**A**), threefold- (**B**), and fivefold- (**C**) rotationally symmetric axis. Note that the patterns in (**B**) and (**C**) appear to be sixfold- and tenfold-symmetric, respectively. This is a consequence of the diffraction intensity being proportional to the square of the modulus of the structure factor, making reflections with opposite indices (h, k, l) and $(\bar{h}, \bar{k}, \bar{l})$ appear equally strong. This effect is known as 'Friedel's law' [38]. Images: courtesy M. Feuerbacher, Forschungszentrum Jülich.

structures made of at least two subcrystals with incommensurate lattice vectors [37]. According to this definition, the set of quasicrystals and the set of incommensurate crystals (ICs) are disjoint, both being subsets of the set of aperiodic crystals. There are overlaps between the subsets within ICs (and a third kind of ICs, namely 'incommensurate magnetic structures' in which the size of the structural unit cell is incommensurate with the size of the magnetic unit cell). However, the distinction between ICs and quasicrystals in the one-dimensional case is non-trivial, as we will see later by studying diffraction patterns of 1D aperiodic lattices. Therefore the IUCr offers an alternative definition [32, 35]:

Definition B. *The term quasicrystal stems from the property of quasiperiodicity observed for the first alloys found with forbidden symmetries. Therefore, the alternative definition is: a quasicrystal is an aperiodic crystal with diffraction peaks that may be indexed by n integral indices, where n is a finite number, larger than the dimension of the space (in general). This definition is similar to that of aperiodic crystal.*

'Indexing' here means that the position of each diffraction peak can be written as a unique set of integers[5] times a set of reciprocal lattice vectors. In other words, it means 'count the minimum number of integers you need to uniquely identify all the diffraction peaks of a D-dimensional crystal. If this number is finite and larger than D, then the crystal is a quasicrystal.' This classification is summarised in table 1.1. Here there is essentially no distinction between quasicrystals and aperiodic crystals because the index counting method does not distinguish these cases. This definition of quasicrystals is more mathematical and, consequently, slightly

[5] or a single integer in periodic 1D lattices

# integers needed (n)			class of material
n uncountably infinite		→	disordered, amorphous
n countably infinite		→	almost periodic crystal
n finite	$n > D$	→	aperiodic crystal
	$n = D$	→	periodic crystal

Table 1.1: Alternative classification of crystals according to the number n of integers needed to index the diffraction peaks, or equivalently, the minimum number of (Fourier-)components needed to write the atomic density distribution as a superposition of plane waves. The class of 'almost periodic crystals' is largely theoretical, in analogy with the mathematical class of 'almost periodic functions' [39], since they have not been observed in experiments [35].

more tangible, compared to definition A. It has a certain appeal since it lists periodic crystals as natural 'extension' of aperiodic crystals in the case $n = D$ (number of integers needed to index the diffraction pattern equal to the spatial dimension of the crystal).

Note that there is no distinction between the terms 'quasicrystal' and 'quasiperiodic crystal'; the two can be used interchangeably [35, 40]. However, the adjective 'quasiperiodic' often refers to a special class of mathematical functions called 'almost periodic functions' [11, 39, 41].[6]

[6] The definition of almost periodic functions goes back the Danish mathematician Harald Bohr, brother of Niels Bohr, and winner of an olympic silver medal in football (1908).

The question of rotational symmetries is a subtle one because neither of the definitions list them as a necessary requirement. However, due to crystallographic restriction (section 1.3) high rotational symmetries in ordered structures are a sufficient criterion for classification as quasicrystal. For simplicity, we can assume two-dimensional quasicrystals to have 'forbidden' rotational symmetries in this work[7] since the eightfold optical lattice obviously fulfils the criterion. Since the precise definition of quasicrystals is tricky, we shall simply use the term 'quasicrystal' for ordered structures *with* forbidden symmetries,[8] whereas the broader concept of 'aperiodic order' shall include quasiperiodic structures *without* forbidden symmetries, as well as quasicrystals.

[7] thereby ignoring the existence of a few aperiodic structures without forbidden symmetry [11, 12]

[8] and also for 1D quasiperiodic structures, for historical reasons

In order to build some intuition on these abstract definitions of quasicrystals, we will now take the Fibonacci chain as an example. All of the concepts that are introduced in section 1.2 for one dimension will be generalised to two dimensions in section 1.3.

1.2 *Fibonacci chain*

The Fibonacci chain is the archetypical manifestation of aperiodic order[9] in one dimension. We construct the Fibonacci chain by repeatedly acting with the following substitution rule

[9] and quasicrystallinity

$$\begin{aligned} L &\to LS \\ S &\to L \end{aligned} \tag{1.1}$$

on a 'seed' letter L. Equation 1.1 means that one letter L is to be replaced by a sequence of two letters (LS). An alternative formulation of the substitution rule is

$$\begin{pmatrix} L \\ S \end{pmatrix} \to \begin{pmatrix} 1 & 1 \\ 1 & 0 \end{pmatrix} \begin{pmatrix} L \\ S \end{pmatrix} \quad , \tag{1.2}$$

to the same effect that the sum in the matrix multiplication is to be understood as the concatenation of two letters ($L + S \to LS$). This procedure leads to an arbitrarily long sequence of letters

$$L \to LS \to LSL \to LSLLS \to LSLLSLSL \to LSLLSLSLLSLLS \to \dots$$

which is called a Fibonacci chain (or 'Fibonacci word'). In a diagrammatic representation the letters L and S can be understood as long and short line segments, respectively; in this representation the vertices between line segments correspond to lattice points.

The occurrence of S and L letters (N_S and N_L, respectively) after m substitution steps is listed in table 1.2 from which we recognise the famous Fibonacci numbers. We denote the mth Fibonacci number by F_m such that $N_S(m) = F_{m-1}$ and $N_L(m) = F_m$. Moreover, the total number of letters is then $N_{\text{tot}} = N_S(m) + N_L(m) = F_{m+1}$. In the limit of $m \to \infty$ the ratio between two subsequent Fibonacci numbers F_m and F_{m+1} is [12]

$$\lim_{m\to\infty} \frac{F_{m+1}}{F_m} = 1 + \cfrac{1}{1 + \cfrac{1}{1+\cfrac{1}{1+\ldots}}} = \tau \quad , \tag{1.3}$$

where τ is an irrational number called the 'golden mean'. Therefore we know that in the infinite Fibonacci word the ratio of the overall occurrence of L letters compared to the total number of letters (the 'frequency' of L letters N_L/N_{tot}) is irrational.

Conversely, if the Fibonacci chain was periodic it would contain (at least) one sub-word that is repeated infinitely often. Therefore the frequency of letters in the limit $m \to \infty$, given by the ratio of letters in this sub-word, would be rational. Thus the Fibonacci chain is aperiodic.[10]

At the same time the Fibonacci word is not random, since it was constructed using a deterministic rule (Eq. 1.1). In other words: the Fibonacci chain is long-range ordered.[11]

The corresponding 'Fibonacci lattice' can be constructed from the chain by placing atoms at the vertices in between the line segments. We can write down the position x of the nth atom in a closed form [44]

$$x_n = S\left(n + \frac{1}{\nu}\left\lfloor \frac{n+1}{\nu} \right\rfloor\right) \quad , \tag{1.4}$$

emphasising the presence of long-range order in the system. Here $\lfloor\cdot\rfloor$ denotes the floor function and $\nu \equiv L/S$ the ratio of lengths of the two line segments.

To summarise, the Fibonacci chain is both aperiodic and long-range ordered.

So far, we have considered arbitrary values for L and S, leading to a deterministic and aperiodic arrangement of atoms in the Fibonacci lattice. Next we consider how a particular choice of ν can lead to self-similarity.

Self-similarity

Self-similarity means invariance under length scaling operations. Therefore, in order to construct a self-similar Fibonacci lattice we simply demand that replacing L with LS and S with L (Eq. 1.1) corresponds to the same (relative) increase in length, namely

$$\frac{L+S}{L} \stackrel{!}{=} \frac{L}{S} \equiv \nu \tag{1.5}$$

Table 1.2: Number of letters in the Fibonacci word after m substitution steps. This sequence of numbers has been known for a very long time, at least since the 13th century [42]; nowadays these numbers are known as Fibonacci numbers.

m	1	2	3	4	5	6	7
$N_S(m)$	0	1	1	2	3	5	8
$N_L(m)$	1	1	2	3	5	8	13

[10] This is true independent of the precise value of L/S (the ratio of lengths in the diagrammatic representation), in contrast to ref. [43]. The cases $L/S = 1$ and $L/S \to \infty$ (L being finite) are a trivially periodic inasmuch as they contain just one non-zero spacing.

[11] this will be shown explicitly later by its diffraction pattern

It is intriguing that as early as 1944, Schrödinger [45] introduced the concept of aperiodic order as a possible explanation for life on earth. At the time, the microscopic function of genes and the structure of DNA was unknown, but the question was already recognised on how such a fragile structure (then estimated at around one million atoms) could robustly encode enough information, lasting many generations, to form a living organism and seemingly violate the second law of thermodynamics. Schrödinger proposed an aperiodic crystal as 'code-script' in which all the information was encoded by the exact configuration of atoms. It is now known that DNA does not represent a deterministic recipe as Schrödinger envisaged but it functions as a resource that interacts with its environment, thereby upholding a constant non-equilibrium of the organism in its surroundings ('life') which does not violate the overall rise in entropy. However, the gist of his original idea that information is carried by aperiodic sequences (the order in which the nucleotides A, C, G, and T appear) has indeed proven correct. Ref. [46] offers a very recent introductory review on Schrödinger's book. See also ref. [12].

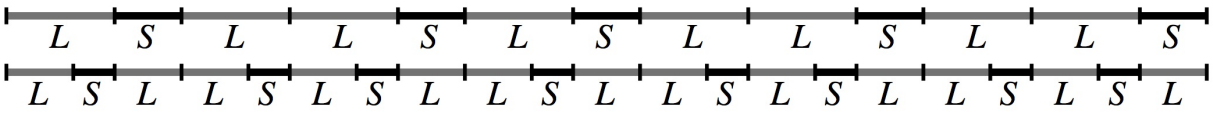

Figure 1.4: Self-similarity of the 'golden' Fibonacci chain ($\nu = \tau$). If the upper Fibonacci chain is scaled down by a factor τ, the resulting structure is again a Fibonacci chain. Figure taken and adapted from [47].

or, equivalently,

$$1 + \frac{1}{\nu} = \nu \tag{1.6}$$

$$\nu^2 - \nu - 1 = 0 \tag{1.7}$$

leading to

$$\nu^{\pm} = \frac{1 \pm \sqrt{5}}{2} \tag{1.8}$$

$$\nu^{+} = \frac{1 + \sqrt{5}}{2} = 2\cos\left(\frac{3\pi}{10}\right) = 1.618033989\cdots \equiv \tau \tag{1.9}$$

The value τ is the aforementioned limit of two adjacant Fibonacci numbers, the golden mean.[12,13] A Fibonacci lattice with the self-similar property $\nu = \tau$ is shown in Fig. 1.4. Here self-similarity manifests itself in the appearance of structures on larger and larger lengthscales.

[12] Another way to get the values $\nu^{\pm}$ is to simply diagonalise the substitution matrix in Eq. 1.2.

[13] It is called an 'algebraic number' because it is the solution to Eq. 1.7 which only has rational (in this case integers) coefficients.

Self-similarity is a characteristic feature of quasicrystals which we are able to directly observe in the experiment (Chapter 6). It constrasts the usual notion of coarse-graining in periodic lattices: In the thermodynamic limit (system size $V \to \infty$ and $N \to \infty$, while $N/V = $ constant) the ratio of lattice spacing a to system size tends to zero. Thermodynamic properties such as entropy or magnetisation therefore do not depend on the value of a. In self-similar systems such as quasicrystals this approach fails since, even for arbitrarily big lengthscales, the system still resembles an inflated version of the microscopic model.

Apart from being conceptually interesting, self-similarity frequently appears in nature and society in the form of fractal structures, for example in network traffic [48], biology and medicine [49], and cosmology [50]. There are also well-known examples in various plants, such as romanesco broccoli, ferns, and sunflowers.

The study of ultracold atoms in quasicrystalline lattices might provide a novel approach to studying fractal structures in a well-controlled environment. The use of massive, quantum degenerate particles – atoms – in this work represents a major advance compared to previous studies of quasicrystals with massless photons [13] and classical particles in optical lattices [14–17].

Having covered the concept of self-similarity we can build some physical intuition on long-range order in quasicrystals by looking at their diffraction pattern, i.e. their structure in reciprocal space. This is particularly relevant for the diffraction experiments that were performed in this work using ultracold atoms. In addition,

diffraction patterns are the only way of fundamentally discriminating between quasicrystals and disordered aperiodic structures.

Diffraction pattern of the Fibonacci lattice

The density distribution of a 1D discrete lattice can be written as

$$\rho(x) = \frac{1}{N}\sum_{n=1}^{N}\delta(x - x_n) \quad , \tag{1.10}$$

where the sum goes over all lattice points, x_n are the positions of the atoms (taken from Eq. 1.4 in the case of a Fibonacci lattice), and $\delta(x)$ represents the Dirac δ-distribution. The diffraction pattern arising from $\rho(x)$ is given by its structure factor which corresponds to the modulus squared of its Fourier transform

$$F(q) \equiv |\mathcal{F}[\rho(x)]|^2 = \left|\frac{1}{\sqrt{2\pi}}\int_{-\infty}^{+\infty}\rho(x)e^{iqx}\,\mathrm{d}x\right|^2 \quad . \tag{1.11}$$

Here q is the change in wave vector due to the diffraction.

Periodic lattices: periodic long-range order

Before we come to the Fibonacci lattice, les us consider the diffraction pattern resulting from a periodic lattice with unity spacing ($S = 1$). It is simply a comb of δ-peaks with regular spacing $q_0 = 2\pi/S = 2\pi$, as shown in Fig. 1.5A. There is a weak modulation of the height of the peaks and on a much smaller scale than $q = 2\pi$ there are ripples in the pattern which are not resolved on the figure. Both of these effects arise from the finite size (21 atoms) of the simulated lattice. This regularly-spaced diffraction pattern is the signature of periodic long-range order.

Next, we consider another periodic lattice of the same size ($N = 21$) but with two incommensurable spacings $S = 1$ and $L = \tau$, i.e. $LSLSLS\ldots$. The diffraction pattern for this configuration is plotted in Fig. 1.5B. Similar to Fig. 1.5A, the spacing between the peaks is perfectly regular; in this case it is given by

$$q_0 \equiv \frac{2\pi}{S+L} = \frac{2\pi}{1+\tau} \quad . \tag{1.12}$$

As before, the regularly-spaced peaks herald periodic long-range order. However, the height of the peaks is strongly modulated which is a consequence of the presence of two incommensurable lengths S and L. The overall structure is perfectly periodic.

Fibonacci lattice: aperiodic long-range order

The diffraction pattern of a 21-atom 'golden' Fibonacci lattice ($\nu = \tau$)[14] is plotted in Fig. 1.5C. At first sight it may look similar to the periodic case but there are two important differences. Firstly, the main peaks are not spaced periodically (in contrast to Fig. 1.5B) but aperiodically. Secondly, there are many more peaks in between the main peaks and there exists no single fundamental distance q_0. By indexing this diffraction pattern we can demonstrate the aperiodic order of the Fibonacci chain.

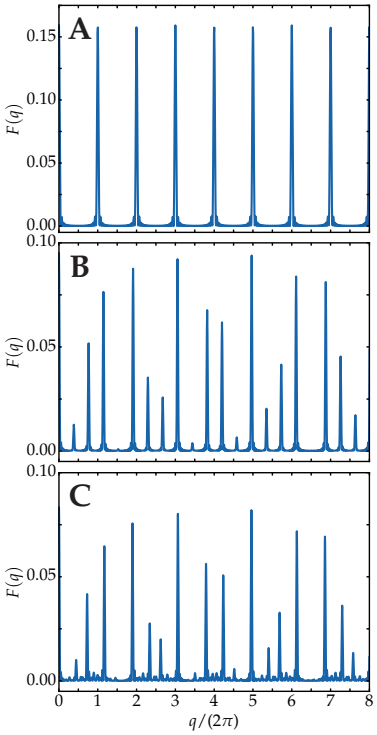

Figure 1.5: Theoretical diffraction patterns (Eq. 1.11) for three different lattices. (**A**) Periodic lattice with spacing $S = 1$. (**B**) Periodic lattice of the type $LSLSLS\ldots$ with spacing $1 + \tau$ (two atoms per unit cell). (**C**) Fibonacci lattice with $\nu = L/S = \tau$. The diffraction peaks in (**A**) and (**B**) are perfectly regularly spaced (see text), indicating the presence of periodic long-range order. In contrast, (**C**) consists of a dense set of peaks, highlighting the aperiodic long-range order of the Fibonacci lattice. Although the envelope in (**C**) looks very similar to that of (**B**), the main peaks are not spaced regularly as can be seen upon close inspection (see also Fig. 1.7). All simulated lattices in this figure consist of 21 atoms; the value of τ (golden mean) is given by Eq. 1.9.

[14] Note that any irrational value of ν leads to a quasicrystal, not just $\nu = \tau$. But we have chosen the special value $\nu = \tau$ because it nicely illustrates the self-similarity of the 'golden' Fibonacci chain in reciprocal space. This is already hinted at in Fig. 1.5B which – although it is entirely periodic in real space – shows signatures of self-similarity.

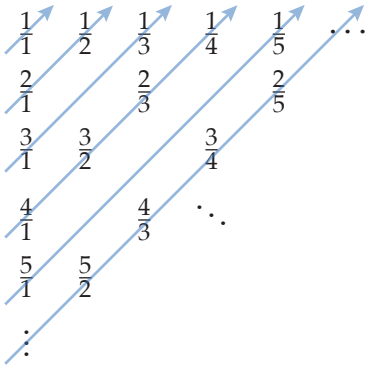

Figure 1.6: Cantor's proof of $\mathbb{Q}^+$ being a countable set. The sketch shows the existence of a bijection from $\mathbb{N}$ to $\mathbb{Q}^+$ by counting the rational numbers diagonally [51].

[15] e.g. $2/4 = 1/2$, $2/2 = 1$

Indexing quasiperiodic diffraction patterns: aperiodic order

First, let us take a closer look at the diffraction pattern of the Fibonacci lattice (Fig. 1.5C). A single reciprocal lattice vector, i.e. a single index (h) where $h \in \mathbb{Z}$, is not sufficient to uniquely identify all the peaks since they are not spaced by equal distances. Similarly, in the in-plane diffraction image of a physical quasicrystal (Fig. 1.3C) two indices (h,k) are not sufficient to account for all the peak positions since the distances in reciprocal space become smaller and smaller. In fact, the peaks are densely spaced in these cases due to the incommensurability of two (or more) lengths in the quasicrystal. For example, in the 'golden' Fibonacci lattice $L = \tau$ is incommensurable with $S = 1$. Consequently, there are as many peaks as there are rational numbers: infinitely many. Does this mean indexing the golden diffraction pattern (Fig. 1.5C) is a lost cause?

Luckily it does not. An intuitive way of counting all positive rational numbers, introduced by Cantor in the 19$^{\text{th}}$ century, comes to the rescue. We simply have to write the rational numbers down in a two-dimensional array (Fig. 1.6), ordered by numerators (rows) and denominators (columns). Subsequently we remove all duplicates[15] and then each rational number along the diagonal can be identified with one non-negative integer, as shown in Fig. 1.6.

Inspired by the method of counting $\mathbb{Q}^+$ we can index all the diffraction peaks of the 1D quasicrystal by using two integers instead of one, namely

$$q_{l,m} = \frac{2\pi l}{a} + \frac{2\pi m}{b} \quad \text{, where} \quad l,m \in \mathbb{Z} \quad \text{and} \quad a,b \in \mathbb{R} \quad . \tag{1.13}$$

At least one of the values a, b has to be irrational. In the case of the golden Fibonacci lattice ($\nu = \tau$) the values for a and b can be derived analytically [44] using Eq. 1.4. The result is

$$q_{l,m} = \frac{2\pi}{1+\frac{1}{\tau^2}} \left(\frac{l}{\tau} + m \right) \quad . \tag{1.14}$$

The positive indices for $l, m \leq 8$ are shown in Fig. 1.7, together with the simulated diffraction for the 21-atom golden Fibonacci lattice (Fig. 1.5C).

How to tell the Fibonacci lattice apart from a random lattice?

The dense set of diffraction peaks resulting from the Fibonacci lattice poses an interesting question: How can we be sure that the Fibonacci chain is ordered and not random? On the one hand, the deterministic construction rule should ensure perfect long-range order. On the other hand, long-range order is really defined by the existence of sharp diffraction peaks. Therefore it must be possible to distinguish a random lattice from a Fibonacci lattice just by observing their respective diffraction patterns.[16]

For a random lattice, let us consider a non-deterministic construction rule in which the length of each bond is randomly chosen to be either $S = 1$ or $L = \tau$. The probability for each line

[16] In other words: The diffraction process does not know about the rule by which the lattice was created. It only knows about the resulting pattern of lattice sites.

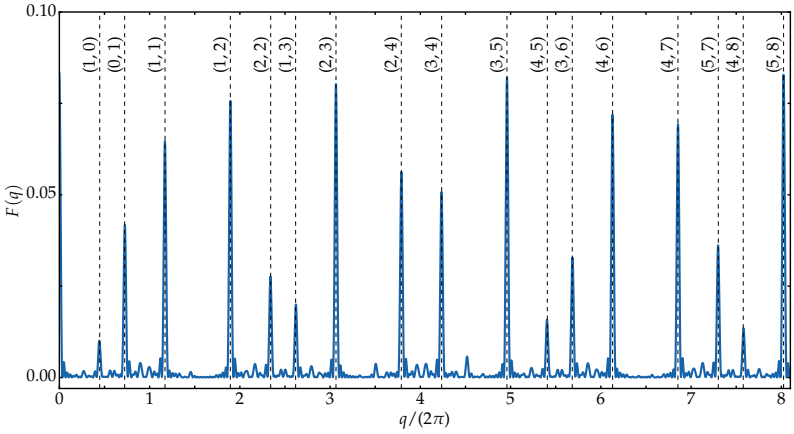

Figure 1.7: Two-dimensional indexing for the 1D golden Fibonacci lattice. The dashed lines are labelled according to Eq. 1.14. The diffraction pattern was obtained from a 21-atom Fibonacci lattice with $\nu = \tau$.

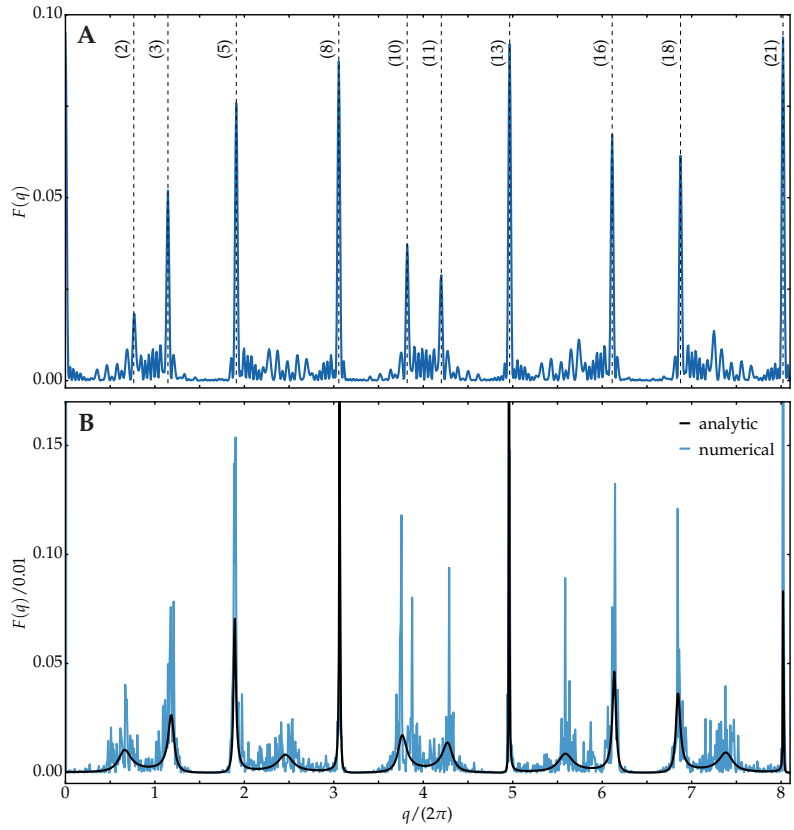

Figure 1.8: Diffraction patterns of 1D random lattices with $\nu = L/S = \tau$ (see text). (**A**) Lattice length $N = 21$. The most pronounced diffraction peaks are spaced periodically in distances of $q_0 = 2\pi/(S + L)$ (c.f. Fig. 1.5B) which are labelled according to their position. These peaks arise from the frequently occurring pattern LS. In between the pronounced peaks there are many more sharp peaks which are not spaced periodically. These could be (wrongly) interpreted as the signature of aperiodic order. (**B**) $N = 1000$ (light blue). For a larger system size the disorder becomes apparent: the diffraction pattern becomes continuous and smeared out. The numerical curve is overlaid with the analytic results from ref. [9] (black line) which corresponds to an infinite random chain. For even larger system sizes the diffraction pattern would more closely resemble that of the analytic calculation. Some peaks remain sharp due to a frequent occurrence of certain patterns, the same as (**A**).

segment being L shall be $1/\tau$ such that the overall occurrence of L is roughly equal to that in the aperiodic ordered Fibonacci chain.[17] The diffraction pattern of such a random lattice ($N = 21$) is shown in Fig. 1.8A. At first sight it does not differ greatly from the diffraction pattern of the perfectly ordered Fibonacci lattice (Fig. 1.7); the most pronounced peaks are spaced similarly but not identically to the periodic case. For this random lattice a single index is sufficient to label them, as demonstrated in Fig. 1.8A. The background in the random case shows some noise which could be interpreted as a dense set of peaks. In this system size (21 atoms) there is no qualitative difference between a random lattice and an

[17] this random chain is discussed in more detail in ref. [9]

aperiodic ordered lattice. However, the randomness does show up in a sufficiently large system (Fig. 1.8B). For $N = 1000$ the diffraction pattern becomes smooth[18] and tends towards the analytic solution for an infinite random chain [9]. From this we draw the conclusion that system size is crucial for determining true long-range order.[19]

[18] although it retains some sharp peaks which arise from the frequent occurrence of certain combinations such as *LS* and *LLS*

[19] As usual with quasicrystals, it is not always as simple as that. A class of pathological 1D quasicrystals was constructed by Baake and Grimm [52] whose diffraction patterns cannot be distinguished from completely disordered structures. Nevertheless, for all practical purposes the sharp peaks in the diffraction pattern are a clear signature of order.

Projection from higher dimensions

The indexing method described above uses two indices to describe the diffraction pattern of a 1D quasicrystal. On the one hand, the requirement of two indices can simply be understood as the consequence of the presence of two incommensurable lengths in the system. On the other hand, the double-indexing naturally leads to the notion that dimensions higher than the physical ones are at play in quasicrystals. Therefore one can re-interpret the diffraction pattern in Fig. 1.7 as the diffraction off a (fictitious) two-dimensional periodic lattice, projected down to one dimension. This concept has proven extraordinarily powerful in the determination of quasicrystalline structure and it is nowadays routinely used to describe and classify quasicrystals [11, 53, 54]. It extends naturally to physical dimensions higher than one. In general, the number of extra dimensions needed to describe a given quasicrystal is equal to the number of its linearly independent lattice vectors over $\mathbb{Q}$ [55]. For example, the icosahedral symmetry of the Zn-Mg-Dy quasicrystal (Fig. 1.1) requires six independent lattice vectors to describe its diffraction pattern (Fig. 1.3) and consequently the periodic 'image' lattice is six-dimensional. Our experimental setting involves a planar, eightfold symmetric optical lattice which can be uniquely described by four independent lattice vectors. Consequently, the experiment is connected to four-dimensional space; Chapter 6 shows the direct simulation of a continuous-time quantum walk on a homogeneous 4D tight-binding lattice using this notion.

The projection method is not only useful for crystallography and indexing but it is also used to construct models of quasicrystals in real space via the so-called 'cut-and-project' scheme.[20]

[20] also called 'projection method' or 'strip-projection'

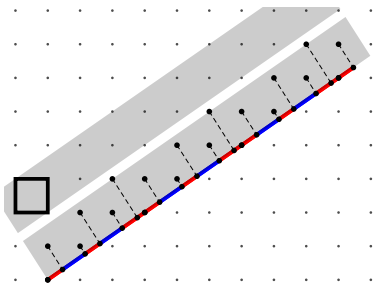

Figure 1.9: Schematic of the cut-and-project scheme for a rational slope ($m = 2/3$) leading to a periodic 1D crystal. The width of the acceptance window is given by the projection of the 2D unit cell (black square) to perpendicular space.

Cut-and-project

The cut-and-project scheme is widely used to contruct models of quasicrystals, as well as study their physical properties. It is illustrated in Figs. 1.9 and 1.10 for one-dimensional structures. The construction involves defining a periodic lattice, for example a simple cubic lattice ($\cong \mathbb{Z}^2$) in two dimensions (x, y). Rotation by an angle α defines a new coordinate system (x', y') which can be interpreted as parallel space (x') and perpendicular space (y'). Parallel space corresponds to the new, physical 1D lattice. In perpendicular space a certain 'acceptance window' (or 'slice') is chosen and points within this window are then projected to parallel space to form the new one-dimensional structure. In one dimension the

description can be written in terms of a slope $m = \tan\alpha$. The width Δ of the slice is given by the projection of the diagonal of the 2D unit cell (black square in Fig. 1.9) to perpendicular space, namely

$$\Delta = \frac{1+m}{\sqrt{1+m^2}} \quad . \tag{1.15}$$

The crucial parameter in this construction is the value of the slope m. If it is chosen to be rational, the constructed lattice will be periodic (Fig. 1.9). If it is chosen to be irrational, the constructed lattice is aperiodic (Fig. 1.10). In particular, if we choose $m = 1/\tau$ the resulting lattice is the golden Fibonacci chain.

Note that although the 'window' itself looks two-dimensional it is actually just a 1D width in perpendicular space. All points that fall into the width under perpendicular projection are 'accepted' and then projected to parallel (physical) space.

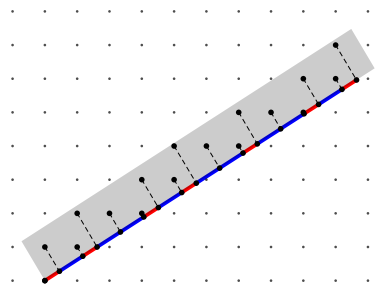

Figure 1.10: Schematic of the cut-and-project scheme for an irrational slope ($m = 1/\tau$) leading to an aperiodic 1D crystals, namely the Fibonacci lattice.

Phasons

In periodic lattices there are two types of low-energy excitations, namely electronic excitations and phonons (lattice vibrations). Without going into too much detail, the cut-and-project scheme can help us gain some intuition on additional excitations that are unique to quasicrystals, called phasons [56]. Phasons are markedly different from phonons which are characterised by wave packets, propagating through the crystal.

In quasicrystals it can be energetically favourable for an atom to perform a sudden 'phason jump' to a new equilibrium position, rather than being excited around its original equilibrium position. This process can be illustrated by phonons in perpendicular space. In Fig. 1.11 the acceptance window in the cut-and-project scheme has been displaced by a small amount (0.3 lattice spacings). The resulting lattice is another golden Fibonacci lattice but compared to Fig. 1.10 some atoms have jumped to a new position by a distance $1 - \tau$. These are just the simplest cases of phasonic excitations, corresponding to a centre-of-mass movement of the acceptance window ($q = 0$ phonon modes). Non-zero q phonon modes, i.e. phonons with finite wavelength, introduce displacements that can lead to the appearance of subsequences, such as $LSLSL$ or $SLLLS$, that do not appear in the Fibonacci lattice (see Fig. 1.12). Moreover, a change in phase of the finite-wavelength acceptance window can lead to the appearance of new spacings, namely $L - S$ and $L + S$ in the resulting 1D lattice, as shown in Fig. 1.13.

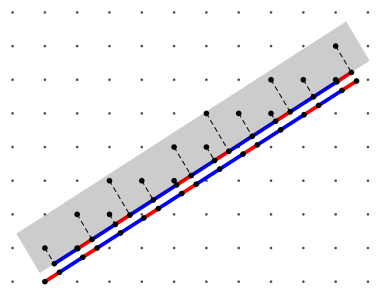

Figure 1.11: Phasonic excitation of the Fibonacci lattice. The acceptance window has been displaced by 0.3 lattice spacings compared to Fig. 1.10 (the original Fibonacci lattice is also shown). Small displacements of the acceptance window in the perpendicular direction can lead to sudden displacement of some atomic positions. Sequences of LS turn into SL, a process called 'phason flip'.

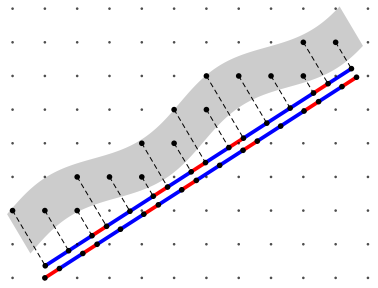

Figure 1.12: Phasonic excitation with non-zero wavelength (see text).

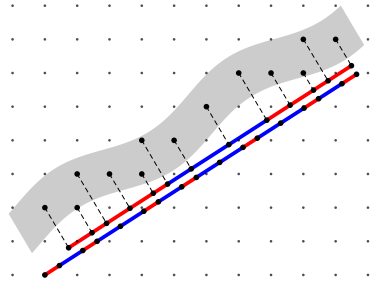

Figure 1.13: Phasonic excitation with non-zero wavelength and different phase compared to Fig. 1.12 above. New spacings are introduced in this case.

These phasonic excitations, in contrast to phonons, are not propagative but diffusive, meaning that their 'dispersion relation' is purely imaginary [56]. Phasonic excitations can lead to broadening of diffraction peaks and diffuse background scattering. It is expected that phasons contribute considerable entropy to quasicrystals, even at low temperatures. Phasons could potentially stabilise them against energetically competing *periodic* configura-

tions [53], i.e. minimise the free energy $F = E - TS$ by increasing the TS contribution (T being temperature, S being entropy, and E being the internal energy).

Up to this point quasicrystals have been discussed in one dimension, thereby reviewing their most important characteristics, namly quasiperiodicity, self-similarity, and the projection from higher dimensions. However, one-dimensional space does not support rotations. Therefore, 2D quasicrystals will be covered in the following, beginning with the notion of 'forbidden' rotational symmetries. After all, an unexpected tenfold symmetry in the diffraction pattern of $Al_{86}Mn_{14}$ lead to the discovery of quasicrystals [1] in the first place.

1.3 *Quasicrystals in two dimensions, the octagonal tiling*

Before we come to two-dimensional quasicrystals we need to take a step back and consider two-dimensional periodic crystals.

A periodic lattice can be uniquely defined by its unit cell and a set of lattice vectors. Translation of a given lattice point by any of the lattice vectors results in an equivalent lattice point. The unit cell describes the arrangement of atoms relative to a lattice point. Note that in any physical system the lattice will be discrete, i.e. the distance between any two lattice points is larger than zero. In the following it will be shown that periodic lattices are incompatible with rotational symmetries higher than sixfold rotational symmetry and also incompatible with fivefold rotational symmetry, following an original proof of ref. [57].

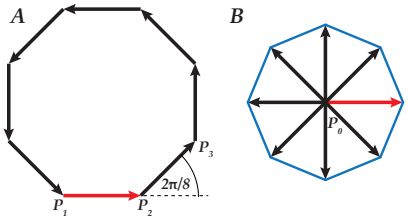

Figure 1.14: Sketch of crystallographic restriction for the case $n = 8$. (**A**) and (**B**) represent the two contructions of an eightfold symmetric polygon that are used in the proof. An infinite series of polygons can be constructed by using the edges of (**B**) to construct yet another polygon, and so on. The fact that the perimeter of (**B**) is smaller than that of (**A**) ensures that in the limit of this series the value of the perimeter vanishes, thus contradicting the discreteness of the lattice.

Crystallographic restriction

Theorem. *Periodic lattices are not compatible with any n-fold rotational symmetry for $n > 6$ and $n = 5$.*

Proof. Consider an n-fold rotational symmetry for $n > 6$ on a discrete lattice (the case $n = 5$ will considered separately). We start constructing a regular polygon 'A' from one lattice point P_1 by adding a lattice vector to reach another lattice point P_2. Subsequently we add a second lattice vector, rotated by $2\pi/n$, to the point P_2 to reach a third lattice point P_3. We keep doing this until we reach again P_1, having constructed A in its entirety; an example of this construction is shown in Fig. 1.14 for the case $n = 8$. Let the perimeter of A be called s_A.

Now, if we protract all the above vectors $\overrightarrow{P_1P_2}, \overrightarrow{P_2P_3}, \ldots$ from one single lattice point P_0 we have constructed another regular polygon 'B' with smaller perimeter s_B, shown in Fig. 1.14 (blue line). The ratio between the two perimeters of A and B is only dependent on n, namely

$$\frac{s_B}{s_A} = 2\sin\left(\frac{\pi}{n}\right) < 1 \quad . \tag{1.16}$$

Taking the edges of the smaller polygon (B) as the new vectors to construct yet another polygon C, and so on, will lead to an infinite series of polygons. Since the ratio of perimeters of two subsequent polygons in this series is strictly smaller than one (Eq. 1.16) the edges of the polygons in the series converge to zero. This contradicts the physical assumption of a discrete lattice.

The special case of $n = 5$ entails the identical construction of the pentagon A but it necessitates a slightly more complicated construction of the pentagon B (and the successive elements of the series). In this case, the smaller pentagon (B) is constructed by successively protracting the vectors $\overrightarrow{P_5P_4}, \overrightarrow{P_1P_5}, \ldots$ from the lattice points $P_1, P_2, \ldots$, rather than to one central point. The ratio of perimeters is then

$$\frac{s_B}{s_A} = \left|1 - \sin^2\left(\frac{\pi}{n}\right)\right| < 1 \quad .$$

This construction can be used analogously to prove the theorem for all cases including $n = 5$ and $n > 6$. □

The proof of crystallographic restriction completes the discussion of periodic lattices.

Since sharp diffraction patterns with tenfold rotational symmetry have been observed [1] (see also Fig. 1.3) it is immediately clear that in an aperiodic lattice higher rotational symmetries must be somehow possible. Furthermore, crystallographic restriction implies that experimental evidence of sharp diffraction peaks with, say, eightfold symmetry is a sufficient criterion to identify a quasicrystal.[21] In order to get a more microscopic picture of two-dimensional quasicrystal it is instructive to consider aperiodic tilings, a subject within the mathematical field of geometry.[22]

[21] However, one must avoid various crystallographic pitfalls that can lead to apparent rotational symmetries in the diffraction pattern. For example, a particular arrangement of four atoms in a 2D simple cubic lattice produces an approximately eightfold symmetric diffraction pattern (see ref. [58], section 3, or ref. [9], Chapter 9). This effect is very similar to the diffraction pattern obtained from a 1D simple cubic lattice with two atoms per site which are arranged in a particular way (Fig. 1.5B). This shows signatures of self-similarity although the underlying lattice is entirely periodic.

[22] Refs. [3] and [9] give an accessible introduction to the topic. An exhaustive treatment can be found in ref. [10].

Aperiodic ordered tilings

A tiling, or tessellation, represents a way to cover a plane using a set of geometric shapes ('tiles'), without any gaps or overlaps [10]. Until the early 60s it was assumed by Hao Wang [59, 60] and others that all coverings of the plane using square tiles with decorated edges would repeat themselves after a long distance, i.e. be periodic. However, it was later shown that aperiodic coverings of the plane do indeed exist [61]. Moreover, it was shown that, given a certain set of tiles, it is generally impossible to decide whether or not these tiles support an infinite covering of the plane; this is known as the 'undecidability of the domino problem'. This proof is another representation of the undecidability of the Turing machine halting problem [62]. It has even been shown that these 'Wang tiles' can perform computations in the same way a Turing machine does [63].

Very recently, the undecidability of the domino problem has been mapped to a very general class of many-body hamiltonians, namely two-dimensional spin systems, with the result that is impossible to predict whether these hamiltonians support

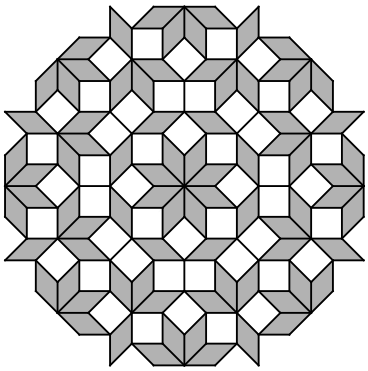

Figure 1.15: A patch of the octagonal tiling.

gapless or gapped excitations [31]. It is therefore to be expected that constructing physical systems of quantum particles in aperiodic potentials such as our quasicrystalline lattice will result in many-body systems of unprecedented complexity. Maybe self-assembly methods could be exploited similar to those that allow DNA-strands to be used as Wang tiles in the construction of crystals [64]. It is not unthinkable that one day atoms in quasicrystalline lattice might act as 'quantum Turing machine'.

The aperiodic tilings considered so far consist of square 'Wang tiles' and hence they do not explain the existence of non-crystallographic rotational symmetries. The first pentagonal tiling was found in 1974 by Penrose [8]:

> I had often doodled by fitting together limited configurations of pentagons and similar shapes but I had never found a good rule for continuing such patterns indefinitely. However, recently I wanted to design something interesting for someone who was in hostipal to look at and I realised that there was a certain definite rule whereby one could continue such a pattern to arbitrary size.

This pattern is nowadays widely known as the Penrose tiling. Later, an eightfold analogue to the Penrose tiling was found, the so-called Ammann-Beenker tiling [10] or 'octagonal tiling'. A patch of the octagonal tiling is shown in Fig. 1.15, consisting of two types of tiles (a square and a rhombus) from which the entire pattern can be pieced together indefinitely.

Construction rules

How is it possible to construct an aperiodic tiling, such as the octagonal tiling? Similar to the Fibonacci chain there are construction rules that allow deterministic tiling of the plane using two different shapes (in this case a square and a rhombus). In brief, the construction relies on matching rules for adjacent tiles, similar to a puzzle game. This process is illustrated in Fig. 1.16A by 'decorating' the vertices and the edges of the tiles with arrows. The arrows on the vertices add local information to the tiles, thereby ensuring 'validity' of the infinite tiling, i.e. that there are no gaps. Non-deterministic construction rules can be used to generate random octagonal-like tilings with approximate eightfold symmetry [9].

Another way of constructing the octagonal tiling makes use of its self-similarity.

Self-similarity

The octagonal tiling is self-similar under scaling the edges of the tiles by the so-called silver mean,

$$\lambda = 1 + \sqrt{2} \quad . \tag{1.17}$$

Similar to the golden mean (Eq. 1.9) λ is an algebraic number, obeying the equation

$$x^2 - 2x - 1 = 0 \quad , \tag{1.18}$$

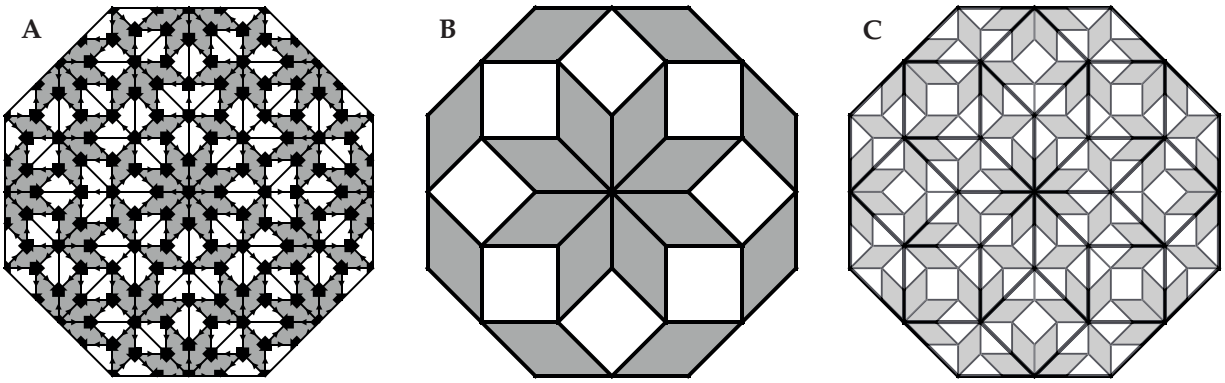

Figure 1.16: Octagonal tiling. (**A**) 'Decorated' octagonal tiling, illustrating the construction rules. (**B**) - (**C**) Self-similarity of the octagonal tiling under 'silver mean' scaling. These images were generated using the *Mathematica* package 'Aperiodic tilings' [65], see also ref. [47].

and it can be represented by a continued fraction analogous to that in Eq. 1.3

$$\lambda = 2 + \frac{1}{2 + \frac{1}{2 + \frac{1}{2+\ldots}}} \quad . \tag{1.19}$$

However, the self-similar scaling operation of the octagonal tiling is less trivial than its 1D counterpart, in which applying the scaling operation to any patch of the Fibonacci chain results in another valid Fibonacci chain (Fig. 1.4). In the two-dimensional case of the octagonal tiling the scaling operation by a factor λ can nevertheless be used if certain rules are obeyed which are shown in Fig. 1.17. These allow self-similar scaling even if the position of the origin is unknown. One step of self-similar scaling of the octagonal tiling – also called 'inflation' – is shown in Fig. 1.16B-C.

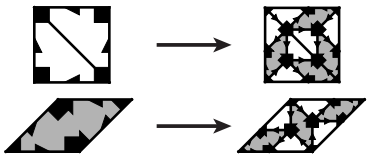

Figure 1.17: Scaling by a factor λ (Eq. 1.17) generates a self-similar copy of the octagonal tiling (Fig. 1.16 B and C).

The construction of the octagonal tiling based on local rules (even in the case of self-similar inflation) is cumbersome because it is an iterative process. Similar to the Fibonacci chain, the construction via cut-and-project is far easier and much more efficient. In addition, it can provide intuition about phasonic excitations in this lattice.

Cut-and-project

In the case of the octagonal tiling the cut-and-project scheme starts with constructing a four-dimensional (4D) simple-cubic lattice $L \cong \mathbb{Z}^4$. The basis of L can be written as

$$\left\{ \begin{pmatrix} 1 \\ 0 \\ 0 \\ 0 \end{pmatrix}, \begin{pmatrix} 0 \\ 1 \\ 0 \\ 0 \end{pmatrix}, \begin{pmatrix} 0 \\ 0 \\ 1 \\ 0 \end{pmatrix}, \begin{pmatrix} 0 \\ 0 \\ 0 \\ 1 \end{pmatrix} \right\} \tag{1.20}$$

in canonical coordinates (x_1, x_2, x_3, x_4), $x_i \in \mathbb{Z}$. Similar to the Fibonacci case we define a rotation [9]

$$\mathcal{R} = \frac{1}{2} \begin{pmatrix} \sqrt{2} & 1 & 0 & -1 \\ 0 & 1 & \sqrt{2} & 1 \\ \sqrt{2} & -1 & 0 & 1 \\ 0 & 1 & -\sqrt{2} & 1 \end{pmatrix} \tag{1.21}$$

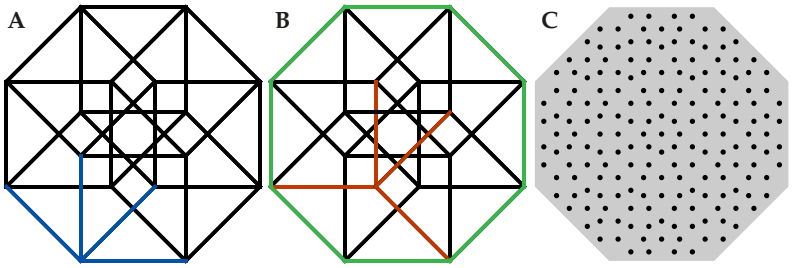

Figure 1.18: Parallel (**A**) and perpendicular (**B**) projection ('shadow') of a hypercube (unit cell of 4D simple-cubic lattice) using Eq. 1.22. The four basis vectors (Eq. 1.20), i.e. edges of the unit hypercube, are shown in blue (**A**) and in red (**B**), respectively. The shadows in both parallel and perpendicular projection are identical. The hypercube has an edge length of unity whereas the shadows have edge lengths $1/\sqrt{2}$. (**C**) The acceptance window in perpendicular space (grey) for the 4D cut-and-project scheme is the 2D perimeter of the shadow in perpendicular projection, i.e. outer green line in (**B**). The points in (**C**) are the same elements of $\mathbb{Z}^4$ (or, equivalently, the 4D simple-cubic lattice) that are also shown in Fig. 1.19 in physical/parallel space. (**A-C**) are drawn to the same scale.

such that the new coordinates are

$$\begin{pmatrix} x \\ y \\ x' \\ y' \end{pmatrix} = \mathcal{R} \begin{pmatrix} x_1 \\ x_2 \\ x_3 \\ x_4 \end{pmatrix} \quad . \tag{1.22}$$

The first two coordinates (x, y) are parallel (physical) space and the last two (x', y') are perpendicular space; a projection of (x_1, x_2, x_3, x_4) to perpendicular space corresponds to multiplication by the first two rows of $\mathcal{R}$. The projection to parallel space, correspondingly, is given by the multiplication by the last two rows of $\mathcal{R}$.

As before, the width of the acceptance window is given by the projection of the 4D unit cell to perpendicular space, which means that the acceptance window in this case is two-dimensional. The projections of the 4D unit cell are shown in Fig. 1.18A-B; both perpendicular and parallel projections ('shadows') have a 2D octagonal perimeter of the same size. The acceptance window is then chosen to be the perimeter of this octagon (green line in Fig. 1.18B). The points that fall into this window under perpendicular projection (Fig. 1.18C) form the octagonal tiling in physical space, simply by performing a parallel projection (Fig. 1.19).

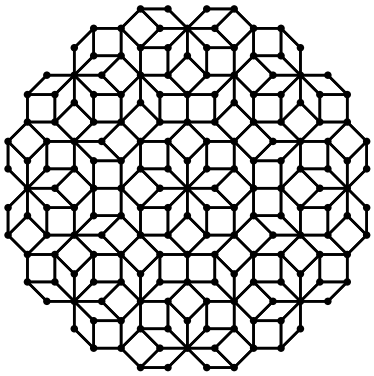

Figure 1.19: Octagonal tiling generated by projection from a $\mathbb{Z}^4$ using a 4D hypercube with seven lattice sites per edge and unity lattice spacing. The bond lengths (black lines) resulting from this projection have length $1/\sqrt{2}$.

Phasons

Analogous to the Fibonacci case, phasonic excitations can be introduced by shifting the acceptance window by a certain amount. Figure 1.20 shows an example of a phasonic excitation by shifting the acceptance window upwards by 0.2 lattice spacings.

Phasonic excitations of the octagonal tiling will play an important role in the description of 'lattice sites' in the eightfold rotational optical potential (section 5.3).

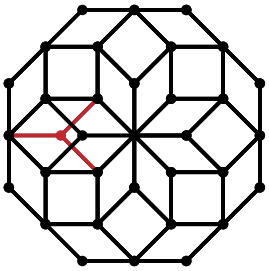

Figure 1.20: One phasonic excitation (red) introduced to the perfect octagonal tiling by shifting the acceptance window (Fig. 1.18C) by 0.2 lattice spacings in the vertical direction. The original octagonal tiling (black) was constructed by projection from $\mathbb{Z}^4$ using a hypercube of size 2^4 (three lattice sites per edge, unit lattice spacing).

Physical diffraction of aperiodic models

The physical significance of aperiodic tilings was realised immediately after the discovery of quasicrystals since the calculated diffraction pattern of a Penrose tiling [66] closely resembled the experimental images obtained by Shechtman et al. [1]. Nowadays aperiodic models such as the Penrose tiling and its three-dimensional icosahedral counterparts [9, 11] are widely accepted

microscopic models for physical icosahedral and decagonal quasicrystals whose crystallographic description is essentially complete [11]. Although physical quasicrystals with eightfold symmetry are comparatively less common [54] the octagonal tiling plays a central role in the modern understanding of quasicrystals, particularly (but not only) from a geometric point of view [9, 67].

The diffraction pattern of the octagonal lattice can be calculated analytically [9] and is shown in Fig. 1.21. It can be described by four reciprocal lattice vectors[23] $\{\mathbf{G}_1, \mathbf{G}_2, \mathbf{G}_3, \mathbf{G}_4\}$ which point in the same respective directions as the parallel projection of the 4D basis vectors (red lines in Fig. 1.18). These lattice vectors are also going to be used to describe the experimental diffraction patterns in Chapter 6.

[23] thus, a four-dimensional image lattice is required to generate the octagonal tiling via the cut-and-project scheme

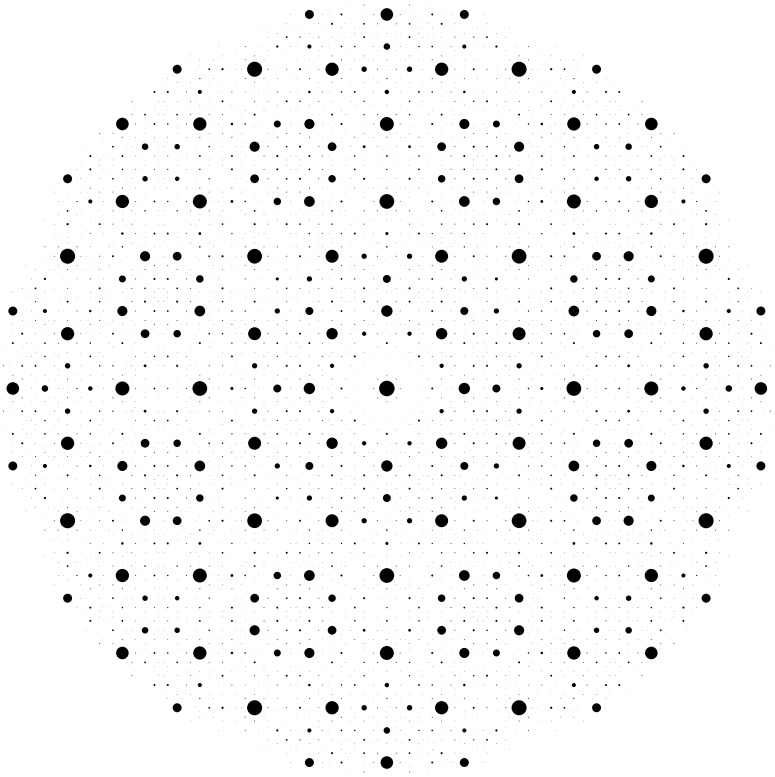

Figure 1.21: Theoretical diffraction pattern of the octagonal tiling. The image shows all peaks with at least 10^{-4} relative intensity (compared to the $q = (0,0)$ peak), which leads to the discrete appearance (the whole diffraction pattern consists of a dense set of peaks). The pattern is perfectly eightfold symmetric and it shows signatures of self-similarity, i.e. the appearance of diffraction peaks at powers of λ. Image taken from [9] with kind permission of the authors.

The main concepts of quasicrystals, namely quasiperiodicity, self-similarity and rotational symmetries have now been discussed in one and two dimensions. In the final section of this chapter the progress that has been made in research on quasicrystals in the past 35 years will be reviewed.

1.4 *Physical quasicrystals and current state of the art*

To date, a huge variety of quasicrystals has been discovered [11, 54]. It is instructive to sort them according to their symmetry and their chemical composition.

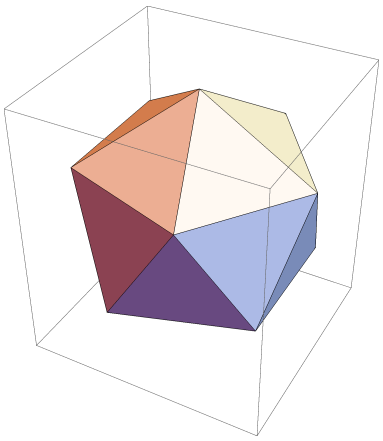

Figure 1.22: A regular convex icosahedron. Each of the twenty faces is an equilateral triangle. Around each vertex there are five faces which form a kind of pentagonal pyramid.

Symmetry

The only thermodynamically stable quasicrystals which have been found up to now exhibit either pentagonal (fivefold) or decagonal (tenfold) or icosahedral (Fig. 1.22) symmetry [11]. Icosahedral quasicrystals are quasiperiodic along all three spacial directions. Conversely, pentagonal and decagonal quasicrystals are quasiperiodic in the plane of the rotational symmetry but periodic along the orthogonal direction. Therefore these quasicrystals are also sometimes called 'axial quasicrystals' [54]. A large variety of axial quasicrystals with varying degrees of structural integrity have been found so far, including pentagonal, octagonal [54, 68], decagonal, and dodecagonal (twelvefold) quasicrystals. However, sevenfold symmetry or any other rotational symmetries not mentioned above have never been observed [11].

Chemical composition

All physical quasicrystals observed so far are binary or tertiary compounds, the vast majority of them being intermetallic compounds. For certain intermetallic materials the relative concentrations of the constituents for which stable quasicrystals exist have been mapped out [11]. However, it is currently an open question whether quasicrystals made of a single chemical element can exist. The stability of many quasicrystals seems to depend very strongly on one chemical property, namely the valence electron concentration [69]. This suggests that electronic mechanisms may play an role in stabilising the high rotational symmetries and aperiodic order in general.

Transport

Electric and thermal transport properties of quasicrystals are generally anisotropic [70]. For example, a high-quality sample of quasicrystalline material can exhibit metallic behaviour along one direction and insulating behaviour along another, despite being an intermetallic compound of aluminium and two other metals (commonly). Similarly, the thermopower or the Hall coefficient can change sign depending on the respective lattice axis it is measured on. These intriguing properties probably can be explained by structural arguments, though it is currently unclear whether local atomic order or long-range aperiodic order is responsible for these unique features [70].

Open questions

Despite much effort to understand quasicrystals better there are still many open questions, even on a fundamental level.

- Are physical quasicrystals energy- or entropy-stabilised? I.e. is the Helmholtz free energy $F = E - TS$ minimal for S be-

ing maximal, or for E being minimal? Is structural disorder inherent in quasicrystals, or can an 'ideal' quasicrystal exist?

- How do quasicrystals form? In other words, quoting ref. [11],

  > How does the 1000th atom find its site in a giant unit cell with thousands of atoms?

- Finally, why are certain rotational symmetries (fivefold, eightfold, tenfold) prevalent in quasicrystals, and why have others (sevenfold, elevenfold, thirteenfold) never been observed?

Apart from the questions listed above which are primarily condensed-matter- and crystallography-driven, research on quasicrystals also touches on the topics of complexity, information science and biology [71, 72].

Physical model systems

Curiously, the only evidence of naturally occurring quasicrystals has been obtained from samples of meteorite material [73, 74]. All other known quasicrystalline materials have been synthesised in the laboratory, some of them (Fig. 1.1) with similar structural quality as best periodic crystals [11].

In order to tackle the questions mentioned above, a variety of physical 'model systems' have been synthesised which aim to emulate quasicrystals with a larger degree of experimental control. Here is a list of physical settings in which quasicrystalline systems have been studied experimentally

- aperiodically layered materials [12], e.g. semiconductors [75]
- liquid crystals [76] and polymers [77]
- self-assembled nanoparticles [78] and colloids [79]
- photonic waveguides [5, 13]. In these systems quasiperiodic patterns can be imprinted by utilising a projected optical lattice [80–82].
- laser-cooled atoms in dissipative optical lattices [14, 15]
- polystyrene spheres in optical lattices [16, 17]
- optical diffraction [66, 83]
- bilayered graphene [84]

Perspectives of ultracold gases in aperiodic lattices

This work establishes quasicrystalline optical lattices as a novel platform for ultracold atoms. Several research avenues can be imagined from here.

On the one hand, there are many open questions regarding the physics of quasicrystals. It has been proposed by Macé et al. [85] that ultracold atoms in a system very similar to ours (see section 5.3) could help solve some of these long-standing mysteries.

This would be particularly interesting from a chemical point of view since up to now only binary and tertiary quasicrystalline compounds have been discovered [11]. Using a single-component quantum gas of potassium, for instance, would resemble this elusive 'unary' quasicrystal.

On the other hand, ultracold atoms in quasicrystalline lattices are interesting and rich systems in their own right. For example, a topological charge pump has been demonstrated experimentally using a 1D photonic quasicrystal [5]. Similary, ultracold atoms in tilted superlattices have recently been shown to represent a 2D topological charge pump, realising in effect a 4D quantum Hall response [86]. These methods may in future be applied also to our quasicrystalline potential thereby realising novel 4D model systems with artificial gauge fields [87].

Another application of aperiodic lattices for ultracold atoms has been the observation of many-body localisation [88]. In particular the role of interactions in quasiperiodic media is poses fundamental questions in physics [89], and experimental results have only recently become available [24, 88, 90, 91]. So far, all experiments employed either 1D [88, 90, 91] or 2D separable [24] potentials. However, more experimental evidence is needed, for instance, to differentiate between two universality classes of localisation phenomena, namely in random disorder and in aperiodic order [92]. For the latter class, our experiment is an ideal starting point since the lattice potential closely resembles the octagonal tiling (see section 5.3), a paradigmatic 2D quasicrystal. The eightfold lattice described in this work is a highly flexible system, not only allowing 1D quasiperiodic and 2D separable quasiperiodic potentials, but also, for the first time, a 2D non-separable aperiodic lattice, i.e. a 2D quasicrystal.

2
Design of the apparatus

This chapter offers a brief overview of the experimental apparatus that is used to create quasicrystalline optical potentials for ultracold atoms, before the apparatus is described in detail in Chapters 3-5. First, the choice of atom (rubidium and potassium) is motivated with a focus on the ability to perform quantum many-body experiments in future. Then a brief overview of the main vacuum apparatus is given, together with an outline of the experimental sequence that is used to create samples of quantum degenerate gases. For a detailed list of devices, part numbers and components, the reader is referred to Appendix A.

2.1 Suitable constituents for creating quantum many-body systems

When setting up a new laboratory to study quantum many-body physics, the choice of quantum constituents – neutral atoms, ions, or molecules – is not an easy one.[1] Often there is a trade-off between the feasibility to prepare and manipulate ultracold samples on the one hand and the capability to perform interesting, novel experiments on the other.

[1] There are, of course, many more possible experimental systems but for simplicity only these three are considered here.

Neutral atoms

First to mention are neutral atoms which can be broadly characterised by four main properties: the atomic mass, the compound particle flavour[2] (boson, fermion), the feasibility to tune contact interactions [93], and the dominant type of interaction (short-range or long-range). Alkali atoms are relatively easy to cool[3] in large quantities but they lack intrinsic long-range interactions.

[2] If the number of neutrons is even, the compound particle (atom) is bosonic, otherwise it is fermionic. Stable isotopes of the elements are more commonly bosonic.

[3] this will be discussed later in section 3.1

Ions

In contrast to neutral atoms, ions are subject to the Coulomb repulsion and they offer long coherence times, suitable even for quantum information processing [94]. However, they are hard to cool en masse, the current record being around 200 ions [95].

Polar molecules

Furthermore, polar molecules are very interesting for quantum simulation applications since they feature long-range dipolar interactions [96], but unfortunately their cooling process involves serious technical challenges due to the plethora of rovibrational sub-levels.

2.2 Choice of atomic species

To date, the most successful large-scale quantum many-body experiments have been carried out using ultracold atoms in optical lattices, the prime example here being the observation of a quantum phase transition using ^{87}Rb-atoms [18]. In the following short review of atomic species we will therefore focus on neutral atoms.

The traditional atomic species that are best-suited for laser cooling are ^{87}Rb [97] and ^{23}Na [98] which were the first to be Bose-condensed.[4] However, these species lack readily accessible Feshbach resonances [93] limiting their feasibility for studying strongly-correlated systems.[5] This limitation can be overcome by using lithium [101] (^{6}Li/^{7}Li) or potassium [102, 103] (^{39}K/^{40}K) which feature broad, accessible Feshbach resonances and are suitable for investigating strongly correlated physics. In addition, both elements include a stable fermionic isotope (^{6}Li and ^{40}K), a crucial ingredient to study electron-like many-body systems, such as the Fermi-Hubbard model [104], as well as antiferromagnetic quantum magnetism [105, 106]. Going beyond the 'standard repertoire' in the alkalis there has been tremendous success in the past decade in reaching quantum degeneracy of species with various special properties. These include elements with two valence electrons, namely ytterbium [107, 108] and strontium [109–111], which possess singlet ground states with with zero electronic angular momentum, giving rise to intriguing SU(N)–symmetries and extremely narrow optical transitions. Furthermore, there are elements with very large magnetic moments, most notably dysprosium [112, 113] and erbium [114, 115], which give rise to dipolar interactions. Quantum degeneracy of these species (ytterbium, strontium, dysprosium, and erbium) has been reached with both their bosonic and their fermionic isotopes. However, the advantages of these species often come with some technical cost, for example in ytterbium and strontium: in order to perform laser cooling on narrow optical transitions a laser with a very narrow linewidth is required.

[4] together with ^{7}Li [99]

[5] Long-range interactions can nevertheless be engineered in few-particle systems by employing the Rydberg-blockade, highlighted by recent experiments on few-body quantum systems [100].

This experiment

The apparatus described in this thesis is designed to create a variety of novel lattice geometries. This requires a large degree of optical access, as well as reliable production of quantum degenerate samples without too much technical overhead. Therefore a well-established 'traditional' combination of atomic species was

chosen, namely rubidium (^{87}Rb) and potassium (^{39}K/^{40}K). The setup employs sympathetic cooling of potassium using ^{87}Rb as coolant; with a suitable laser system it is therefore possible to switch between ^{39}K and ^{40}K on a shot-to-shot basis using only software commands. All the experiments carried out in this work use ^{87}Rb and ^{39}K though we have also demonstrated a magneto-optical trap (MOT) of ^{40}K and the ability to easily switch between the two potassium isotopes. For a more detailed review of the atomic properties of ^{87}Rb and ^{39}K please refer to section 3.1.

2.3 *Vacuum apparatus*

The two most important design criteria for building a cold-atom apparatus today are optical access and cycle time. On the one hand, wide optical access allows flexibility of the type of experiments performed. In our case, this is imperative as we require four optical axes in one plane for the optical quasicrystalline lattice. On the other hand, a short (< 1 min) cycle time is beneficial for convenient experimentation and efficient optimisation of the apparatus.[6]

[6] and also for the sanity of the graduate students.

The 'Munich design' pioneered by Greiner et al. [116] combines the two requirements by separating a 'high-pressure' ($\sim 1 \times 10^{-9}$ mbar) MOT chamber with limited optical access from the science chamber ($\sim 1 \times 10^{-11}$ mbar) with excellent optical access. The two chambers are connected by an angled differential pumping section through which the atoms are transported magnetically. This well-established design is now being used in several laboratories, including LMU Munich [116–120], ETH Zurich [121], Harvard [122], and LPL (Paris) [123].

Our apparatus is shown schematically in Fig. 2.1. It is an adaptation of the latest iteration [119, 120] of the Munich design which contains an additional high-pressure ($\sim 1 \times 10^{-6}$ mbar) chamber for preparing a pre-cooled atomic beam (2D MOT). The main differences between their design and ours can be summarised as follows:

- We have two 2D MOT chambers, allowing independent control of the background vapour pressure for rubidium and potassium.
- The effective differential pumping section between the 2D MOT chambers and the MOT chamber is probably shorter than theirs.[7]
- The differential pumping section (20 cm) between the MOT chamber and the 'knee' is longer and its inner diameter (10 mm) is wider than theirs.
- Our science cell is a rectangular cuboid, allowing a more compact geometry of experiment coils.

[7] We ordered a titanium part with a 1.5 mm clearance over 50 mm length but the part we received has a 1.5 mm clearence only over 20 mm. The rest of the differential pumping section has a wider diameter (~ 3 mm). However, the pressure differential between 2D MOT chambers (which are not actively being pumped) and the MOT chamber has never been a limiting factor in our experiment and consequently a longer clearence would have been of no avail.

It should be noted that the large separation between the MOT chamber (7.2×10^{-11} mbar) and the science cell (1.2×10^{-11} mbar)

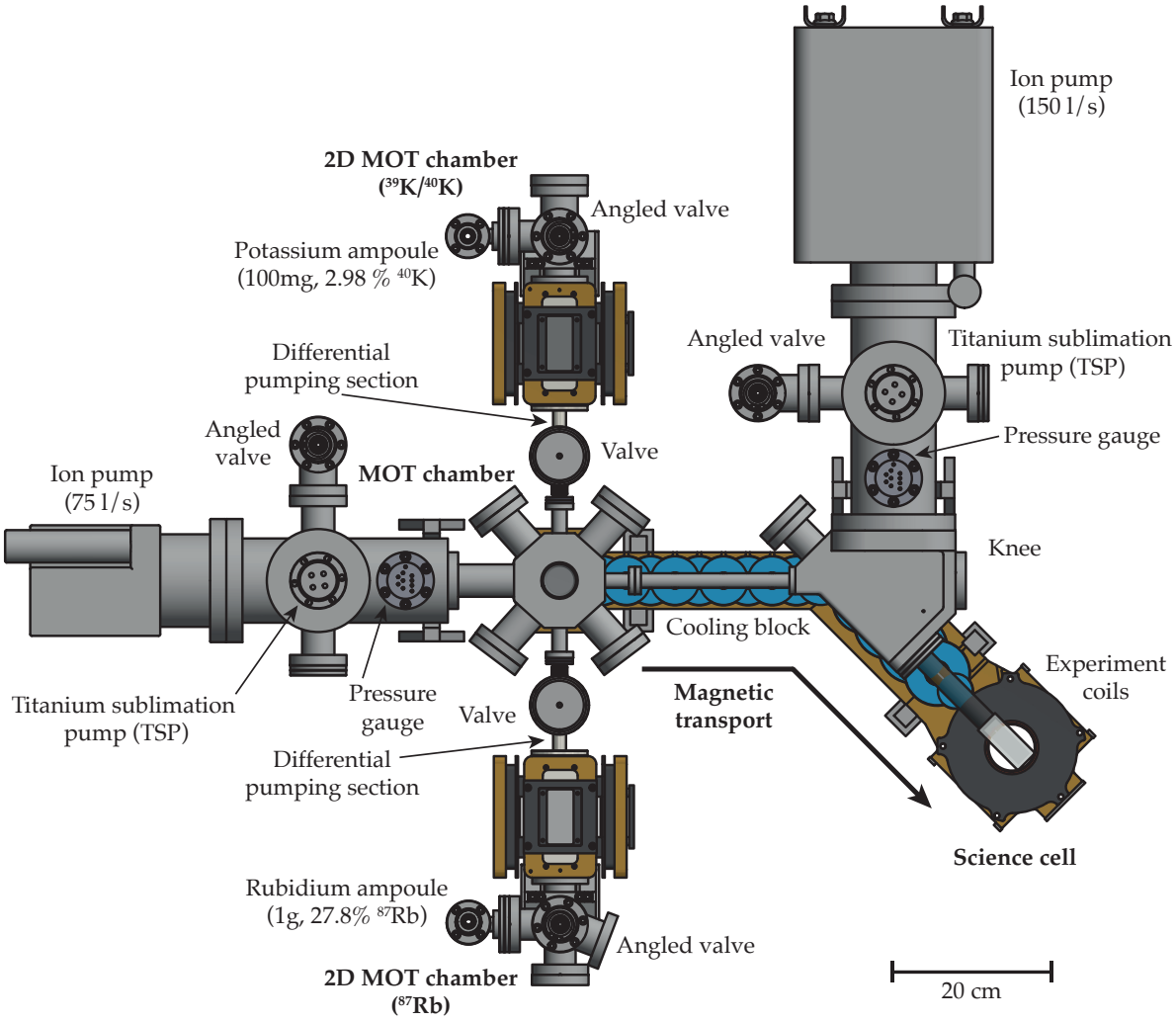

Figure 2.1: Schematic of the main experimental apparatus. For clarity, only the lower half of the cooling block and magnetic transport system (brass-coloured) is shown.

Table 2.1: Rough overview of the experimental sequence.

stage	duration	section
MOT	2.5 s	3.5
final MOT	10 ms	3.7
optical molasses	4.5 ms	3.8
optical pumping	0.7 ms	3.9
magnetic transport	5 s	3.10
MW evaporation	7.5 s	3.11
RF state transfer	20 ms	4.5
dipole evaporation	3 s	4.3
total	23 s	

is now mostly practical and not physically required since the pressure difference between the two chambers is only a factor of six. Nevertheless we can maintain efficient MOT loading, facilitated by a very large ($\sim 10^4$) pressure differential between the 2D MOT chambers and the MOT chamber.

A more comprehensive treatment of the design, implementation and characterisation of the vacuum apparatus can be found in Matteo Sbroscia's First-Year Report [124].

2.4 *Overview of the experimental sequence*

Table 2.1 provides a rough overview of the experimental sequence that is used to create quantum degenerate samples of ^{87}Rb and ^{39}K.

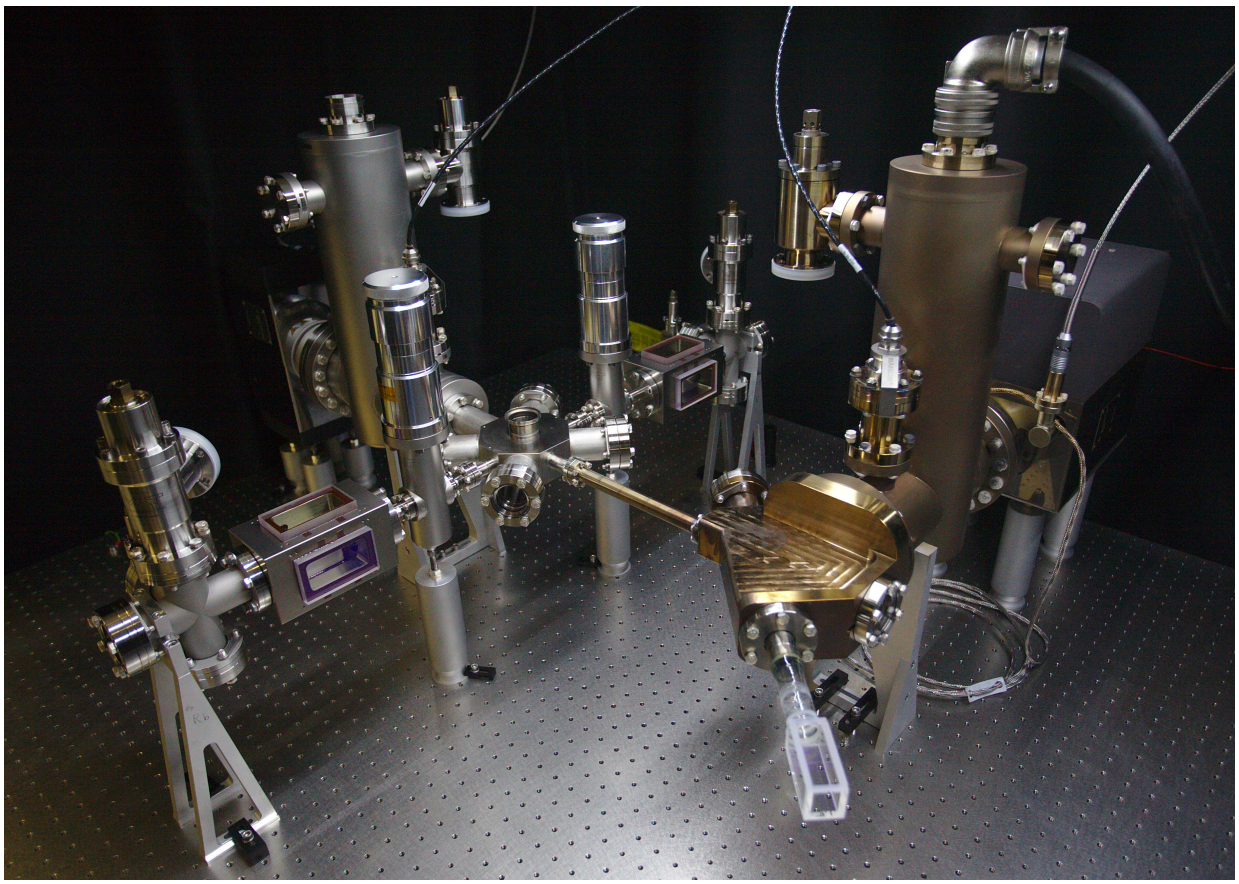

Figure 2.2: Completed vacuum setup (4^{th} July 2016). The photo was taken after bake-out had been completed, after the rubidium and potassium ampoules had been broken, and after the turbo-pump had been disconnected. The heavy cable of the titanium-sublimation pump (TSP) is still connected (top right).

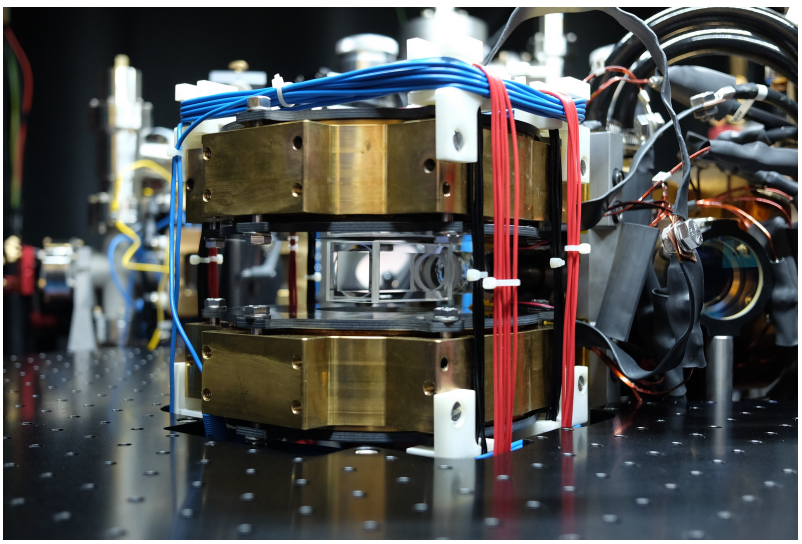

Figure 2.3: Science cell and brass cooling block seen from main breadboard (see also Fig. 5.17), before any optics have been placed on it (28^{th} February 2017). The ribbon-wire can be seen (black), connecting the upper and the lower experiment coil. The compensation coils are wound in red (T-axis), black (D-axis), and blue wire (Z-axis) on 3D-printed mounts.

3
Laser cooling & trapping of ^{87}Rb & ^{39}K

This chapter accompanies the atoms on their initial journey from room temperature to the µK-scale before we later present the detailed methods to reach quantum degeneracy in the optical dipole trap (Chapter 4). First, each atomic species and their relevant energy scales are introduced. Then the experimental methods to cool and trap these atoms are described. This chapter is focussed on our experimental implementation[1]; the theoretical introduction to each method is kept to a minimum. For a general introduction to the topic, the reader is referred to the standard literature [125–127].

[1] A detailed list of optical components can be found in Appendix A.

3.1 *The alkalis*

The inevitable starting point for any experiment involving ultracold gases is some kind of atom source at or above[2] room-temperature. Thankfully, the vapour pressures of rubidium and potassium are reasonable (see table 3.1) such that a small specimen (0.1 - 1.0 g) of each species in a vacuum chamber is sufficient to start the laser cooling cycle from background vapour.

Table 3.1: Vapour pressures for rubidium and potassium for two different temperatures [128].

T	Rb	K
295 K	3.8×10^{-7} mbar	1.7×10^{-8} mbar
333 K	1.6×10^{-5} mbar	1.0×10^{-6} mbar

[2] In many cases atoms have to first be heated to increase their vapour pressure.

Similar to atomic hydrogen, the ground level of the alkali atoms is the $^2S_{1/2}$-level of the valence electron. Since here the angular momentum quantum number L is zero, there is no fine structure splitting and consequently only the two hyperfine states $F = 1, 2$ are thermally populated at ambient temperature; The thermal energy required to significantly populate the excited electronic states is much higher than room temperature, as shown in table 3.4.

The hyperfine structure of the alkalis is very favourable for standard laser cooling techniques [126] due to the existence of (almost) closed transitions on the D_2-line ($^2S_{1/2} \rightarrow {}^2P_{3/2}$).[3] A transition is said to be 'closed' if it can be treated as an effective two-level system, neglecting decay into other (ground) states, e.g. by spontaneous emission. Other advantages include reasonable natural linewidths[4] and the commercial availability of lasers in the relevant wavelength-range (though in past decades laser technology has advanced considerably such that nowadays the availability of lasers is not usually a limiting factor).

[3] for a particular choice of F and m_F states

[4] wide enough for the transitions to be addressed with a conventional single-mode diode laser and narrow enough to have Doppler temperatures on the order of 100 µK

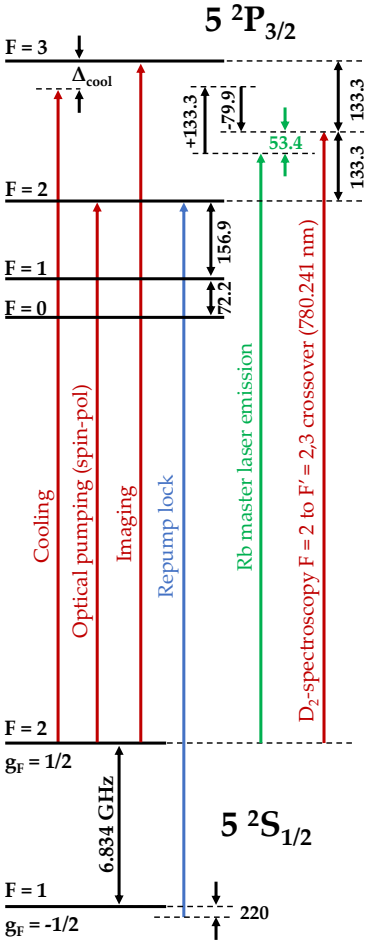

Figure 3.1: Hyperfine structure of the D_2-line transition in ^{87}Rb (not to scale)

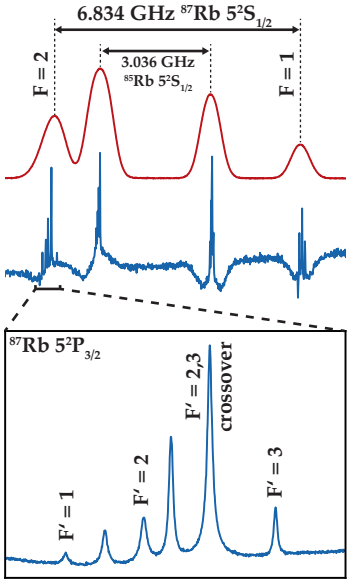

Figure 3.2: Rubidium D_2-line Doppler-free (blue) and Doppler-broadened (red) spectroscopy. The ^{87}Rb master laser is locked 53.4 MHz below (i.e. to the red of) the $F' = 2,3$ crossover line (see also Fig. 3.1).

Rubidium-87

In terms of aptitude for laser cooling ^{87}Rb is one of the most favourable atomic species (see also section 2.2) which is down to three main factors: Firstly, the hyperfine splitting of both the ground and the D_2-excited state is much larger than the natural linewidth ($6\,\mathrm{MHz}\times 2\pi$); therefore the individual hyperfine levels (and their crossovers) are nicely resolved by our spectroscopy (Fig. 3.2). Correspondingly the $|F = 2, m_F = 2\rangle \rightarrow |F = 3, m_F = 3\rangle$ ($^2P_{3/2}$) transition, driven by σ^+-polarised light, is almost perfectly closed and comparatively few repump photons ($F = 1 \rightarrow F' = 2$) are required to transfer atoms back to the cycling transition. This allows for a near-textbook-like implementation of magneto-optical trapping and optical molasses. Secondly, the atomic mass is relatively large, favouring thermalisation and reducing non-adiabatic ('Majorana'-)losses from magnetic traps. Thirdly, the background scattering length is relatively large and positive ($100\,a_0$), favouring fast thermalisation and BEC stability (section 4.6).

Potassium-39

In contrast to ^{87}Rb, the hyperfine splitting of the $4^2P_{3/2}$ level in ^{39}K is very narrow (Fig. 3.3, unresolved by our spectroscopy in Fig. 3.4), precluding a 'properly' closed transition and necessitating many more repump photons to combat this effect. Consequently, molasses-cooling is much less efficient than for ^{87}Rb. Additionally, its background scattering length is negative which means that an ultracold cloud of ^{39}K can collapse under its own inter-atomic attractive interactions [129]. However, ^{39}K possesses a readily accessible Feshbach resonance at 402.70(3) G [130] to counteract the negative effects of attractive interactions. This Feshbach resonance is indeed the main reason why ^{39}K is widely used for studying strongly interacting or non-interacting bosons [103, 131–136]. The well-established technique of sympathetic cooling with ^{87}Rb [103, 131, 132, 134] allows relatively straightforward production of quantum degenerate samples of ^{39}K. Although the sympathetic production might be in future superseded by all-optical production using the 'grey molasses' technique [129, 133, 137, 138] the presence of ^{87}Rb proved to be useful in our lab. It allowed us to benchmark the optical lattice in the early stages of the experiment before we achieved condensation with ^{39}K. Moreover, the experiment is designed to perform shot-to-shot switching between ^{39}K and fermionic ^{40}K in future, aided by the abundant ^{87}Rb-atoms for sympathetic cooling of either species.

So far the short review of atomic properties considered isolated atoms; in the following the effects of external fields will be briefly discussed.

Laser frequencies

The relevant optical transitions for laser cooling of ^{87}Rb and ^{39}K are shown in Fig. 3.1 and 3.3, respectively. In the following sections 3.5-3.9 the individual purpose of each laser frequency will be discussed in detail. Note that in ^{87}Rb the reference laser (green line in Fig. 3.1) is emitting 53.4 MHz to the red of the spectroscopy line, whereas in ^{39}K the reference laser is locked directly to the spectroscopy signal.

3.2 ^{87}Rb & ^{39}K in magnetic fields

In the presence of a magnetic field B the $(2F+1)$-fold degeneracy of m_F states within a given hyperfine level F is lifted. In the case of low field strengths the energy shift of an $|F, m_F\rangle$ state is linear, namely

$$\Delta E = g_F m_F \mu_B B \quad , \tag{3.1}$$

called the *anomalous Zeeman effect* [127]. Values for g_F can be found in Fig. 3.1 and 3.3 and μ_B is Bohr's magneton. For strong fields the $|F, m_F\rangle$ states cease to be good quantum numbers. In this case, the levels of ^{87}Rb or ^{39}K with $J = 1/2$ (for example) are split into two groups ($m_J = \pm 1/2$) of four, i.e. $2I+1$, where $I = 3/2$ (*Paschen-Back effect*). The hyperfine and magnetic splittings are plotted in Fig. 3.5 and 3.6 for ^{87}Rb and ^{39}K, respectively, in both the weak-field and the strong-field regimes. For levels with $L = 0$ and $S = 1/2$ the energies can be written in an analytic form called the *Breit-Rabi formula* [127, 139, 140].

Interlude: calibration of magnetic coils

The splitting of hyperfine states in magnetic fields represents the most accurate way of calibrating homogeneous magnetic fields in our apparatus. It is a well-understood, single-particle effect with no obvious systematic errors. The levels with $J = 1/2$ (e.g. the $5\,^2S_{1/2}$ ground level of ^{87}Rb) are particularly well suited for magnetic field calibration as they are unaffected by the electric quadrupole correction [139]. We can experimentally determine the transition frequencies at high magnetic fields (several hundreds of gauss) with a relative uncertainty of 10^{-4} using Landau-Zener sweeps or Rabi oscillations. By comparing the experimental values to the theoretical predictions (Fig. 3.5 B) we can quantify our magnetic field to similar precision. Table 3.2 shows some relevant calibrated field values using RF transitions from the $|F = 1, m_F = -1\rangle$ to the $|F = 1, m_F = 0\rangle$ state in the atomic ground level of ^{87}Rb (arrow in Fig. 3.5 B). The calibration of our guide field coils can be found in section 4.5 using the same method.

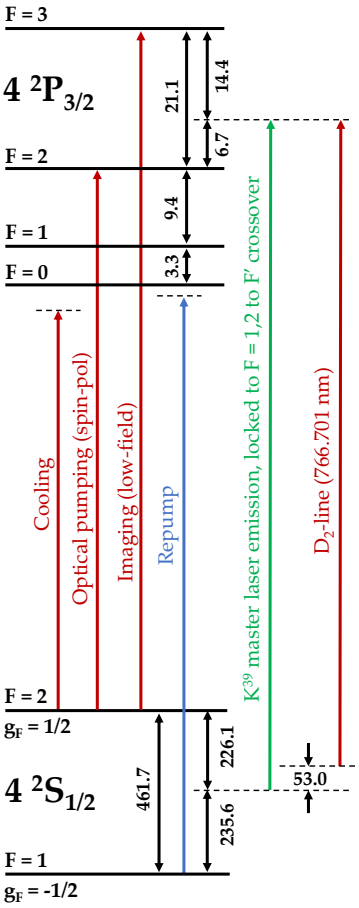

Figure 3.3: Hyperfine structure of the D_2-line transition in ^{39}K (not to scale). Note the unequal distances between the lock point on the two hyperfine ground levels.

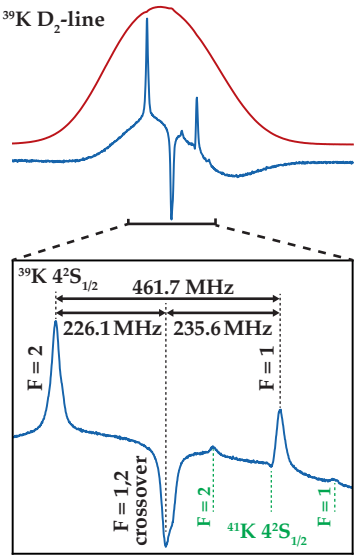

Figure 3.4: Potassium D_2-line Doppler-free (blue) and Doppler-broadened (red) spectroscopy. The ^{41}K lines are indicated in green. We lock on the $F = 1, 2$ crossover line which has an assymetric line shape.

3.3 *Spectroscopy and absolute frequency stability (laser locking)*

The production and manipulation of ultracold ^{87}Rb & ^{39}K requires an absolute laser frequency stability (long-term and short-term) of roughly 1 MHz, corresponding to a relative stability on the order of 10^{-9}. This requirement means that the laser jitters and drifts by much less than the natural linewidth (6 MHz$\times 2\pi$) of the relevant optical transitions. In our case the short-term fluctuations (linewidth) of the free-running reference laser is in the 100 kHz-range. However, the long-term (thermal) fluctuations are on the order of 100 MHz such that a stable reference and a frequency-feedback-loop ('laser lock') are necessary. Absolute frequency stability for our ^{87}Rb- and ^{39}K-master lasers is achieved using standard saturated absorption spectroscopy and commercial Pound-Drever-Hall locking electronics which will be briefly described in the following. Relative frequency stability between separate laser diodes and the master lasers is ensured using frequency-offset-locks (see section 3.4 below).

Table 3.2: Magnetic field calibration for our experiment coils using RF transitions from the $|F = 1, m_F = -1\rangle$ state to the $|F = 1, m_F = 0\rangle$ state in ^{87}Rb. For each current value we take an RF-resonance scan using a Landau-Zener sweep with a half-range of 50 kHz and a duration of 20 ms. These frequencies are then converted to magnetic field values using the magnetic field hamiltonian (Fig. 3.5 B).

Current/A	RF res./MHz	B-field/G
29.257	228.825	317.68(9)
32.379	253.600	351.44(9)
36.600	287.213	397.19(9)
36.650	287.650	397.78(9)

Table 3.3: Spectroscopy, laser locking parameters and lock performance. The linewidths are measured with the 'EagleEye' reference cavity.

parameter	^{87}Rb	^{39}K
vapour cell temp.	50°C	80°C
optical power/mW	~ 1	$\sim$1.4
modul. freq./kHz	28.00	20.00
modulation ampl.	0.012 mA	
laser linewidth/kHz	155	120

Saturated absorption spectroscopy

The saturated absorption spectroscopy technique [141–144] overcomes Doppler-broadening by employing the pump-probe beam configuration. In our apparatus we have a commercial spectroscopy unit (one for each atomic species) which supplies a fibre-coupled pump-probe setup and a vapour cell. We obtain a spectroscopic absorption signal (y-axes in Figs. 3.2 and 3.4) by scanning the laser piezo (x-axes) together with the diode current ('feed forward') using a triangular wave.

Laser locking

The master lasers are locked to spectroscopy lines using top-of-fringe (Pound-Drever-Hall [145]) locking which is insensitive to laser intensity fluctuations. The Pound-Drever-Hall technique uses a weak (typically 5×10^{-4}) modulation of the diode current at a frequency around 20 kHz to imprint sidebands onto the laser frequency. The spectroscopy signal is mixed down with the same 20 kHz at a fixed phase delay to produce an error signal that represents the derivative of the spectroscopy signal. This is then used to stabilise the laser frequency with a proportional-integral-derivative (PID) loop. We choose the most pronounced spectroscopy features as they promise the largest feedback slopes and the best locking performance; in ^{87}Rb we use the $F = 2 \rightarrow F' = 2, 3$ crossover [127] line (Fig. 3.1), the ^{39}K-laser is locked to the $F = 1, 2 \rightarrow F'$ crossover line, as shown in Fig. 3.3. The parameters used for laser locking are itemised in table 3.3, together with the lock performance.

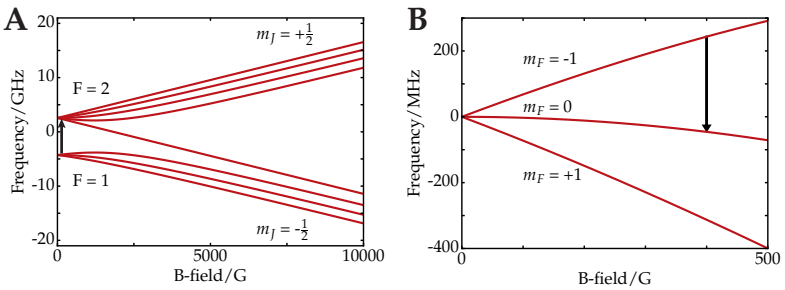

Figure 3.5: Hyperfine and magnetic splitting of electronic levels in ^{87}Rb. (**A**) $5\,^2S_{1/2}$ level. In the presence of a weak magnetic field the $(2F+1)$-fold degeneracy of each hyperfine level F= 1, 2 is lifted. For strong fields the lines are split into two groups ($m_J = \pm 1/2$) of four ($2I+1, I = 3/2$). (**B**) $5\,^2S_{1/2}$ F = 1 (ground) level in the low-field regime. The black arrows indicate the magnetic dipole transitions which can be stimulated by RF-radiation in order to calibrate magnetic fields (**B**), or perform MW evaporation (**A**), as discussed in section 3.11.

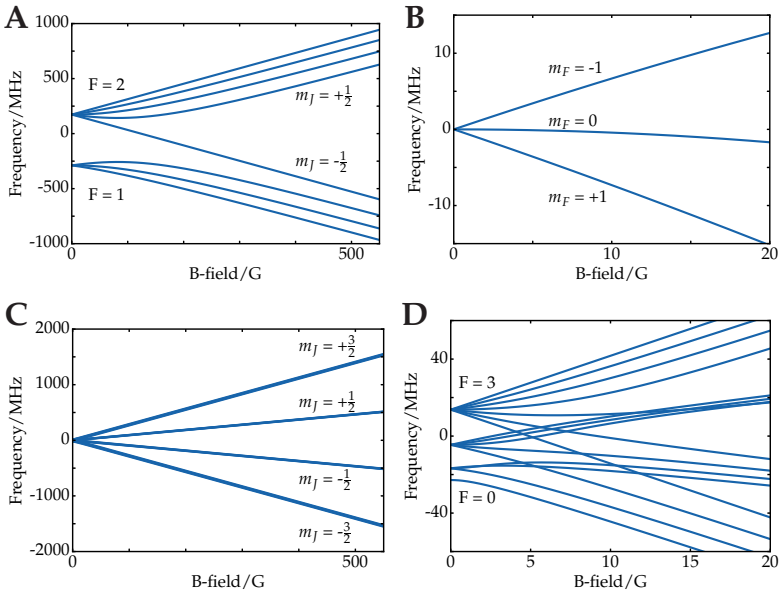

Figure 3.6: Hyperfine and magnetic splitting of electronic levels in ^{39}K. (**A**) $4\,^2S_{1/2}$ level. (**B**) $4\,^2S_{1/2}$ F = 1 hyperfine (ground) level in the low-field regime. (**C**) $4\,^2P_{3/2}$ (D2-excited) level. There are 16 m_F states which are not resolved on this scale. In the strong-field regime the states are grouped by m_J, each containing four m_I states, i.e. $2I+1$, where I = 3/2. (**D**) $4\,^2P_{3/2}$ (D2-excited) level (same as **C**) at weak magnetic fields. Each hyperfine level F = 0,1,2,3 is split into m_F states $(2F+1)$.

	hierarchy	transition	λ/nm hc/E	frequency E/h	B-field/G E/μ_B	temperature $E/(k_B T)$
^{87}Rb	'gross'	$5\,^2S_{1/2} \rightarrow 5\,^2P_{3/2}$ (D_2)	780.241 210	384.230 484 THz	3×10^8	18 000 K
	fine	$5\,^2P_{1/2} \rightarrow 5\,^2P_{3/2}$ (D_1-D_2)		7.123 THz	5×10^6	342 K
	hyperfine	$5\,^2S_{1/2}\ F = 1 \rightarrow F' = 2$		6.834 682 611 GHz	4900	0.3 K
		$5\,^2P_{3/2}\ F = 2 \rightarrow F' = 3$		266.650 MHz	191	13 mK
^{39}K	'gross'	$4\,^2S_{1/2} \rightarrow 4\,^2P_{3/2}$ (D_2)	766.700 921	391.016 170 THz	3×10^8	19 000 K
	fine	$4\,^2P_{1/2} \rightarrow 4\,^2P_{3/2}$ (D_1-D_2)		1.730 THz	1×10^6	83 K
	hyperfine	$4^2S_{1/2}\ F = 1 \rightarrow F' = 2$		461.720 MHz	330	20 mK
		$4^2P_{3/2}\ F = 2 \rightarrow F' = 3$		21.1 MHz	15	1 mK

Table 3.4: Hierarchy of some relevant energy scales (E) and energy-equivalents in ^{87}Rb [139] and ^{39}K [140].

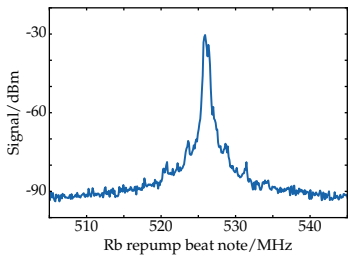

Figure 3.7: Frequency scan of the beat note (after mixing) between the Rb repump and the Rb master laser. A lorentzian fit to the peak gives a centre frequency of 526.1 MHz. The measurement bandwidth of the spectrum analyser was set to 1 kHz for this measurement.

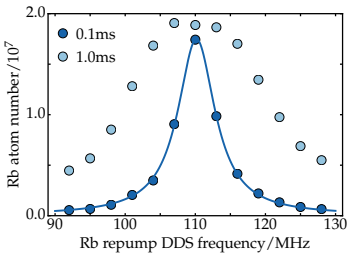

Figure 3.8: Frequency scan of Rb repump flash (during imaging) for two different pulse durations. Note that the DDS unit drives an AOM in double-pass configuration, i.e. the laser frequency is changed by twice the amount shown on the x-axis. The atom numbers are 2d gaussian fits to the atom cloud after loading the dipole trap at a temperature of 6 µK in 12ms ToF. The repump flash is applied 1.5 ms before the imaging pulse in order to optically pump the atoms from the $|F = 1, m_F = -1\rangle$ state to the $F = 2$ manifold. The lorentzian fit (line) gives a centre frequency of 110.1(1) MHz with a Γ-width of 6.5(1) MHz.

3.4 *Relative frequency stability (offset locking)*

Frequency shifts on the order of 100 MHz are routinely performed by acousto-optic modulators (AOMs). Their radiofrequency (RF) bandwidths of up to ±20 % of the central frequency are sufficient to tune the frequency by several natural linewidths in ^{87}Rb or ^{39}K (particularly if used in the convenient double-pass configuration). However, for the two situations described below we require larger frequency shifts or wider tuning ranges, which can be achieved using an 'offset lock' [146]. In this configuration the laser that is to be stabilised is overlapped (on a non-polarising beam-splitter) with a reference laser and the resulting beat note is picked up on a high-bandwidth photodiode. The beat signal can be mixed down with an external RF source, for example a voltage-controlled oscillator (VCO) or a direct-digital-synthesis (DDS) unit if frequency tuning is required. Afterwards the signal is split into two paths with different cable lengths, then recombined on a mixer and finally low-passed. The resulting DC voltage can be approximated by a cosine [146], the argument of which is given by the offset frequency times the constant time delay (= length/speed of light) induced by the longer cable. Therefore this setup is sometimes called 'delay-line lock'. Laser locking is then achieved by using a side-of-fringe lockpoint of the cosine as the error signal for the PID-loop. In our experiment this technique is used for two applications, namely the rubidium repump lock and the potassium imaging lock.

Rubidium repump lock

The ground state splitting in ^{87}Rb is 6.8 GHz (table 3.4) and in our experiment it is bridged by an offset lock. In this setup the raw beat signal is first mixed down with a 7.5 GHz reference oscillator to make the RF signal easier to handle. We choose a (constant) lockpoint 220 MHz to the blue of the repump transition $F = 1 \rightarrow F' = 2$ in ^{87}Rb , frequency fine-tuning is then achieved by a double-pass 110 MHz AOM (-1st order, Fig. 3.8). Since our rubidium master laser is locked 53.4 MHz to the red of the crossover line (Fig. 3.1) we should set our beat note (after mixing down with the reference oscillator) to

$$7500.0 - (6834.7 - 133.3 + 53.4) - 220.0 = 525.2 \qquad (3.2)$$

(in MHz). In practice we have a beat note (after mixing) of 526.1 MHz, as shown in Fig. 3.7. In Fig. 3.8 we show a spectroscopic measurement of the resulting repump laser frequency which is consistent with the above considerations. This measurement was performed using the 'repump flash' (see section 3.12) during imaging of the $|F = 1, m_F = -1\rangle$ state in the dipole trap. Since our main imaging light is only resonant with atoms in the $F = 2$ level the measured atom number is a good probe of the repump frequency, resulting from the optical pumping efficiency from $|F = 1, m_F = -1\rangle$ to

F = 2. For longer repump flash pulses we observe a broadening effect similar to that of power broadening.

Potassium imaging lock

The ground level hyperfine splitting of ^{39}K is only 462 MHz (table 3.4) and that of ^{40}K is 1.3 GHz which could, in principle, be bridged by AOMs. However, we require a much larger degree of flexibility than could be achieved by AOMs, since ^{39}K is often imaged at magnetic fields close to the Feshbach resonance at 402.70 G (see section 4.6 on Feshbach resonances). In ^{39}K the corresponding frequency shifts are between 200 and 500 MHz to the red of the master laser; in ^{40}K the shifts are even larger and of opposite sign (to the blue, since the ground state hyperfine splitting is inverted). Offset locks allow large tuning ranges of arbitrary sign and are therefore ideally suited for this application.

In contrast to rubidium, we mix the beat signal with a DDS signal (which in turn has been mixed with a VCO to cover higher frequencies) such that we can vary the lockpoint in-sequence. Figure 3.9 shows the beat signal between the potassium master laser and the imaging laser. By changing the DDS frequency we are able to obtain a spectroscopic signal of the ^{39}K imaging transition $F = 2 \rightarrow F' = 3$ at low magnetic field, as shown in Fig. 3.10. It crucial to use σ^+ polarised imaging light in order to address the correct hyperfine state (Fig. 3.10 also shows a frequency scan using the wrong polarisation, in this case the resonance is shifted in a non-trivial manner). The expected imaging transition at 2.8 G is at 155.5(2) MHz to the red of the D_2-line (fine structure point). Taking into account the position of the ^{39}K master lock point (Fig. 3.3) we expect the imaging transition at

$$-155.5\,\text{MHz} - 53.0\,\text{MHz} = -208.5\,\text{MHz} \quad , \tag{3.3}$$

in excellent agreement with the measured value of 208.6 MHz (Fig. 3.10).

Up to this point the stage is set for the atoms, and their journey towards quantum degeneracy begins. In the following the individual cooling steps will briefly introduced and subsequently described with the focus on our experimental implementation. However, schematics of large-scale laser setups and lists of optical components, part numbers, etc. have been omitted in favour of readability.

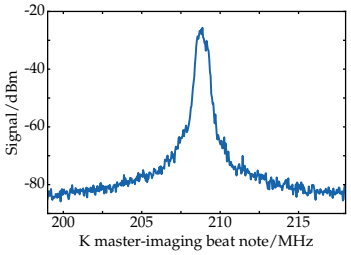

Figure 3.9: Spectrum analyser trace of the beat note between the ^{39}K imaging and the ^{39}K master laser corresponding to the highest data point in Fig. 3.10 below. The measurement bandwidth of the spectrum analyser was set to 1 kHz for this measurement.

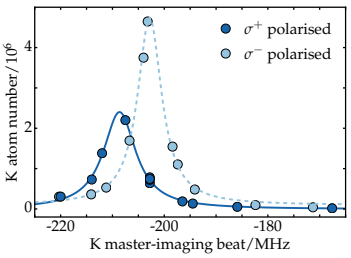

Figure 3.10: Frequency scan of ^{39}K imaging light at a guide field of 2.8(1) G (offset coils at 4.5 A), using σ^+ and σ^+ polarised light. Only the σ^+ polarised light results in a faithful resonance signal at $-208.6(1)$ MHz (lorentzian fit) with a Γ-width of 7.6(5) MHz. The dashed line is a lorentzian fit to the σ^- data (wrong polarisation) as a guide to the eye. The frequency is red-detuned with respect to the potassium master laser (indicated by the negative values on the x-axis). The atom numbers (y-axis) are 2d gaussian fits to the atom cloud after loading the dipole trap at a temperature of 9 µK in 3ms ToF.

3.5 *Magneto-optical trap (MOT)*

Radiation pressure can be used to cool dilute vapours by means of the Doppler effect. This was discovered as early as 1975 by Hänsch and Schawlow [147]:

> It is well known that light exerts a radiation pressure on any substance which reflects or scatters is. [...] the radiation pressure of laser light has been used to selectively deflect atoms of a chosen isotopic species from a beam. We wish to point out that if the laser radiation is essentially isotropic, but confined to frequencies on the lower half of the Doppler-broadened absorption line of an atomic vapour, the gas can be cooled. That is, the average translational kinetic energy of the atoms can be reduced.

If the light is red-detuned with respect to the atomic transition, only atoms moving against the direction of the laser beam will predominantly experience photon momentum kicks and thereby be slowed down. Adding a weak magnetic quadrupole field[5] to this situation leads to atoms that are further away from the field minimum (i.e. the centre of the quadrupole field) reaching the resonance condition more easily than atoms at the field minimum. Therefore the atoms experience an effective restoring (i.e. trapping) force towards the centre. This is the principle of the magneto-optical trap (MOT) which nowadays forms the basis of essentially all cold-atom experiments [125–127].

All laser light required for MOT operation and the subsequent near-resonant cooling stages is derived from the respective reference lasers (section 3.3). Frequency shifts are performed by means of double-pass AOMs which are driven by home-built DDS units and RF amplifiers. Subsequently the light is amplified using six separate tapered-amplifiers (TAs). The rubidium and the potassium light is overlapped using 'magic' waveplates[6] and then distributed via a commercial two-input-by-six-output setup called 'fibre cluster'. Due to the nature of the polarising beam splitters in

[5] weaker than would be necessary to trap the atoms against gravity

Table 3.5: MOT parameters. Laser powers are given per beam. Detunings are given in MHz from the respective transitions (negative values mean red detunings).

parameter	^{87}Rb	^{39}K
backgr. pressure	7×10^{-11} mbar	
loading duration	2.5 s	1.0 s
gradient (strong ax.)	20 G/cm	
coil current	11.0 A	
gradient @ 1 A	1.78 G/cm	
cooling transition	$F = 2 \rightarrow F' = 3$	
repump transition	$F = 1 \rightarrow F' = 2$	
cooling power/mW	95-130	40-46
repump power/mW	0.7-1.0	60-87
cool. detuning/MHz	-23	-52
rep. detuning/MHz	0	-25
beam waist	13 mm	

[6] which act as λ-plate at 767 nm and as $\lambda/2$-plate at 780 nm

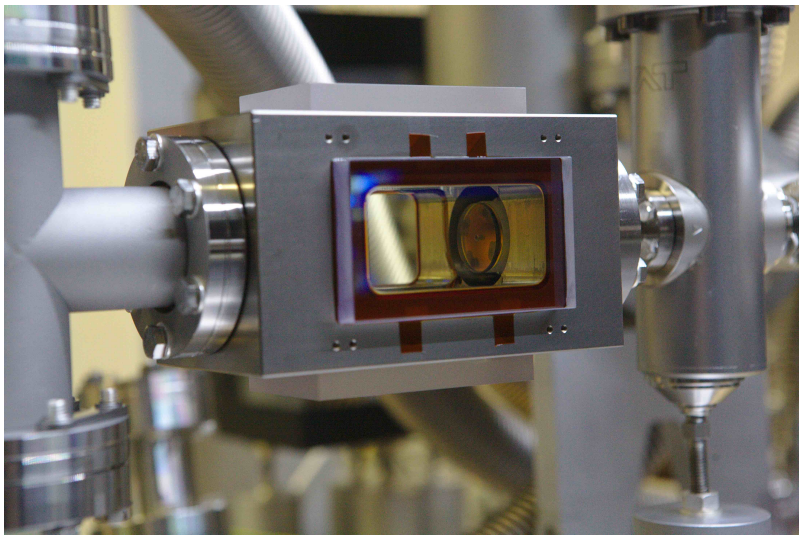

Figure 3.11: 2D MOT vacuum chamber. The frame is made of titanium and the rectangular windows are made of BK7 glass. The windows are glued to the frame using high-temperature exopy glue, with some kapton foil as spacer material. Inside the chamber (on the right) the mirror-polariser setup with its small aperture (see text) can be seen. All materials were chosen such that their respective thermal expansion coefficients match within 15 % [124].

the fibre cluster it is impossible to split the light from both input ports into six equal parts. Therefore the waveplates in the fibre cluster have been used to maintain pair-wise-balanced powers (at least within 10 %, typically better than 5 %) for both inputs. The MOT laser beams are large (table 3.5) and therefore relatively insensitive in terms of alignment, as long as they are roughly central, collimated and counter-propagating. We aligned one beam of each counter-propagating pair by coupling the light into a fibre plugged into the opposite fibre coupler. A list of relevant parameters is given in table 3.5.

The weak magnetic field gradient is provided by the same coils that are later used for magnetic transport (section 3.10). In addition, there are three pairs of compensation coils (section 3.8) which counteract stray magnetic fields.

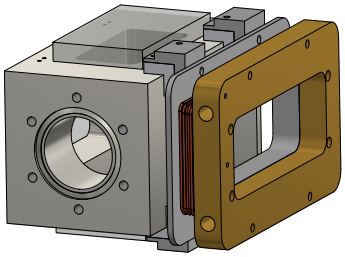

Figure 3.12: Schematic of the 2D MOT chamber showing one of the four coils. The brass block on the outside contains a U-shaped hole which is perfused by cooling water in order to carry away the heat dissipated by the coil. Figure taken and adapted from ref. [124].

3.6 2D MOT

Due to the low pressure in the MOT chamber (7×10^{-11} mbar) we observe no spontaneous MOT loading from background vapour. Instead, the MOT is loaded using two 2D MOTs [148–152] which are located on either side of the MOT chamber, each separated by a differential pumping section that maintains a large pressure differential (as described in section 2.3, see also Fig. 2.1). Separate 2D MOTs allow us to control the background vapour pressure for each species independently, leading to improved loading rates compared to refs. [119, 120]. These 2D MOTs are used to precool the atoms and produce a collimated beam[7] of ^{87}Rb/^{39}K-atoms that can be directly captured by the main '3D MOT'. The basic principle of the 2D MOT is the same as that of the 3D MOT, except that there is one direction along which less cooling takes place.[8] In our 2D MOT design (Fig. 3.11) this manifests itself by an elongated geometry[9] and by an aperture in the axial retro-mirror through which atoms leave the chamber. In addition, a polariser is glued to the face of the retro-mirror (with some added spacers, as shown in Fig. 3.11). The purpose of the axial beam is then twofold: On the one hand, it provides some cooling in the axial direction (though this contribution is limited due to the ring-shaped beam profile coming back from the retro-mirror). On the other hand, the central part of the axial beam serves to 'push' atoms towards the 3D MOT. The mirror-polariser setup allows us to balance the relative strength of cooling and pushing by changing the (linear) polarisation of the incoming axial beam. For potassium we have an additional laser beam along this axis that is blue-detuned in order to push the atoms through the aperture. In contrast to the 3D MOT all beams are retro-reflected. A summary of relevant 2D MOT parameters is given in table 3.6.

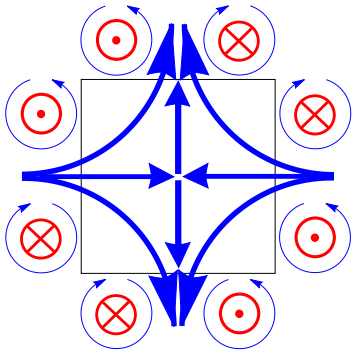

Figure 3.13: 2D MOT field configuration seen from the axial direction. Figure taken and adapted from ref. [124].

[7] this method was also proposed in the original paper by Hänsch and Schawlow [147]

[8] Sometimes this is called a 2D$^+$ MOT since cooling also takes place along the third direction. However, the notion of cooling along the third axis depends on the precise relative power levels between the different axes. In this work the term 2D MOT will be used for simplicity.

[9] there is no magnetic field gradient along this axis and hence no restoring force

The 2D MOT vacuum chambers were assembled in-house, closely following the Munich implementation [153, 154]. The elongated geometry of the 2D MOT is intended to provide a large

Table 3.6: 2D MOT parameters. Laser powers are given per beam. Detunings are given in MHz from the respective transitions (which are identical to those in the MOT). Negative frequency values mean red detunings. Here x and y directions are parallel to the transport axis and along gravity, respectively.

parameter	^{87}Rb	^{39}K
vapour pr./mbar	4×10^{-7}	1×10^{-6}
diff. pumping ⌀	1.5 mm	
diff. pump. length	2 cm	
duration	2.5 s	1.0 s
field gradient	21 G/cm	22 G/cm
coil current	8.5 A	9.0 A
gradient @ 1A	2.4 G/cm	
coil windings	63 per coil	
heat dissipated	30 W per coil	
comp. windings	8 per coil	
comp. current x	0.0 A	2.5 A
comp. current y	2.5 A	0.6 A
cooling detuning	−19 MHz	−28 MHz
repump detuning	0 MHz	−15 MHz
push detuning	-	+42 MHz
cooling power x	230 mW	190 mW
cooling power y	320 mW	260 mW
repump power x	48 mW	230 mW
repump power y	39 mW	170 mW
axial cooling	8.5 mW	∼1 mW
push power	-	2.0 mW
beam waist (long)	20 mm	
beam waist (short)	10 mm	
axial beam waist	2 mm	
push beam waist	-	0.8 mm

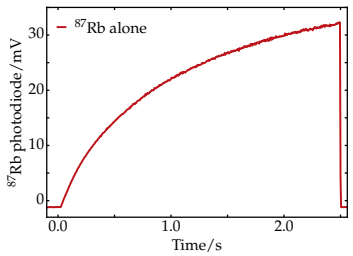

Figure 3.14: Fluorescence signal for MOT loading without potassium (rubidium only).

capture volume (though this effect cannot easily be quantified). A detailed account of the design and setup of our 2D MOT chambers can be found in Matteo Sbroscia's First-year report [124].

The magnetic gradients in each 2D MOT are provided by four rectangular coils, one on each face of the chamber, as shown in Fig. 3.12. They produce a quadrupole-like field in the plane perpendicular to the axial direction (Fig. 3.13); field gradients in the axial direction are negligible. Since considerable power is dissipated by the 2D MOT coils (table 3.6) they are water-cooled in parallel with the transport coils (section 3.10).

The alignment of the axial beam (and its counter-propagating partner) is crucial for proper operation of the 2D MOT. A good alignment technique is to first roughly maximise transmission of the axial beam through the whole apparatus (coming out of the opposite 2D MOT chamber). At this point the reflected, ring-shaped beam should exit the entrance viewport which can be made visible by holding a viewing card with a hole in place. Probably the retro-reflected beam is then not exactly overlapped with the incoming beam. This can be achieved by further beam-walking, whilst keeping the ring-shaped profile approximately constant. The alignment of the transverse beams is not crucial; it has almost no effect on the MOT loading rate provided that the beams are collimated and roughly counter-propagating.

Fluorescence signal

In order to characterise the loading of the MOT we monitor its fluorescence. Scattered light is collected on a lens at a vacuum viewport on the knee (Fig. 2.1), focussed, split into two parts, and filtered by wavelength before it reaches a photodiode (one for each species).Typical scope traces are shown in Figs. 3.14, 3.15, and 3.16.

In potassium the optical powers for repump and cooling light are comparable since the upper hyperfine levels are closely spaced (Fig. 3.3) and there is no closed transition. The necessity for higher laser powers leads to increased photon scattering and therefore limits the achievable temperatures in a ^{39}K-MOT to values well above the Doppler-limit [127] of 145 µK. Additionally, we expect light-assisted collisions to play a role in the comparatively modest performance of the ^{39}K-MOT in the presence of ^{87}Rb [155, 156]. Compared to the ^{39}K-only case (Fig. 3.15) we load roughly half as many ^{39}K-atoms if rubidium is present (Fig. 3.16). However, the rubidium is almost unaffected by the potassium; this is important because we rely on abundant ^{87}Rb-atoms as coolant to reach quantum degeneracy in ^{39}K (section 4.3).

3.7 *Final MOT stage in potassium*

Once loading of potassium is saturated (Fig. 3.16) we address the problem of strong photon (re-)scattering (described above) by lowering the ^{39}K-repump power in the final 10 ms of the MOT. During this 'final MOT' stage we linearly decrease the ^{39}K-repump power to 2 % of its original value. Additionally, we decrease the detuning of the ^{39}K-cooling light to -28 MHz at the beginning of the final MOT stage (the repump detuning remains essentially unchanged). We observe a significant increase in ^{39}K atom number using this procedure. Explaining this effect in detail is non-trivial due to the complexity of the process (dual species MOT, non-equilibrium system, unresolved ^{39}K-hyperfine structure). However, the most plausible explanation seems that of a 'temporal' dark MOT [118, 157, 158] in which further heating due to photon (re-)scattering is reduced by ^{39}K-atoms accumulating in the dark F = 1 hyperfine level.

Several experiments on ^{39}K have found that increasing the MOT gradient during the final MOT stage ('compressed MOT' or cMOT [159]) has a positive effect on the MOT performance [120, 135, 160]. Other experiments (on lithium) have found the opposite to be true [161]. Yet different experiments (on rubidium) have shown a somewhat chaotic behaviour to produce the best results [162]; they employ an artificial neural network to perform multiparameter optimisation of the final MOT stage. In our case we observe strong fluctuations in the system when increasing the MOT gradient and consequently we leave the MOT gradient unchanged in this stage of the experiment. Similarly, there seems to be no consensus as to whether the detuning of the cooling light should be increased [120, 135] (i.e. shifted away resonance), decreased [160], or modulated in a non-trivial manner [162]. We find decreasing the detuning of the cooling light (shifting its frequency towards resonance) results in the best performance.

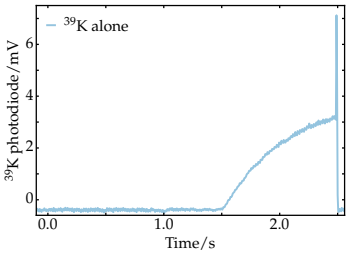

Figure 3.15: Fluorescence signal for MOT loading without rubidium (potassium only).

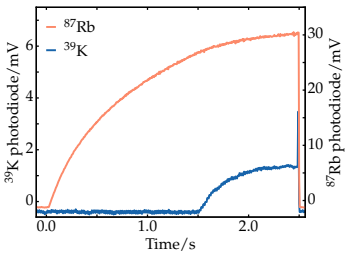

Figure 3.16: Fluorescence signal for MOT loading with both species present. (oscilloscope on high-resolution mode for all these measurements).

3.8 *Optical molasses*

A typical ^{87}Rb-^{39}K-MOT contains on the order of one billion atoms of each species at temperatures in the millikelvin-regime. The standard procedure to reach colder temperatures is the optical molasses technique [163, 164]. Its setup is identical to that of the MOT except that all magnetic field gradients are switched off. On the one hand, this means there is no restoring force towards the centre and consequently the atoms are not trapped any longer. Consequently the duration of this cooling procedure is limited to a couple of milliseconds. On the other hand, polarisation-gradient cooling mechanisms [165] which were previously confined to the trap centre are now happening across the entire atomic cloud. The latter effect is so strong that within 4.5 ms the temperature of the cloud drops by almost a factor of ten. Our experimental parameters are summarised in table 3.7.

Table 3.7: Molasses parameters. Laser powers are given per beam. Detunings are given in MHz from the respective transitions, which are the same as for the MOT (negative values mean red detuning).

parameter	^{87}Rb	^{39}K
duration	4.5 ms	
cooling power	26-35 mW	16-18 mW
repump power	0.7-1.0 mW	1.9-2.8 mW
cooling detuning	-63 MHz	-4 MHz
repump detuning	0 MHz	-45 MHz

Table 3.8: MOT compensation coil parameters. Here we use the convention that the x-axis (yellow wire) coincides with the direction of magnetic transport, the y-axis (blue) points along the axial direction of the 2D MOTs, and the z-axis (grey) is aligned with gravity. The coils for optical pumping (spin-polarisation, s-p) are also wound on the z-axis (black wire). The number of windings is given *per coil*, the conversion factor between field and current in G/A, and the optimum current values in A.

parameter	x	y	z	s-p
windings	6	$5\frac{3}{4}$	6	15
conversion (G/A)	0.4	0.4	0.37	0.92
current/A	1.5	1.5	0.0	-

Table 3.9: Optimum parameters used for optical pumping of ^{87}Rb. Detunings are given in MHz from the unshifted transitions (at zero field). Negative values mean red detuning.

parameter	value
total duration	0.7 ms
pumping duration	100 µs
repump duration	45 µs
offset field	10 G
pumping detuning	−3 MHz
repump detuning	+4 MHz
pumping power	1.5 mW
repump power	0.4 mW
beam waist	3 mm

[10] since local field maxima are precluded by Earnshaw's theorem [124]

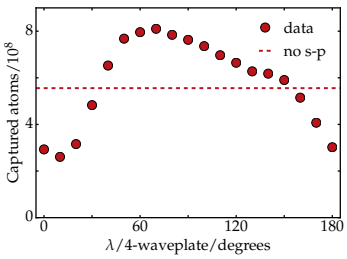

Figure 3.17: Optical pumping efficiency. The number of captured atoms is plotted as a function of pumping-polarisation ($\lambda/4$-waveplate) in ^{87}Rb. Atom numbers are gauss sum fits to fluorescence images in 5 ms ToF after release from the magnetic trap. The minimum (maximum) atom numbers correspond to almost σ^+ (σ^-) polarisation, probably with some residual ellipticity.

MOT compensation coils

During optical molasses any residual magnetic field gradients can lead to directional forces and thus inefficient cooling. Therefore we use three pairs of 'compensation coils' to counteract stray magnetic fields caused by ion pumps, optical isolators, and Earth's magnetic field. The compensation coil parameters are listed in table 3.8; the optimum current values were found by maximising the number of atoms after transport. Changing the compensation fields has negligible effect on the cloud temperature after transport. The optical isolators for the lattice are the dominant source of stray fields (by a factor of two) since placing them caused a sizeable shift in the optimum currents.

3.9 *Optical pumping (spin-polarisation)*

After optical molasses the atoms need to be magnetically trapped and transported to the science cell for further (evaporative) cooling. Only weak-field seeking m_F states (i.e. states with a positive zeeman shift, $g_F \times m_F$ positive in Eq. 3.1) can be trapped using magnetic forces.[10] In the electronic ground levels of ^{87}Rb and ^{39}K there are three trappable states: $|F = 2, m_F = 1, 2\rangle$ and $|F = 1, m_F = -1\rangle$. After the optical molasses stage we optically pump the ^{87}Rb atoms into the $|F = 1, m_F = -1\rangle$ state using a flash of σ^- polarised pumping ($F = 2 \rightarrow F' = 2$) and repumping light ($F = 1 \rightarrow F' = 2$). Two frequencies are necessary to perform both Zeeman pumping (m_F-states) and hyperfine pumping (correct hyperfine level F = 1). The repump light is only on for the first half of the pulse. An offset field is provided by dedicated coils that are wound around the z-MOT-compensation coils (table 3.8). The current for the offset field is produced by a capacitor discharge unit; if needed the polarity of the coils can be switched using a current-H-bridge. All relevant parameters can be found in table 3.9; they were found by maximising the number of captured atoms in the magnetic trap.

In order to estimate our pumping efficiency we vary the polarisation using a $\lambda/4$-waveplate (Fig. 3.17). The maximum and minimum numbers of captured atoms in Fig. 3.17 can be interpreted as most atoms being in $|F = 1, m_F = -1\rangle$ and $|F = 1, m_F = 1\rangle$ (un-trapped), respectively. Since these data points are roughly symmetric around the situation without any optical pumping ('no s-p') we can conclude that our Zeeman- and hyperfine-pumping are both in principle working properly. The deviation from the expected cosine-behaviour leads us to believe that our pumping efficiency is limited by birefringent optical elements between the waveplate and the position of the atoms (possibly the vacuum windows). This birefringence may prohibit perfect σ^+ and σ^- polarisation and therefore lead to a reduced optical pumping efficiency of roughly 75 %. In principle, the birefringence could be

accounted for by placing a $\lambda/2$-waveplate but this was not found to be crucial for BEC production.

There is no general consensus as to which hyperfine state should be used for transport. Some experiments [120, 160] opt for the $|F = 2, m_F = 2\rangle$ state because its trapping gradient is twice as large compared to states with $|m_F| = 1$. Other experiments [135] report the $|F = 1, m_F = -1\rangle$ to be beneficial. We use the latter state since it gives the best results (condensate numbers). This could be explained by the improved performance of the MW evaporation (section 3.11) using the lower ($F = 1$) hyperfine manifold. For ^{39}K we have so far not managed to effectively pump atoms into the $|F = 1, m_F = -1\rangle$ state[11] and consequently we do not perform any optical pumping for this species. Potentially the relatively strong offset field of 10 G precludes any efficient Zeeman pumping since at this field the upper hyperfine levels (Fig. 3.6 D) are split in a nonlinear way. Moreover, the final MOT stage for ^{39}K leads to a large occupation of the $F = 1$ manifold which in our case suffices to perform further cooling without any optical pumping.

[11] however, pumping to the $|F = 2, m_F = 2\rangle$ state works efficiently

3.10 *Magnetic trapping, transport, and experiment coils*

Magnetic quadrupole traps [127, 166] are used to capture the atoms in the MOT chamber, transport them to the science cell, and perform MW evaporation (section 3.11). Conceptually the magnetic trap relies on a magnetic field minimum at which atoms with positive Zeeman shift accumulate ($g_F \times m_F$ has to be positive in Eq. 3.1). The typical quadrupole coil configuration consists of two axially aligned coils with counter-propagating currents; this situation leads to a field minimum in between the two coils that is at exactly zero field with linear gradients in all directions. The main parameter characterising a magnetic trap, which for all practical purposes has infinite trap depth, is its gradient. Due to the second Maxwell equation $\nabla \cdot \mathbf{B} = 0$ the field gradient in the axial direction is twice as big as the gradients in the planar direction, leading to a 2:1-aspect ratio of the trapped atomic cloud. In this work the trap gradient is always quoted along the 'strong axis'.

A series of overlapping magnetic traps (Fig. 3.18) can be used to transport atoms over relatively large distances (64 cm in our case) in a 'conveyor belt' motion. By choosing appropriate current ramps in the successive coil pairs the aspect ratio[12] can be kept within reasonable bounds in order to avoid heating due to repeated compression and decompression of the cloud [117]. In our configuration (Fig. 3.19) this aspect ratio varies from 1.0 (when the cloud is at rest) to 2.4 (at the last coil pair before the atoms reach the experiment coils). More information on the design of the coil system can be found in the Master's thesis of Oliver Brix [167].

Table 3.10: Parameters used for magnetic trapping and transport.

parameter	value
total distance	64.35 cm
total duration	4.99 s
acceleration	0.2 m/s²
max. speed	0.5 m/s
sampling rate	1 kHz
MOT gradient @ 1 A	1.78 G/cm
MOT grad. (capture)	53 G/cm
MOT grad. (transport)	100 G/cm
exp. gradient @ 1 A	3.5(1) G/cm
exp. grad. (transport)	100 G/cm
exp. grad. (compressed)	300 G/cm

[12] between the longitudinal gradient along the transport axis and the transverse gradient

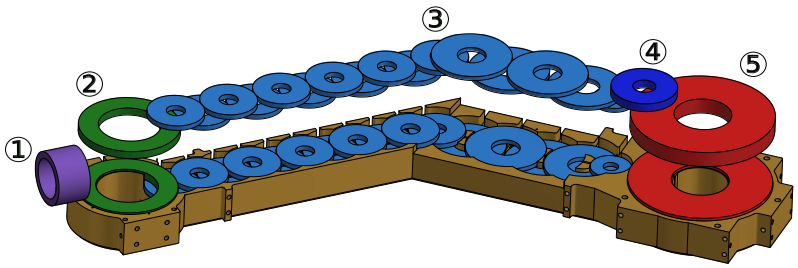

Figure 3.18: Schematic of magnetic coils used for MOT & magnetic capture (2, green), transport (3/4, blue), MW evaporation and Feshbach fields (5, red). All coils except the experiment coils (5) and the push coil (1) are glued into a brass cooling block (only the lower cooling block is shown for clarity). Figure taken from [124].

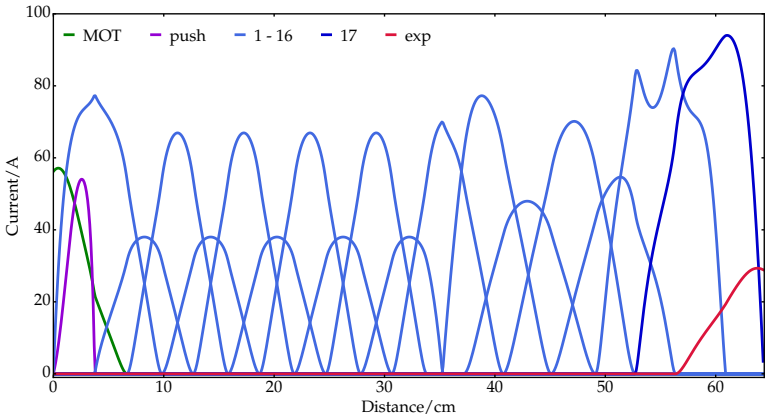

Figure 3.19: Coil currents used for magnetic transport. These were determined by maintaining an approximately constant aspect ratio of the atomic cloud over the travelled distance [117, 167]. The colour code is the same as in Fig. 3.18.

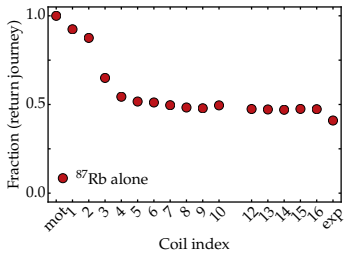

Figure 3.20: Fraction of rubidium atoms recaptured after transport (return journey).

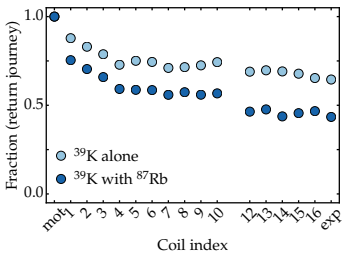

Figure 3.21: Fraction of potassium atoms recaptured after transport (return journey), with and without rubidium present.

The experiment coils themselves serve a further purpose, in addition to providing a strong magnetic confinement for transport and MW evaporation, namely to create homogeneous Feshbach fields (section 4.6). They are designed such that if the polarity of one experiment coil is flipped the resulting field at the position of the atoms is as homogeneous as possible. In our case we expect residual curvatures on the order to $10^{-4}\,\mathrm{mG/\mu m^2}$ at field strengths of several hundred gauss [167]. If we had a uniform optical trap for the atoms [168] these residual curvatures would result in effective trap frequencies on the order of 1 Hz.

The sequence for magnetic transport starts with trapping the atoms after optical pumping in the MOT chamber using a gradient of 53 G/cm. Subsequently the MOT field gradient is ramped to 100 G/cm and the atoms are transported using the current values shown in Fig. 3.19. In order to convert the distances to timestamps in sequence we use a constant acceleration until we reach a certain max. speed (and vice versa for decelerating). The atoms come to a halt at the 45° bend in the transport path ('knee' in Fig. 2.1). All relevant transport parameters are summarised in table 3.10.

The transport efficiency is characterised by performing a return-journey to the experiment coils and back. Afterwards the number of atoms that survived is counted (using fluorescence imaging in the MOT chamber), as shown in Figs. 3.20 and 3.21. The result-

ing transport efficiency is then given by the square root of the fraction of atoms remaining after the return journey (table 3.11). In general, the transport efficiency improves with higher gradients but we are limited to 100 A by our power supplies. Another way to enhance efficiency would be to transport the atoms in the $|F = 2, m_F = 2\rangle$ state which experiences a trap gradient that is twice as large. However, the subsequent MW evaporation stage works better in the $|F = 1, m_F = -1\rangle$ state and therefore we transport the atoms in this state. We observe that magnetic transport is generally more efficient for ^{39}K than for ^{87}Rb (Fig. 3.21). We also observe that lower acceleration improves the efficiency for ^{87}Rb.

Table 3.11: Single-journey transport efficiencies for rubidium and potassium.

^{87}Rb alone	64%
^{39}K alone	80%
^{39}K with ^{87}Rb	66%

Technical implementation of transport and experiment coils

All transport coils – except the pair of experiment coils – are glued into a brass block (Fig. 3.18) that is watercooled and actively stabilised to 21.5°C (which is also the set temperature of the laser-table air conditioning). More information on the design of the cooling block can be found in ref. [167]. The experiment coils were wound in-house using copper ribbon wire, kapton insulation between the windings, and thermally conductive but electrically insulating epoxy glue. The side of each coil that faces the brass block was milled down slightly (using a fly-cutter) and lapped in order to ensure flatness and thereby improve thermal contact with the brass block.[13] Between the coil and the brass block there is an electrically insulating (but thermally conducting) sheet, as well as heat compound paste that is directly applied to the coil face. Carbon plates are screwed to the cooling block from both sides in order to fix the experiment coils in place. The tightness of the screws was carefully adjusted to optimise cooling performance (table 3.12).

Table 3.12: Experiment coil parameters. Note that the ribbon height has been reduced by taking off < 0.5 mm from one side. The temperatures quoted are steady-state values for a 50 % duty cycle at 100 A; these are reached after about 10 minutes while the cooling block is stabilised to 21.5°C. The temperature values are measured using Pt100 sensors that are directly glued to the coil using thermally conductive epoxy glue.

parameter	value
windings	75 per coil
ribbon height	16 mm
ribbon width	0.5 mm
resistance upper coil	66.2 mΩ
resistance lower coil	66.2 mΩ
temperature upper coil	45°C
temperature lower coil	40°C

[13] despite this procedure there was some residual unevenness, probably due to the coil not being fully rigid in itself

Unfortunately, there is a mechanical instability in the upper experiment coil that makes fast switching impossible. If the upper coil is switched off suddenly using a MOSFET switch the effective field strength of the coil is reduced; consequently the position of the magnetic trap moves upwards. Repeated pulses of this kind lead to a degrading of field strength over time that takes several weeks to relax. We observed shifts of several hundred µm, corresponding to 1-2 A of current 'missing' in the upper coil. We attribute the effectively reduced current to electrical shorts between the windings. These could be potentially introduced by a jerk motion during the sudden switch-off of the coil (rough estimates suggest an outwards force on the order to 10 N within one coil caused by the magnetic field of the other coil). The field strength of the lower coil is insensitive to a sudden switch-off. We have avoided fast switching for several months now and the cloud position has been relatively stable since then.

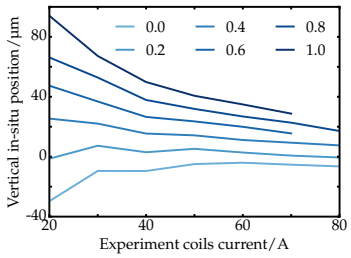

Figure 3.22: Optimisation of compensation coil fields using the movement of the quadrupole trap centre as figure of merit. Data is shown for six different current values in amps (colour-coded in different shades of blue) of the Z-compensation coils, the optimum being around 0.2 A (least movement).

Compensation coils (offset fields)

Similar to the MOT chamber we use three pairs of rectangular compensation coils around the science cell to counteract any stray magnetic fields. In an ideal quadrupole configuration the location of the field minimum does not change with the trap gradient. However, adding an offset field leads to a dependence of the trap centre on its gradient. Consequently we can use the trap movement to characterise our ambient magnetic fields and compensate for them by minimising the gradient-dependence of the trap centre (Fig. 3.22).

After describing transport and the necessary magnetic hardware we will now outline the evaporative cooling sequence in the steep magnetic trap.

3.11 *Microwave (MW) evaporation*

The first stage of evaporative cooling in our experiment takes the atoms from hundreds of µK down to the single-digit µK regime, cold enough to be trapped by the optical dipole trap (Chapter 4). In this technique the highest-lying atoms in the magnetic trap (i.e. the hottest ones) are selectively removed via radio frequency transitions to untrapped states. Evaporative cooling in magnetic traps was first proposed for hydrogen [169] and then demonstrated in 1995 [170, 171] in the wake of the first Bose-Einstein condensates. It remains an important technique to this day due to its conceptual simplicity, particularly in the context of atom-chip microtraps [172]. Future large-scale cold-atom experiments will probably move towards all-optical production of ultracold gases, e.g. loading the dipole trap directly from grey molasses [133], thereby avoiding the technical challenges posed by high-current carrying coils (see above). However, in our setup the possibility of selectively removing ^{87}Rb-atoms (and not the ^{39}K-atoms) is crucial to our sympathetic cooling strategy.[14]

[14] For more information on sympathetic cooling, please see section 4.3

For evaporation the $|F = 1, m_F = -1\rangle \rightarrow |F = 2, m_F = -2\rangle$ transition in the ground $5^2S_{1/2}$-level of ^{87}Rb (arrow in Fig. 3.5A) is addressed. After transport the ^{87}Rb atoms have a temperature of roughly 500 µK in the steep magnetic trap (300 G/cm). The initial frequency for MW evaporation is chosen such that only the very hottest atoms in the trap are removed at first. In our case we start at a frequency of 6676 MHz which addresses atoms situated at a magnetic field around 76 G (Fig. 3.5 A); this magnetic field corresponds to a thermal energy ($k_B T$) of 5 mK. In an ideal thermal gas at 500 µK only a tiny fraction (5×10^{-5}) of atoms have more kinetic energy than this, which justifies our starting frequency. Subsequently the MW frequency is lowered to 6827.2 MHz in a 7.5 s ramp.

Technical implementation

The MW radiation for evaporation is generated by mixing the output of a home-built DDS unit [173] with a reference oscillator at 6500.0 MHz. The signal is then amplified several times (10 W max. power) and brought to the atoms by a waveguide and a capped horn antenna which is situated around 13 cm from the atoms in direct line of sight. The backreflection from the antenna is dumped via a circulator into a high-power attenuator.

Majorana losses

The 'kink' at the centre of a magnetic quadrupole trap starts to dominate the (quasi-)equilibrium[15] in the trap for temperatures in the μK regime. In this region, atoms passing very close to the magnetic field minimum experience a sudden change in direction of the magnetic field, leading to a non-adiabatic spin-flip [125]. In our case this means that trapped atoms in the $|F = 1, m_F = -1\rangle$ state become un-trapped ($|F = 1, m_F = 1\rangle$) and lost from the cloud. Even worse, since the atoms in the centre of the trap are the coldest ones, these atom losses lead to heating due to rethermalisation of the remaining atoms. Therefore we terminate MW evaporation at temperatures around 6.6 μK before Majorana losses (Fig. 3.23) and heating (Fig. 3.24) become dominant.

Before we turn to the dipole trap and the physics of Bose-Einstein condensation in Chapter 4 the experimental aspects of absorption imaging are briefly discussed in the following. The time-of-flight imaging technique is covered in more detail in section 6.2 in the context of optical lattices.

[15] Perfect equilibrium for a thermal gas in our system can never be reached since particle number is not conserved. There is always an (exponentially small) fraction of atoms at very high energies that can escape the trap. Subsequent re-equilibration leads to an additional evaporation effect which is negligible for our experimental timescales.

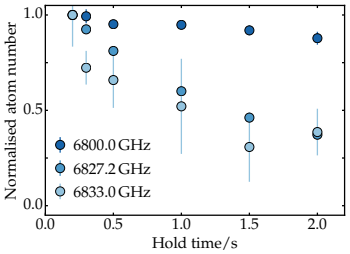

Figure 3.23: Majorana losses for ^{87}Rb (no ^{39}K present) for three different final MW frequencies. The hold time in a steep magnetic trap (300 G/cm) after termination of the MW evaporation is plotted on the x-axis. Temperatures and atom numbers are measured after release from the dipole trap in 33 ms ToF.

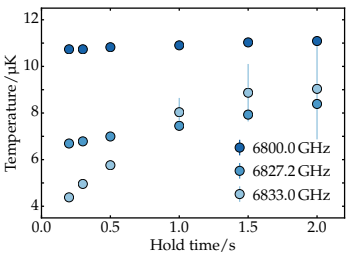

Figure 3.24: Majorana heating for ^{87}Rb in the steep magnetic trap for three different final MW frequencies.

3.12 *Absorption imaging*

The absorptive behaviour of a material in the presence light, characterised by the Beer-Lambert law, has been known for more than a century. In the case of an atomic vapour and laser light that is resonant with a closed transition in the atom the laser intensity is simply reduced exponentially with the distance travelled through the vapour. Thus we can extract the density profile of an atomic cloud by taking a sequence of two images of the laser beam profile, one with the atomic cloud (seen as a shadow) and one without [125]. The optical density of the cloud is then given by

$$OD(x,y) = \sigma\, n_{\text{column}}(x,y) = -\ln\left(\frac{I(x,y)}{I_0(x,y)}\right) \tag{3.4}$$

Here σ is the absorption cross-section of a single atom, n_{column} is the column density, $I(x,y)$ is the 'atom' picture, and $I_0(x,y)$ is the empty picture.[16]

All the measurements on Bose-Einstein condensates (with and without lattices) were performed using this technique. Usually we release the atoms from the dipole trap (see chapter 4 below) and

[16] in practice a third image is taken without any laser light (background image) an this image is subtracted from both $I(x,y)$ and $I_0(x,y)$

perform absorption imaging in 33 ms time-of-flight (ToF) on the Z-axis (along gravity). There is resonant imaging and repump light available for both species on all individual lattice axes (named X, Y, D, and T, according to Fig. 5.17 in Chapter 5).

In some special cases it can be useful to image the cloud 'in-situ', i.e. in the trap, for example to measure the position of the magnetic trap (Fig. 3.22). Note that our capabilities of taking images in ToF from the magnetic trap are limited since we cannot shut down the coil currents quickly enough (section 3.10). Short imaging pulses of 100μs with low intensity[17] ($I \ll I_{sat}$) are typically used.

[17] such that σ is only weakly dependant on I

At low magnetic fields, both ^{87}Rb and ^{39}K are imaged on their respective $^2S_{1/2}\ |F = 2, m_F = 2\rangle \rightarrow {}^2P_{3/2}\ |F = 3, m_F = 3\rangle$ transition which comes closest to being a cycling transition. It is crucial for the imaging light to have a definite polarisation with respect to the quantisation axis of the atoms, given by a homogeneous magnetic field. In particular, the low-field imaging scheme requires σ^+ polarised light. A wrong polarisation can lead to an effective shift in the imaging transition. Figure 3.10 nicely illustrates this effect to the extent that σ^- polarised light causes a shift by several MHz. These imaging resonance scans were taken using a cold atomic cloud released from the dipole trap.

Repump flash

In order to use the $|F = 2, m_F = 2\rangle \rightarrow |F = 3, m_F = 3\rangle$ cycling transition the atoms have to be prepared in the $^2S_{1/2}\ |F = 2, m_F = 2\rangle$ state, or at least the $F = 2$ level within $^2S_{1/2}$, prior to imaging. To this end, a dedicated flash of repump light (see Figs. 3.1 and 3.3) may be necessary, depending on the current stage of the experimental sequence. Low-field imaging in ^{39}K is almost never used due to the slowness of our experiment coils (section 3.10), nevertheless, ^{39}K repump light is available on two imaging axes in the science cell. In the case of ^{87}Rb, the repump flash is almost always used.[18] Figure 3.8 shows a resonance scan of the repump flash frequency (which can be tuned using an AOM in double-pass configuration) using a cold atomic cloud. In order to maximise the detected atom number, a relatively long flash of 1.0 ms is used in the experiment.

[18] since the ^{87}Rb atoms spend almost all their lives in the ground $F = 1$ manifold

Table 3.13: High-field imaging resonances for ^{39}K.

B-field/G	Resonance/MHz
317.38	-301.4
351.44	-352.4
397.19	-419.0

High-field imaging in ^{39}K

In contrast to ^{87}Rb, the potassium atoms are almost exclusively imaged at strong magnetic fields (see section 4.6 below). The atomic levels in ^{39}K are detailed in Fig. 3.6 for both low and high magnetic fields. In this case, the $|F = 1, m_F = 1\rangle$ state connects to the $|m_I = 3/2, m_J = -1/2\rangle$ at high magnetic fields. Imaging is performed on a transition from this state to the $|m_I = 3/2, m_J = -3/2\rangle$ state in $^2P_{3/2}$. Unfortunately, the mixing of hyperfine states at high fields precludes the existence of a cycling transition and leads a depumping effect [174] of approximately 3% per cycle. The neg-

ative effects of depumping can be mitigated by performing an independent measurement of atom number by means of locating the BEC transition (section 4.7).

High-field imaging of ^{39}K is routinely performed in our experiment and some measured resonance frequencies are shown in table 3.13. The experimental resonances agree excellently with the theoretical prediction from Fig. 3.6, including the electric quadrupole correction [140]. As with low-field imaging, the polarisation of the imaging light is crucial here. To this end, a setup containing a $\lambda/2$ and a $\lambda/4$ waveplate is used to optimise the imaging polarisation using atom number as figure of merit.

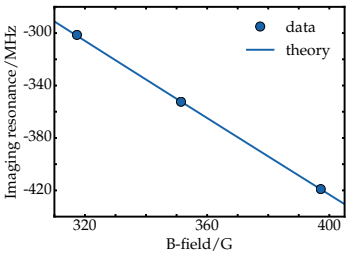

Figure 3.25: ^{39}Kimaging resonances at strong magnetic fields. The agreement between the experimental values (table 3.13) and the theoretical prediction (Fig. 3.6) is better than 0.6 MHz.

Stern-Gerlach imaging

In order to discern the population of m_F states of a given atomic cloud, the Stern-Gerlach imaging technique is used. The cloud is split according to the magnetic moment of each atom by subjecting the atoms to a magnetic field gradient while they are in free fall (during time-of-flight).

In our apparatus a dedicated gradient coil has been wound in a 3D-printed mount that also contains the RF-antenna (section 4.5), just above the science cell. It is driven by a home-built capacitor discharge unit that is designed to provide a short pulse of high current (table 3.14).

This coil provides a vertical field gradient of $> 10\,\mathrm{G/cm}$ such that the cloud is split vertically into the different m_F components. For ^{87}Rb, a 2 ms current pulse at the beginning of ToF (15 ms) leads to a vertical displacement of 246 µm between each m_F component.

Table 3.14: Parameters for Stern-Gerlach imaging.

parameter	value
coil windinds	360
peak current	12 A
initial rise time	50 µs
pulse duration ^{87}Rb	3 ms
pulse duration ^{39}K	1 ms

It should be noted that neither the repump flash, nor the Stern-Gerlach imaging technique has been achieved after the magnetic trap but only in the dipole trap.

This discussion of absorption imaging, including specific applications thereof, such as high-field imaging in ^{39}K and Stern-Gerlach imaging, concludes the chapter on experimental methods for laser cooling.

4
Quantum gases

Up to this point in the experimental sequence (table 2.1) the atoms have been cooled, trapped, transported to the science cell, and cooled down further to µK temperatures. During these stages of the sequence the atom cloud represents a classical, thermal gas. However, at even lower temperatures the collective properties of the gas start to be influenced by the wave-like nature of particles, i.e. quantum mechanics. The first important manifestation of collective quantum-mechanical behaviour lies in the collisional properties at low momenta. This will be briefly discussed in the context of Feshbach resonances (section 4.6).[1] Once the thermal wavelength of the particles becomes comparable to the inter-particle distance, the gas has to be described fully quantum-statistically, reflecting the strikingly different low-temperature phases of fermions and bosons (section 4.7).

[1] Note that the bosonic or fermionic particle symmetry already influences thermodynamic properties, namely via the type of prevalent low-energy collision, long before quantum-statistical considerations become relevant.

The chapter begins with a brief introduction to optical dipole traps. Afterwards our specific setup, namely a crossed-beam dipole trap with elliptical waists, is characterised theoretically and experimentally. Sympathetic cooling is discussed, together with the general properties of Feshbach resonances in ^{39}K. Finally the concept of Bose-Einstein condensation is introduced.

4.1 Dipole trap: introduction

The interaction between atoms and monochromatic light can be broadly divided into two separate regimes. On the one hand, near-resonant light leads to dissipative behaviour and, consequently, photon scattering. This effect is utilised by laser cooling methods such as the molasses technique (section 3.8). On the other hand, far-detuned light acts dispersively, leading to a conservative potential for neutral atoms which is often referred to as the dipole potential. Relevant formulae can be derived both semi-classically [127, 175] and purely quantum-mechanically [165, 175, 176]. The latter derivation is based on the Jaynes-Cummings model, describing a two-level atom coupled to a quantised light-field (a coherent state) resulting in a shift of the two atomic levels, called light-shift or AC-Stark shift. Semi-classically, the light-shift can be understood as the average energy of a dipole in the presence of an oscillating electric field, characterised by the real part

of the polarisability of the atom. In this chapter we will not derive the formulae from first principles but instead refer to Grimm et al. [175]. In our experiment we use a standard red-detuned dipole trap at 1064 nm such that an intensity maximum results in a trough in the potential. The photon scattering rates in the trap centre are on the order of millihertz and can thus be neglected on experimental timescales.

Choice of trapping geometry

Both the loading of the dipole trap and the subsequent evaporation to quantum degeneracy contain several non-linearities, such that the choice of optimal dipole beam parameters a subtle trade-off between many different variables.

Several factors affect the loading efficiency of the dipole trap from a magnetic quadrupole trap. Firstly, a high spatial overlap between the two traps is required. The aspect ratio of an atomic cloud confined to the centre of a radially symmetric magnetic quadrupole field is always approximately $2:1$ (as discussed in section 3.10). This favours radially symmetric, oblate dipole traps of similar aspect ratio. Secondly, the trapping volume should be large, encouraging large beam waists, so as to transfer as many atoms as possible to the dipole trap. But for the same reason the trap should also be as deep as possible which, given a fixed available laser power, favours small waists.

The dipole trap geometry also crucially affects the final stages of the experimental sequence, including optical evaporation and loading into the optical lattice. Optical lattice experiments in two dimensions profit from approximately homogeneous density profiles, favouring oblate traps with high aspect ratios. In addition, anticonfining effects of blue-detuned lattice potentials can be cancelled[2] by suitably configured dipole traps. Moreover, the geometric mean of the trapping frequencies $\bar{\omega} = \sqrt[3]{\omega_z \omega_r^2}$ should be kept as large as possible in order to avoid very high densities at the centre of the trap which can lead to three-body losses. Finally, the efficiency of sympathetic cooling using a coolant with a larger atomic mass (e.g. cooling ^{39}K with ^{87}Rb) depends in a subtle way on the gravitational sag in the dipole trap (as discussed in the following). On the one hand, maximising the spatial overlap between the two species corresponds to having a small differential sag and very small vertical waists. On the other hand, ideal sympathetic cooling of ^{39}K keeps all the potassium atoms in the trap, evaporating only ^{87}Rb atoms. It turns out that the parameter region of optical powers for which this is the case is larger for *smaller* vertical waists.

In our experiment we decided to use a crossed-beam dipole trap with elliptical beam profiles, summarised in table 4.1. The two dipole beams propagate in the plane normal to gravity and their foci intersect at an angle of just under 90°. For each beam the ratio of horizontal to vertical waist size is about five to one,

[2] In the case of a one-dimensional, blue-detuned, simple-cubic lattice the resulting anticonfining potential is gaussian in both horizontal and vertical directions which can be compensated exactly by an attractive dipole potential with a $\sqrt{2}$ times larger waist. For two-dimensional lattices the cancellation is approximate. Here, instead of an in-plane crossed-beam trap a single dipole beam in the axial direction can be used to cancel the quadratic terms in the anticonfining potential.

Table 4.1: Dipole trap beam parameters at the position of the atoms, as determined by measuring trap frequencies.

axis	w_{0h}/μm	w_{0v}/μm	max. pow.
x	285(5)	55(2)	>7 W
y	285(5)	55(2)	>7 W

leading to a radially symmetric, oblate trapping geometry.

Trapping potential

The dipole potential for an idealised two-level (e-g) atom state can be written as [175]

$$V_{\text{e-g}}(\mathbf{r}) = -\frac{3\pi c^2}{2\omega_a^3}\left(\frac{\Gamma_a}{\omega_a - \omega_f} + \frac{\Gamma_a}{\omega_a + \omega_f}\right) I(\mathbf{r}) \quad , \tag{4.1}$$

where ω_a is the resonance frequency of the atom, ω_f the frequency of the light field, Γ_a the spontaneous scattering rate, and $I(\mathbf{r})$ the laser intensity profile. In a red-detuned dipole trap we have $\omega_a > \omega_f$ such that the dipole potential $V_{\text{e-g}}$ is negative, leading to an attractive force towards its centre. The relevant transitions in the alkalis are the D-lines (section 3.1) which both contribute to the total trapping potential, given by

$$V_{\text{dip}}(\mathbf{r}) = \frac{1}{3}V_{\text{e-g}}^{\text{D1}}(\mathbf{r}) + \frac{2}{3}V_{\text{e-g}}^{\text{D2}}(\mathbf{r}) \quad . \tag{4.2}$$

Here we have assumed linearly polarised light for which the trapping potential is independent of the given internal hyperfine state of the atom.

The intensity profile of a focussed gaussian laser beam, assumed to propagate along the z-axis is

$$I(\mathbf{r}) = \frac{2P}{\pi w_h(z) w_v(z)} \exp\left(-\frac{2h^2}{w_h^2(z)} - \frac{2v^2}{w_v^2(z)}\right) \quad . \tag{4.3}$$

The paramaters h and v stand for the respective horizontal and vertical coordinate and P is the optical power in watts. The beam waists $w_i(z)$ are given by

$$w_i(z) = w_{0i}\sqrt{1 + \left(\frac{z}{\pi w_{0i}^2/\lambda}\right)^2} \quad , \quad i \in \{h, v\} \tag{4.4}$$

where w_{0i} are the (single) waists of the elliptical gaussian beam in h, v-direction and λ is the dipole trap wavelength.

Now we are going to change into lab coodinates. In the crossed-beam configuration two dipole foci of equal waists are overlapped at just under 90° which can be approximated by the sum of two gaussian beams propagating along x and y, respectively. In the lab frame z is chosen to be the direction of gravity and thus the axial direction of the crossed-beam trap. Both beams are supposed to have equal waists such that the trap is radially symmetric in the xy-plane. The dominant trapping effect arises from the respective transverse beam profile of each beam, whereas the beam profile along the axes of propagation only add a weak confinement.

In the centre of the trap the potential is harmonic which can be seen by Taylor-expanding Eq. 4.3. The characteristic trapping

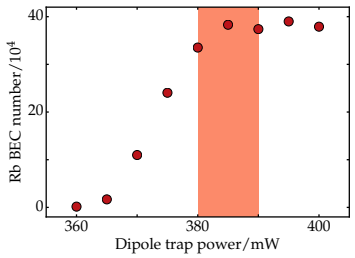

Figure 4.1: Minimal trapping power for ^{87}Rb in the dipole trap. Below a certain threshold (385(5) mW in each beam, marked by the shaded area) the dipole trap cannot hold the rubidium condensate against gravity.

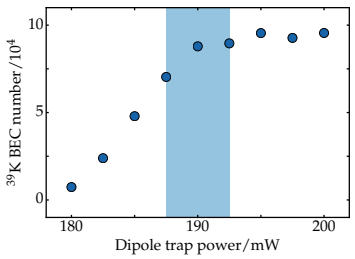

Figure 4.2: Same as above, but for ^{39}K. Here the threshold is 190(2) mW.

frequencies in the radial (ω_r) and axial (ω_z) directions for an atom of mass m are then given by

$$\omega_r = \sqrt{\frac{4V_0}{mw_{0h}^2}} \tag{4.5}$$

$$\omega_z = \sqrt{\frac{8V_0}{mw_{0v}^2}} \quad , \tag{4.6}$$

where V_0 is the maximum dipole potential, i.e. V_{dip} in the centre of the trap. Both dipole beams contribute to the vertical confinement which leads to an increase in the vertical trapping frequency by a factor of $\sqrt{2}$ compared to a single-beam trap.

Effects of gravity

The expressions 4.5 and 4.6 are good approximations as long as gravity can be neglected. But as soon as the gravitational potential becomes comparable to V_{dip} it has to tbe included, leading to a total potential of the form

$$V_{\mathrm{tot}}(\mathbf{r}) = V_{\mathrm{dip}}(\mathbf{r}) + mgz \quad . \tag{4.7}$$

The maximum trap depth $V_{\mathrm{max}}/k_{\mathrm{B}}$ expressed in µK is given by the energy difference between the local minimum and the closest local maximum of Eq. 4.7 which can be determined numerically. In particular, the maximum trap depth vanishes at non-zero dipole trap power, called 'minimal trapping power', causing the atoms to spill out of the trap centre. The minimal trapping power is quantified experimentally in Figs. 4.1 and 4.2 by measuring the condensate atom number for various dipole powers. Whereas for low dipole trap powers the vertical trap depth is limiting, the high-power maximum trap depth is limited in the horizontal direction (V_{horz}, dashed lines in Fig. 4.3A). Therefore the functional form of V_{max} (Fig. 4.3A) exhibits a kink for each atomic species, indicating the cross-over between the vertically and horizontally limited regimes. This cross-over occurs at roughly 0.6 W for ^{39}K and 1.2 W for ^{87}Rb. In our beam configuration the maximum trap depth for

Table 4.2: Measured dipole trap frequencies for ^{87}Rb. The frequencies were experimentally determined by slowly lifting a ^{87}Rb-condensate by means of increasing the dipole power and then suddenly decreasing the power to the precise values listed in the table. This jerk in the position of the dipole trap leads to oscillations (along all axes, though primarily along z) which are fitted to a cosine in order to extract the frequency.

power	0.38 W	0.40 W	0.45 W	0.50 W	0.55 W	0.70 W	1.00 W
$\omega_r/(2\pi)(x)$	14.2(2)	15.9(2)	17.6(6)	19.2(5)		23.8(5)	28.4(5)
$\omega_r/(2\pi)(y)$	12.2(9)	13.7(9)	14.7(5)	16.6(9)		20.6(6)	23.9(9)
$\omega_z/(2\pi)$			90.8(3)	108.6(5)	120.9(8)	150.7(8)	183.1(7)

Table 4.3: Measured dipole trap frequencies for ^{39}K. The measurement protocol is identical to table 4.2 above.

power	0.20 W	0.25 W	0.30 W	0.50 W	1.00 W
$\omega_r/(2\pi)(x)$	16.5(5)	19.1(5)	21.9(5)	29.06(2)	41.1(5)
$\omega_r/(2\pi)(y)$	14.9(5)	17.5(5)	19.4(5)	25.49(2)	35.7(5)
$\omega_z/(2\pi)$	74(1)	115.3(5)	135.9(5)	190(1)	280(5)

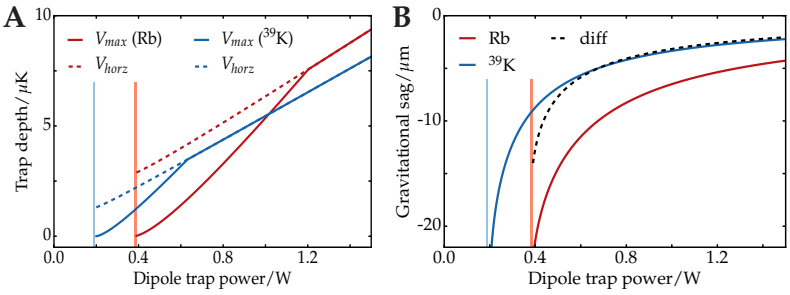

Figure 4.3: (**A**) Maximum trap depth ($V_{\max}/k_B$) versus dipole trap power (in each beam). For low powers the vertical trap depth is limiting (the atoms leave the trap from the centre along gravity) whereas for higher powers (above 1.2 W) the horizontal depth is limiting (the atoms leave the trap to the side). (**B**) Calculated gravitational sag for ^{87}Rb (red), ^{39}K (blue), and the difference between the two ('differential sag', black dashed). The pale blue (red) vertical bars are the measured minimal trapping powers from Fig. 4.1 (4.2) which agree well with the numerical results.

^{87}Rb drops below that of ^{39}K at about 1.0 W. Fig. 4.3A also shows the experimental values of minimal trapping power (vertical bars of the same colour as in Figs. 4.1 and 4.2) which agree well with the theoretical prediction.

Gravity does not only affect the trap depth but also the vertical position of the trap centre. This effect, also known as gravitational sag,[3] is summarised in Fig. 4.3B.

4.2 *Trap frequencies*

The extent of a cloud of ultracold atoms in a dipole trap is typically much smaller than the beam waists and the expansion of the potential around the trap centre can be restricted to include terms up to quadratic order. For all practical purposes the dipole potential is therefore fully characterised by its vertical and horizontal trap frequencies ω_z and $\omega_r = \omega_x = \omega_y$, respectively. These can be obtained numerically from fitting a parabola to the local minimum of Eq. 4.7 (at the vertical position z given by the gravitational sag, Fig. 4.3B). We find excellent agreement between our measurements (values in tables 4.2 and 4.3) and the numerical predictions, shown in Fig. 4.4. Note that the horizontal trap frequencies are measured on the x/y-axes of the z-axis imaging camera and do not necessarily correspond to ω_x and ω_y (the principal axes of the dipole trap). The mismatch between the two measured horizontal frequencies could be either explained by the not-perfectly-90° angle between the two dipole axes[4] or by slightly different horizontal beam waists (the latter seems more likely).

Sympathetic cooling works best if the coolant (^{87}Rb) is predominantly evaporated, such that most of the potassium atoms remain in the trap. It has been argued by Campbell et al. [131] that sympathetic cooling in deep dipole traps does not work well. However, we find decent cooling results with this method despite the limiting ^{39}K trap depth. This could be explained by a different evaporation ramp, higher available ^{87}Rb atom numers, or by the different trap geometry

[3] Efficient sympathetic cooling relies on a good spatial overlap between the two species.

[4] which should show up as beating in the oscillation signal between the x- and y-axes but was not resolved in our experiments

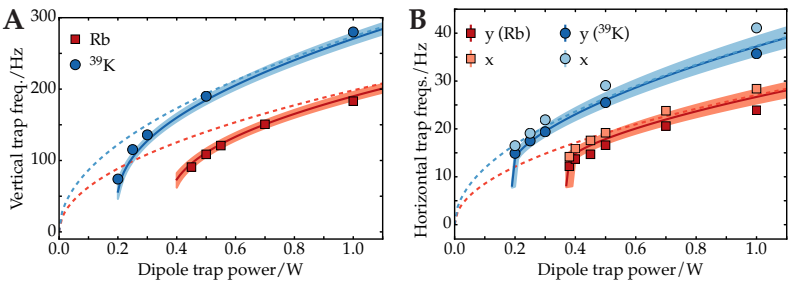

Figure 4.4: Vertical (axial, **A**) and horizontal (radial, **B**) trap frequencies $\omega/(2\pi)$ versus dipole trap power (per beam). The solid lines and shaded regions show the numerical prediction with a 2.5 μm uncertainty of the vertical beam waist. The dashed lines represent Eqs. 4.5 and 4.6 (neglecting gravity).

Table 4.4: Evaporation parameters used to reach quantum degeneracy

parameter	^{87}Rb	^{39}K
initial power	7 W	
initial V_0/k_B	43 µK	38 µK
final power/mW	∼400	∼200
final V_0/k_B	3 µK	1 µK
exp. ramp dur.	3 s	
exp. time const.	0.5 s	
guide field	2.8(1) G	
1st Fesh. (1.7 s)	0 G	315.49(2) G
	100 a_0	141(1) a_0 (inter)
2nd Fesh. (1.3 s)	0 G	397.8(1) G
	100 a_0	280 a_0 (intra)

4.3 *Evaporation and sympathetic cooling*

Quantum degeneracy of ^{87}Rb or ^{39}K is achieved by forced evaporation [177] in the dipole trap. In the case of ^{39}K we start evaporation at similar temperatures but with far fewer atoms compared to ^{87}Rb, necessitating a more efficient cooling method. We employ the widely used sympathetic cooling technique [131, 178, 179] which utilises the abundant ^{87}Rb atoms as coolant for ^{39}K. The experimental parameters used for evaporation are summarised in table 4.4. They are optimised to maximise condensate atom number, given a fixed ramp duration of 3 s.

4.4 *Dipole trap laser setup*

This section is an interlude about the setup and characterisation of the dipole trap.

All dipole beams are derived from a single-frequency solid state laser[5] at 1064 nm. The two (x and y) dipole trapping beams are prepared on a separate laser table[6] from which the laser power is distributed via optical fibres to the experiment. The z-dipole axis has been prepared but not implemented yet; it is designed to provide additional radial confinement for the lattice potential once the atoms habe been loaded into the quasicyrstalline potential.

Each beam passes through an AOM in order to shift its frequency (with respect to the other beams, avoiding cross-interferences) and to stabilise its intensity via PID feedback. After the initial split, the x and y beams both carry 17 W of power from which max. 8 W is measured after passing through the science cell. The largest losses are caused by the AOM (15%), the DC fibre polarisation maintaining[7] (∼25%), and the glass-cell/air interfaces (measured ∼6% each, 45° incidence). More information on the preparatory stages of the dipole trap setup can be found in Max Melchner's Master's thesis [180].

After exiting the optical fibre on the experiment laser table each beam passes through a Glan-Laser prim in order to clean the polarisation. The transmission through two subsequent bending mirrors is used as PID input signal (45° bend) and monitoring signal (22.5° bend). At 1064 nm, Silicon-based photodiodes are *not* suitable for high-bandwidth applications, such as the PID loop, due to the slow diffusion time constant t_2 in this wavelength range [181]. Therefore we use high-bandwidth amplified InGaAs photodiodes for PID feedback. The feedback loop is otherwise identical to the lattice intensity stabilisation 5.4. The optical power of each dipole beam (for example, on the x-axis of Fig. 4.1) has been calibrated using a power meter *after* the beam passed through the science cell. Therefore the true optical power at the position of the atoms is approximately 10% higher than the specified value. Although, in principle, powers up to 8 W have been measured after the science cell, the maximum values used in the sequence are 7 W in order to leave some room for long-term drifts.

[5] Mephisto MOPA 55 W, Coherent Inc.

[6] 'high-power' or HP table, which also hosts the lattice laser

[7] The 'cold' fibre coupling efficiency (AOM on pulsed mode with 1% duty cycle) is about 95%. But in DC mode the coupling efficiency is reduced to ∼ 75%, probably due to polarisation drifts which manifest themselves as power drifts after the Glan-Laser cleaning prism.

Table 4.5: Horizontal (w_{0h}) and vertical (w_{0v}) dipole trap beam waists in µm. 'Design' refers to the values that were aimed at, 'theory' are the expected values using ABCD matrices, given the approximate distances on the breadboard and the measured divergence from the fibre coupler, 'exp(erimental)' are the measured values using a camera that is focussed to the position of the atoms, and 'freq(uency)' refers to inferred values by measuring trap frequencies (table 4.1).

	Dipole x		Dipole y	
waist	w_{0h}	w_{0v}	w_{0h}	w_{0v}
design	280	50	280	50
theory	284	53	279	52
exp	284	64	280	47
freq	285(5)	55(2)	285(5)	55(2)

After the Glan-Laser prism, the beam first passes through a cylindrical telescope and then a spherical telescope before it is focussed to the atomic cloud via an achromatic lens (125 mm focal length), as shown schematically in Fig. 5.17 in the following Chapter. The gaussian beam propagation has been modelled[8] for the actual physical setup on the experiment table, taking into account the measured beam divergence from the fibre collimation. For elliptical beams, the horizontal and vertical waists propagate independently from each other, making it (in general) impossible to focus both the vertical and the horizontal waist to the same point. The horizontal waist of the dipole beam at the position of the atoms is relatively large, corresponding to a small divergence, whereas the vertical waist is strongly divergent. Therefore, all remaining degrees of freedom[9] were optimised to create an essentially focussed beam at the atoms with specified design-waists. The experimentally measured waists agree reasonably well with the expected values from gaussian propagation (see table 4.5). Note that the theoretical values resulting from the trap frequency measurement assume a radially symmetric dipole trap. The experimental agreement could be improved by modelling the trap frequencies in x and in y separately, accounting for the measured mismatch between the two (Fig. 4.4B).

[8] using ABCD matrices

[9] distances between telescopes and lenses (given the physical constraints on the breadboard) and the available focal lengths of lenses

The final achromatic lens to focus each dipole beam to the atoms is shared with the lattice setup by employing the grazing-angle technique. The dipole beam is reflected off a D-shaped mirror and for a short distance (5 cm) it propagates parallel to the corresponding lattice beam. The lattice beam is incident on the final achromat on its optical axis; the dipole beam is incident roughly 5 mm away from the optical axis. Since both beams impinge on the lens as parallel rays they are focussed to the same spot. Consequently, the dipole beams are overlapped at the position of the atoms under different angles than the lattice, in our case just under 90°. Due to the relatively large horizontal waists, the trap geometry is insensitive to the exact angle under which the dipole beams are overlapped. This technique avoids the use of expensive dichroic mirrors while maintaining the necessary flexibility in the alignment of both lattice and dipole trap. A schematic of the optical setup around the science cell can be found in section 5.4 below.

Alignment

All degrees of freedom of alignment, except the relative horizontal angle between the dipole beams (as mentioned above), are important for the resulting dipole trapping performance.

Firstly, the focus of the (vertical) dipole waists should coincide with the atomic cloud, in order to ensure maximum trap depth. This is achieved by first focussing a camera on each dipole axis to the position of the atoms (using in-situ absorption imaging). Subsequently, the last achromat is moved longitudinally (on a

z-translation stage with µm screws) to focus the dipole beam.

Secondly, each dipole beam should propagate perpendicular to gravity, thereby minimising gravitational sag. We achieve this by beam walking using pinholes centred on the achromatic lenses, thereby trusting that our optical table is also aligned perpendicular to gravity. Using the time-of-flight technique on the D-axis[10] we measured the angle of the dipole trap beams with gravity to be $90.0(5)^\circ$.

[10] one of the lattice axes which does not have a dipole beam

Thirdly and most importantly, the dipole beams have to intersect at the same point in space ('pointing'). This is necessary in order to benefit from the crossed-beam configuration in which the vertical trap depth of both beams add up. If the beams do not intersect vertically, the trap depth is greatly reduced (in the worst case by a factor of two). In addition, the vertical intersection ensures the approximate radial symmetry of the trap (up to the discrepancies in beam waist).

To this end, the last kinematic mirror before the final achromat is piezo-driven. Rough pre-alignment is achieved by loading cold atoms into a single-beam dipole trap and maximising the in-situ optical density.[11] Fine alignment is achieved by producing a condensate and lowering the final evaporation depth until almost no atoms are held against gravity. Then the vertical alignment can be changed in small steps by the piezo-driven mirror to maximise atom number. This alignment technique can discriminate the optimum position of the mirror to within 10 piezo steps; this corresponds to a mirror-displacement of roughly 170 nm and a vertical displacement (at the atoms) of 1.6 µm.

[11] An optical density of 1.8-2.0 for ^{87}Rb is a good benchmark here.

The centre of the dipole trap is aligned 61 µm below centre of the magnetic trap for optimum loading efficiency.

Table 4.6: Magnetic field calibration of the guide field. For each current value we take an RF/MW-resonance scan using a Landau-Zener sweep of 20 ms duration. In the case of the RF transfer the transition $|F = 1, m_F = -1\rangle \rightarrow |F = 1, m_F = 0, 1\rangle$ in the ground level of ^{87}Rb is used, in the case of MW we use $|F = 2, m_F = 2\rangle \rightarrow |F = 1, m_F = 1\rangle$. These frequencies are then converted to magnetic field values using the magnetic field hamiltonian (section 3.2).

Current/A	RF/MW resonance	B-field/G
6.0	3.042(8) MHz	4.35(1)
6.0	6843.78(2) MHz	4.33(1)
4.5	1.95(5) MHz	2.8(1)

4.5 *Dipole loading, guide field, and RF state transfer*

Before the magnetic trap is ramped down and during loading of the dipole trap we apply a homogeneous magnetic field ('guide field') using offset coils in the z-direction (Fig. 4.5). This serves three purposes: Firstly, it ensures a definite quantisation axis after the magnetic trap has been switched off and before the (strong) Feshbach field comes on (in the case of ^{39}K).[12] Secondly, it compensates for long-term drifts in the position of the magnetic trap (section 3.10), ensuring good spatial overlap between the magnetic trap and the dipole trap. Our offset coils shift the vertical trap position a little more than 25 μm/A when applied to a high-gradient magnetic trap of 300 G/cm (strong axis). Thirdly, we perform a radio-frequency (RF) state transfer, using the guide field to lift the degeneracy of the internal states of ^{87}Rb and ^{39}K. The choice of internal states during evaporative and sympathetic cooling is of crucial importance to the success of these methods [182]. Inelastic collisions between atoms in different internal states can lead to heating and losses. Consequently it is desirable to transfer the atoms to their respective absolute ground state, thereby

[12] Though even without a quantisation axis during the entire dipole evaporation ramp we achieve condensation with ^{87}Rb.

precluding inelastic processes. In our case this is achieved simultaneously for ^{87}Rb and ^{39}K using a Landau-Zener transition from $|F = 1, m_F = -1\rangle$ to $|F = 1, m_F = 1\rangle$. The RF transfer is accomplished by a 20 ms-long linear frequency sweep from 1.90 MHz to 2.00 MHz at a homogeneous magnetic field of 2.8(1) G.

Figure 4.5 shows a scope trace of our dipole loading procedure, including a photodiode signal of the dipole trap, current clamp measurements of the experiment coil and the offset-z coil, and the timing of the RF transfer. The calibration of our guide field is summarised in table 4.6.

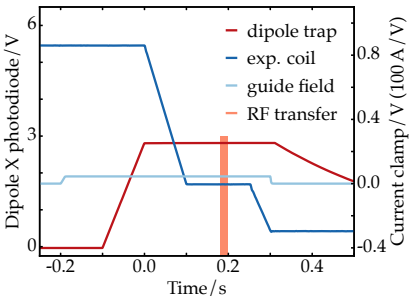

Figure 4.5: Dipole trap loading procedure (for ^{39}K). Before the magnetic quadrupole field (dark blue) is ramped down we apply a guide field (light blue), as discussed in the text. The polarity of the upper experiment coil (dark blue) is then changed to provide the inter-species Feshbach field during evaporation. In case of ^{87}Rb the dipole loading procedure is identical except that there is no Feshbach field.

RF antenna

The RF antenna that is used for the state transfer operates in the near-field regime ($\lambda_{RF} = 1.5$ m) and consequently the radiation consists mostly of an oscillating B-field. The antenna geometry and its number of windings is therefore largely insignificant (see Fig. 4.6). In addition, the antenna can be approximated by an isotropic emitter, making the coupling efficiency of the radiation independent of the precise alignment (angle) of the antenna with respect to the atoms, as long as it is placed as close as possible (see Fig. 4.6).

Our antenna has circular geometry, consisting of four windings (radius 15 mm) and it is wound on a 3D-printed plastic mount that also houses the Stern-Gerlach coil, about 1 cm above the glass cell. The antenna is not impedance-matched to any particular frequency because it is designed to operate in a large range of frequencies (1 - 400 MHz).[13]

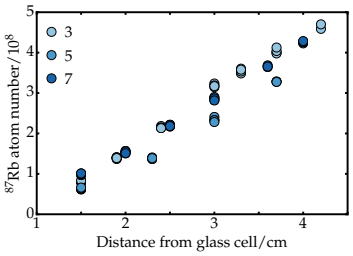

Figure 4.6: RF antenna coupling efficiency. The data represents the surviving ^{87}Rb-atoms after a 1s ramp from 30 MHz to 5 MHz in a steep-gradient (300 G/cm) magnetic trap, i.e. the fewer atoms the larger the coupling efficiency (or Rabi-frequency).

[13] It was also designed to perform RF evaporation on the m_F-states in ^{87}Rb.

4.6 *Feshbach fields*

Feshbach resonances [93, 183] are key to both the production of ultracold atomic gases and the application thereof. The physical origin of this phenomenon lies in the quantum-mechanical scattering process of two particles at low energies [184] which can be characterised by a single parameter called the scattering length.[14] This parameter, usually quoted in units of the Bohr-radius $a_0 = 5.29 \times 10^{-11}$ m, is a measure for the phase shift between the incoming and outgoing wave function of a scattered particle. Its value depends on the respective energy landscape of the inter-atomic molecular potential which, for a given atomic species, is hard to predict. This combined quantum state of the two scattering participants (in the limit of large separation) is called a scattering channel. The energy of a scattering channel depends on the composition of internal states and it can be shifted according to the Zeeman effect by applying a magnetic field. If the constituents of two scattering channels have a different composition of internal states then their respective molecular potentials can be tuned relative to each other. In particular, the energy of two free particles (an open scattering channel) can be brought

[14] At low energies, s-wave scattering dominates due to the centrifugal barrier [183] which surpresses higher-order scattering. The dominance of s-wave scattering defines the 'ultracold' regime.

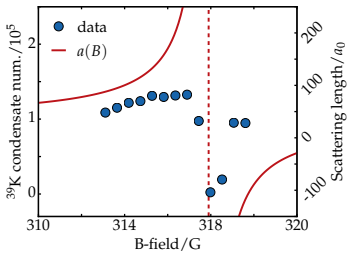

Figure 4.7: Experimental optimisation of the inter-species Feshbach field for ^{39}K - ^{87}Rb. The optimum field value (315.49 G) produces the largest ^{39}K-condensate. The data points are averages over three identical realisations and the error bars are smaller than the markers. The magnetic field (x-axis) is calibrated using an RF transfer in rubidium (table 3.2). The second y-axis shows the scattering length a (red line).

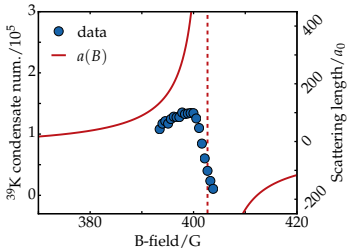

Figure 4.8: Experimental optimisation of the intra-species Feshbach field for ^{39}K (optimum value 397.8 G) using the ^{39}K-condensate number as figure of merit. The second y-axis shows the scattering length a (red line).

[15] The bosonic or fermionic particle symmetry influences the collective properties of the gas. This can, for instance, show up in the dynamics of the system, such as an anisotropic expansion of a thermal Bose gas after sudden release from the dipole trap [185].

Table 4.7: Feshbach resonance parameters. The values are taken from [93] except the resonance position for ^{39}K which has recently been measured to a much greater precision [130].

into resonance with a bound state of a different channel (a closed channel), leading to a maximum scattering phase shift of π and a diverging scattering length. This effect is called Feshbach resonance.

The scattering length (a) close to a Feshbach resonance is parametrised by the following function of the magnetic field

$$a(B) = a_{\mathrm{bg}}\left(1 - \frac{\Delta B}{B - B_{\mathrm{res}}}\right) \tag{4.8}$$

where the relevant values for a_{bg}, B_{res}, and ΔB are listed in table 4.7.

When producing condensates of ^{39}K we make use of both Feshbach resonances during evaporation, firstly to sympathetically cool ^{39}K with ^{87}Rb and secondly to reach quantum degeneracy with ^{39}K. The field is switched from inter-species to the intra-species value at the point when all ^{87}Rb has fallen out of the trap due to gravity, as detailed in table 4.4. These parameters are optimised to produce the largest condensates, as shown in Figs. 4.7 and 4.8.

4.7 *Quantum degeneracy and Bose-Einstein condensation*

The ultracold temperature regime is defined by the prevalence of s-wave scattering for bosons [183] or p-wave scattering for fermions, which are two-body collisional properties of the relevant atomic species. Such a system may still be thermodynamically described by classical Maxwell-Boltzmann statistics (although the scattering has to be already described quantum-mechanically[15]).

However, if the cloud is cooled down further, the density crucially affects the thermodynamics of the system. The phase-space density

$$\frac{n}{\lambda_{\mathrm{dB}}^3} \quad \text{where} \quad \lambda_{\mathrm{dB}} = \frac{h}{\sqrt{2\pi m k_{\mathrm{B}} T}} \tag{4.9}$$

replaces temperature as the relevant thermodynamic parameter because it relates the average inter-particle distance $n^{-1/3}$ to the thermal de Broglie wavelength λ_{dB}. When the phase-space density approaches unity [186] the classical Maxwell-Boltzmann description fails and must be replaced by the relevant quantum statistical expression. In this regime the symmetry properties of the individual quantum particles dominate all thermodynamic quantities. In particular, fermionic symmetry – the full many-body wavefunction is anti-symmetric under particle exchange – leads to Pauli exclusion, i.e. the fermionic occupation of a single quantum state

species	scattering channel	B_{res}/G	ΔB/G	a_{bg}/a_0
^{87}Rb/^{39}K	$1\times^{87}$Rb & $1\times^{39}$K in $\lvert F=1, m_F=1\rangle$	317.9	7.6	34
^{39}K	$2\times^{39}$K in $\lvert F=1, m_F=1\rangle$	402.70(3)	-52	-29

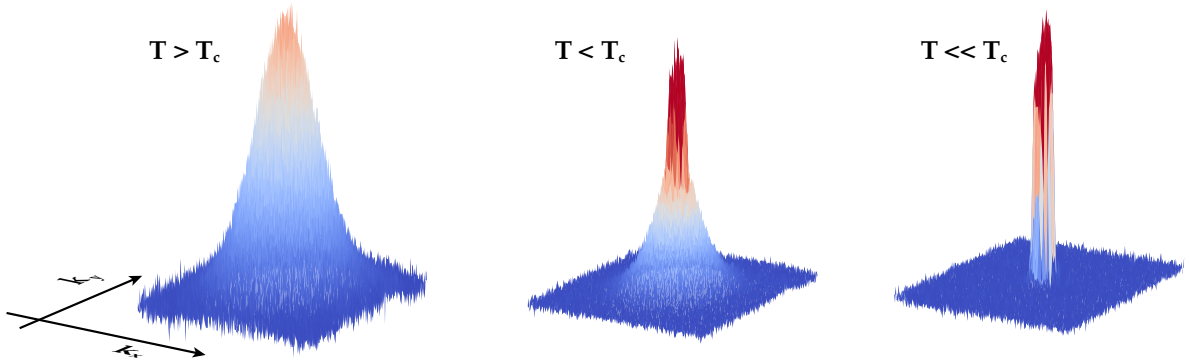

Figure 4.9: Bose-Einstein condensation in a gas of ^{39}K-atoms. The vertical coordinate in the surface plot corresponds to the optical density. A thermal gas ($T > T_c$) is well-described by the Maxwell-Boltzmann distribution, corresponding to a gaussian profile in time-of-flight. Below the critical point, a sharp feature at $\mathbf{k} = (0, 0)$ starts to appear which grows as the gas is cooled down further. For temperatures much lower than T_c, there is no discernible thermal fraction.

is bounded from above by 1. Conversely, bosonic symmetry – the many-body wavefunction is symmetric under particle exchange – leads to particle-bunching which allows bosonic systems to lower their energy by occupying a single quantum state. Statistically, these effects are captured by the average occupation

$$\langle n_i \rangle = \frac{1}{e^{(\epsilon_i - \mu)/(k_B T)} \mp 1} \tag{4.10}$$

of a given state $|i\rangle$ with energy ϵ_i. The minus-sign corresponds to bosonic, the plus sign to fermionic quantum statistics. The chemical potential μ has been introduced to ensure particle number conservation via

$$N = \sum_i \langle n_i \rangle \tag{4.11}$$

in the grand-canonical ensemble. In this work all lattice experiments were carried out with bosons and the remainder of this section will cover the relevant properties of ultracold bosons in a harmonic trap.[16]

[16] However, all necessary hardware has been set up to produce a Fermi-gas of ^{40}K.

Bose-Einstein condensation

As the temperature of the gas is reduced at constant density, the chemical potential approaches the value of the lowest energy level

$$\epsilon_0 = \begin{cases} 0 & \text{in a uniform system} \\ \frac{3}{2}\hbar\omega & \text{in an isotropic 3D harmonic trap} \end{cases} \tag{4.12}$$

from below. The occupation of the excited states then tends to a finite value, given by the number equation (Eq. 4.11).[17] Therefore, all remaining particles (in the thermodynamic limit $N \to \infty$) must occupy the ground state ϵ_0. This effect is known as Bose-Einstein condensation.

[17] For all excited states ($\epsilon_i > \epsilon_0$) the number equation can be solved analytically by replacing the sum by an integral.

Alternatively, condensation can be achieved by increasing the particle number N at fixed temperature. For an ideal Bose gas in a harmonic trap the critical particle number N_c is given by [186]

$$N_c = 1.202 \left(\frac{k_B T}{\hbar \bar{\omega}} \right)^3 . \tag{4.13}$$

Here $\bar{\omega}$ denotes the geometric mean of the trapping frequencies. For $N \geq N_c$ (at fixed T) the excited motional states are 'saturated' such that adding particles to the system solely increases the ground state occupation.[18]

[18] In a realistic scenario, however, at most half the added particles end up in the condensate and the other half is thermal [187].

Experimentally, the condensate can be detected in time-of-flight (see sections 3.12 and 6.2). It appears as a sharply peaked feature above the thermal background [97], as shown in Fig. 4.9. The profile of the condensate peak, a paraboloid, is a consequence of interatomic interactions and trapping geometry. Theoretically, these can be taken into account by the Gross-Pitaevskii equation in the Thomas-Fermi approximation [186].[19] The resulting real-space profile in an anisotropic harmonic trap is then given by

[19] by neglecting the kinetic energy term $-\frac{\hbar^2}{2m}\nabla^2$

$$n(\mathbf{r}) = n_0 \left(1 - \frac{x^2}{R_x^2} - \frac{y^2}{R_y^2} - \frac{z^2}{R_z^2}\right) \quad , \tag{4.14}$$

where R_i are the Thomas-Fermi radii in the three spatial directions and n_0 is the central density. Generally, the expansion of a trapped condensate in time-of-flight is anisotropic [97, 186] in contrast to the thermal gas which expands isotropically. Equation 4.14 gives rise to a parabolic density profile of the atomic cloud in time-of-flight which is used extensively in this work as a fit function to measure atom numbers. Thereby the equations quoted in ref. [160] are used.

Atom number calibration

The observation of a phase transition from a thermal to a Bose-condensed state provides a measurement of atom number which is independent of the specifics of the light-atom interactions of the atomic species in question. For ^{39}K in particular, a faithful atom number measurement via summing the optical density (section 3.12) is impossible due to the non-existence of a closed imaging transition, even at high magnetic fields where no repumping light is required (section 3.12).

5
Eightfold optical lattice

This chapter provides the theoretical and experimental groundwork for the experiments carried out in this thesis (Chapter 6). First, the basic equations for non-interacting particles in a 1D optical lattice are derived (section 5.1). Second, the single-particle dynamics following a sudden lattice quench is reviewed with a focus on using this method for lattice depth calibration. Third and last, the laser setup for the eightfold rotationally symmetric optical lattice is described (section 5.4).

5.1 1D optical lattice

The matter-wave experiments described in Chapter 6 can be treated in the usual Bloch-wave formalism. In this section the matrix hamiltonian for a single atom in a one-dimensional optical lattice is derived which forms the basis for all theoretical predictions in Chapter 6.

The dipole potential (Eq. 4.2) of a retro-reflected laser beam can be written as

$$V(x) = V_0 \cos^2(k_{\text{lat}} x) = \frac{V_0}{2}\left(1 + \frac{e^{i2k_{\text{lat}}x} + e^{-i2k_{\text{lat}}x}}{2}\right) \quad , \tag{5.1}$$

where any inhomogeneities and (anti-)confining potentials have been neglected.[1] Further, it is assumed that the incoming and the retro-reflected beams are perfectly counter-propagating. The lattice wavelength $\lambda_{\text{lat}} = 2\pi/k_{\text{lat}} = 726\,\text{nm}$ is far-blue-detuned with respect to the D-lines in ^{39}K, ensuring that single-photon processes are completely suppressed. The lattice depth[2] (V_0) can be expressed conveniently in units of photon recoil energy, i.e.

$$E_{\text{rec}} = \frac{h^2}{2m\lambda_{\text{lat}}^2} \quad . \tag{5.2}$$

Here m denotes the atomic mass and h Planck's constant; the relevant recoil energies for ^{87}Rb and ^{39}K are listed in table 5.1.

Due to the periodicity of the potential[3] (Eq. 5.1) we can invoke Bloch's theorem [188, 189] and introduce the quasimomentum q. The quantity

$$q \bmod 2k_{\text{lat}} \tag{5.4}$$

Table 5.1: Relevant recoil energies for ^{87}Rb and ^{39}K using the optical wavelength $\lambda_{\text{lat}} = 726\,\text{nm}$.

species	E_{rec}/h
^{87}Rb	4.35 kHz
^{39}K	9.71 kHz

[1] This assumption is valid for our experimental timescales since the longest lattice pulses are $t = 50\,\mu\text{s} \ll \frac{1}{\omega_{\text{trap}}}$.

[2] In principle, the value of V_0 could be calculated directly from Eq. 4.2. In practice, however, these estimations suffer from systematic uncertainties in the laser powers and beam waists. Therefore the lattice dynamics that are derived in the following will be used to calibrated V_0 since they provide a much more precise measure of lattice depth.

[3] the lattice spacing a is given by

$$a = \frac{\lambda_{\text{lat}}}{2} = \frac{2\pi}{2k_{\text{lat}}} \tag{5.3}$$

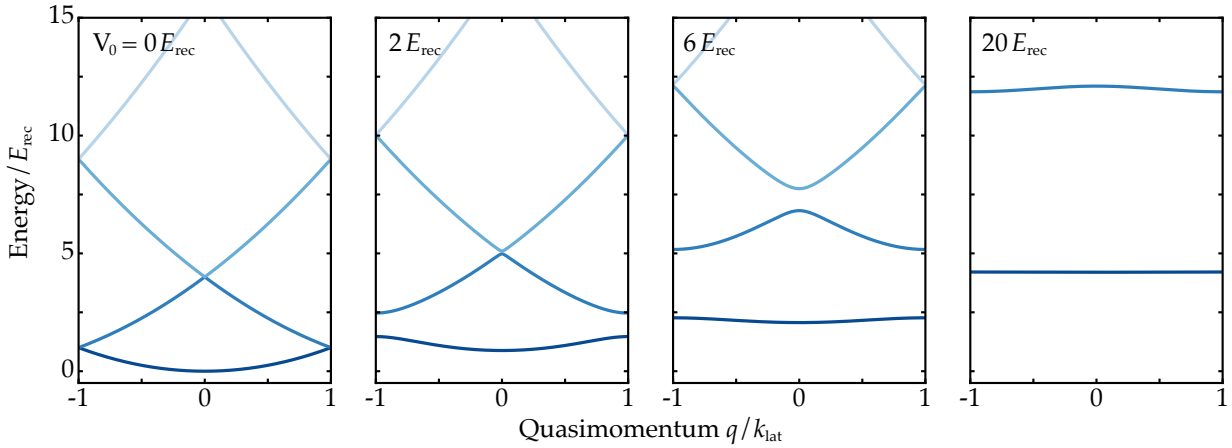

Figure 5.1: Band structure for non-interacting particles in a homogeneous, one-dimensional optical lattice. The solutions to Eq. 5.9 for $n \in \{0,1,2,3\}$ (deep blue to light blue) and $V_0/E_{rec} \in \{0,2,6,20\}$ (left to right) are shown. For small values of V_0 the optical lattice causes only small perturbations on top of the free-particle dispersion $p^2/(2m)$. Conversely, in the limit of deep lattices ($V_0 \gtrsim 5E_{rec}$) the $n = 0$ Bloch waves become more peaked around each lattice site, the bandwith becomes small, and the dispersion relation can be approximated by a cosine (tight-binding limit).

is conserved in a periodic potential. In the Bloch formalism the wave function takes the form

$$\underbrace{\psi_q^n(x)}_{\text{Bloch wave}} = \underbrace{u_q^n(x)}_{\text{Bloch function}} \times \underbrace{e^{iqx}}_{\text{plane wave}} \quad , \tag{5.5}$$

where the index n has been introduced to account for all possible solutions (bands) of the energy eigenvalue equation $\mathcal{H}\psi = E\psi$ (time-independent Schrödinger equation). The ansatz Eq. 5.5 can be inserted to the eigenvalue equation to yield

$$\left[-\frac{\hbar^2}{2m}\left(\frac{\partial^2}{\partial x^2} + q^2\right) + \frac{V_0}{2}\left(1 + \frac{e^{i2k_{lat}x} + e^{-i2k_{lat}x}}{2}\right)\right] u_q^n(x) = E_q^n\, u_q^n(x) \quad . \tag{5.6}$$

Bloch's theorem states that the functions $u_q^n(x)$ exhibit the same periodicity as $V(x)$, i.e. $u_q^n(x) = u_q^n(x+a)$, and consequently they can be decomposed in a discrete Fourier series:

$$u_q^n(x) = \sum_{l=-\infty}^{+\infty} c_l^n(q)\, e^{i2lk_{lat}x} \quad . \tag{5.7}$$

Inserting this expression into Eq. 5.6 results in

$$\sum_{l=-\infty}^{+\infty}\left[\left(-\frac{\hbar^2}{2m}\left((2lk_{lat})^2 + q^2\right) + \frac{V_0}{2}\right)e^{i2lk_{lat}x} + \frac{V_0}{4}\left(e^{i2(l+1)k_{lat}x} + e^{i2(l-1)k_{lat}x}\right)\right] c_l^n(q) = E^n(q) \sum_{l'=-\infty}^{+\infty} e^{i2l'k_{lat}x}\, c_{l'}^n(q) \quad , \tag{5.8}$$

which can be easily converted to the following matrix equation for $\mathcal{H}$

$$\sum_{l=-l_{max}}^{+l_{max}} \mathcal{H}_{l,l'} c_l^n(q) = E^n(q) c_{l'}^n(q) \quad . \tag{5.9}$$

The simplicity of the potential $V(x)$, which contains only two non-trivial Fourier components, namely $\pm 2k_{lat}$, ensures the straightforward derivation of Eq. 5.8 (no double summation on the left-hand

side). Consequently, the matrix $\mathcal{H}_{l,m}$ is sparse, the only non-zero elements being located on the diagonal and the first off-diagonal, i.e.

$$\mathcal{H}_{l,l'} = \begin{cases} \frac{\hbar^2}{2m}(q + 2lk_{\mathrm{lat}})^2 + \frac{V_0}{2} & \text{for} \quad l = l' \\ V_0/4 & \text{for} \quad |l - l'| = 1 \\ 0 & \text{otherwise.} \end{cases} \tag{5.10}$$

The truncation of the infinite basis of the coefficients $c_l^n(q)$ at certain values $\pm l_{\max}$ can be justified *a posteriori* since only a fraction of bands get populated.[4].

[4] This is not the case for the eightfold optical lattice and consequently the calculation of a ground-state energy in this formulation is usually impossible in that case (section 6.1).

The Bloch waves are delocalised over the whole lattice. However, it is possible to recover localised wave functions for each lattice site. These localised functions are called Wannier functions

$$w_n(x - x_i) = \frac{1}{\sqrt{M}} \sum_q e^{-iqx_i} \psi_q^n(x) \tag{5.11}$$

for each lattice site i (M is some normalisation). Bloch waves and Wannier functions are related via a discrete Fourier transform. Therefore, a localised particle (i.e. unity occupation of a single Wannier function) corresponds to a flat distribution of Bloch waves (each Bloch wave is equally populated). The Wannier functions form an alternative orthonormal basis to solve the Schrödinger equation.

The derivation above can be generalised to more sophisticated lattice geometries, as shown in section 6.1.

Band structure, tunnelling, and group velocity

In the case of periodic lattice geometries, for instance 1D or 2D simple-cubic, or 2D honeycomb geometry, the hamiltonian matrix in Eq. 5.10 can be diagonalised and the corresponding eigenvalues and eigenstates are exact. The eigenenergies are the well-known Bloch bands, depicted in Fig. 5.1 for different values of $V_0/E_{\mathrm{rec}} \in \{0, 2, 6, 20\}$. Two regimes emerge here: On the one hand, shallow lattices can be treated as a small perturbation on free-particle behaviour. On the other hand, deep lattices ($V_0 \gtrsim 5E_{\mathrm{rec}}$) lead to peaked Bloch functions around the lattice sites, corresponding to the tight-binding limit.

In the tight-binding limit the lowest band of the optical lattice corresponds to a discrete lattice with a fixed tunnelling energy between the sites. A measure for the tunnelling matrix element J between neighbouring lattice sites is the bandwidth of the lowest band, i.e.

$$J = \frac{\max(E_q^0) - \min(E_q^0)}{4} \quad . \tag{5.12}$$

The dispersion relation in this case (deep blue line in rightmost plot in Fig. 5.1) is the characteristic cosine of the tight-binding model [188]:

$$E(q) = -2J\cos(qa) \quad , \tag{5.13}$$

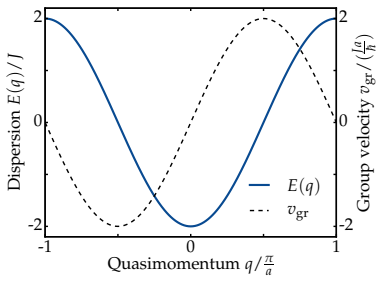

Figure 5.2: Tight-binding dispersion relation and its derivative, the group velocity.

where a is the lattice spacing (Eq. 5.3). This dispersion relation is plotted in Fig. 5.2 together with the corresponding group velocity

$$v_{\mathrm{gr}} = \frac{1}{\hbar}\frac{\partial E(q)}{\partial q} = \frac{2Ja}{\hbar}\sin(qa) \quad . \tag{5.14}$$

Higher dimensions and quantum walks

In the case of D-dimensional separable lattices Eq. 5.13 generalises to

$$E(\mathbf{q}) = -2J\sum_{i=1}^{D}\cos(aq_i) \quad , \tag{5.15}$$

where $\mathbf{q}$ is now a D-component vector. Correspondingly, the individual components of the group velocity are given by

$$v_i(\mathbf{q}) = \frac{1}{\hbar}\frac{\partial E(\mathbf{q})}{\partial q_i} = \frac{2Ja}{\hbar}\sin(aq_i) \quad . \tag{5.16}$$

For a given Wannier state that is initially localised to one lattice site all Bloch waves are equally populated, leading to an average root-mean-square group velocity

$$\sqrt{\overline{\mathbf{v}^2}} = \frac{2Ja}{\hbar}\sqrt{\sum_{i=1}^{D}\overline{\sin^2(aq_i)}} = \frac{2Ja}{\hbar}\sqrt{\frac{D}{2}} \quad . \tag{5.17}$$

The $\sqrt{D}$ scaling will be recovered exactly in the experiment (Chapter 6) for $D \in \{1,2,3,4\}$.

5.2 *Time-evolution and lattice depth calibration*

Let us now consider the time-evolution of an optical lattice system according to the time-dependent Schrödinger equation

$$i\hbar\frac{\mathrm{d}\psi}{\mathrm{d}t} = \mathcal{H}\psi \quad . \tag{5.18}$$

As a first example the ballistic expansion of a particle initially localised to one single lattice site will be shown.

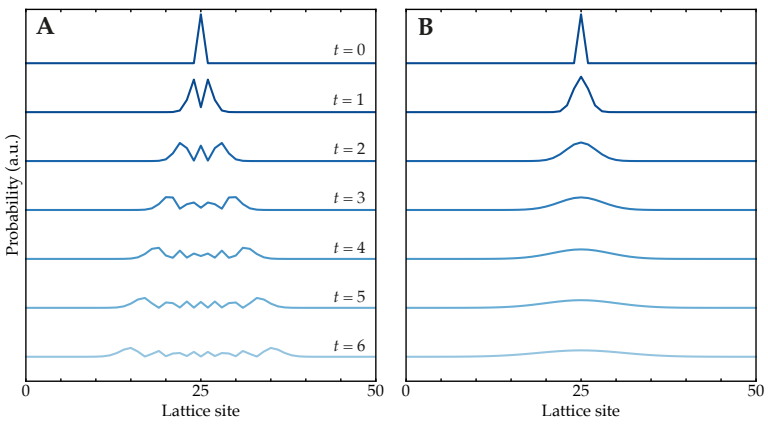

Figure 5.3: (**A**) Quantum walk on a 1D homogeneous tight-binding lattice. Initially the particle is localised to one lattice site (deep blue, top). With time, it spreads ballistically in both directions, giving rise to a 'light-cone' with a constant group velocity given by Eq. 5.17 for $D = 1$. Times are given in units of tunnelling times $\hbar/J$. (**B**) Classical random walk (schematic). Particles initially localised to one lattice site are allowed to hop to neighbouring sites with a certain probability. Contrary to the quantum case, the expansion is diffusive, i.e. gaussian.

Homogeneous tight-binding lattice

In the limit of deep lattices ($V_0/E_{\mathrm{rec}} \gg 1$) it is convenient to work in the Wannier-basis and the system describes only the direct coupling of nearest neighbours (homogeneous tight-binding model). The hamiltonian reads

$$\mathcal{H}_{i,j} = \begin{cases} J & \text{for} \quad |i-j'| = 1 \\ 0 & \text{otherwise.} \end{cases} \tag{5.19}$$

Note that we have changed basis compared to Eq. 5.10 such that the lattice sites i denote the Wannier functions $w^0(x - x_i)$. The initial state $\psi(t = 0)$ for time-evolution shall simply be unity probability at one lattice site. The time-evolution $\psi(t)$ according to Equation 5.18 can readily be solved, for example using the `scipy.integrate` package, leading to a linear expansion of the wavepacket over the entire lattice. This light-cone-like behaviour (depicted in Fig. 5.3A) has no classical analogon. Therefore this effect has been coined 'continuous quantum walk' [22, 190, 191] in order to differentiate it from a classical random walk (Fig. 5.3B).

Table 5.2: Scheme to group the basis states for a 1D optical lattice.

order	states
0^{th}	$\{\lvert q=0\rangle\}$
1^{st}	$\{\lvert +2k_{\mathrm{lat}}\rangle, \lvert -2k_{\mathrm{lat}}\rangle\}$
2^{nd}	$\{\lvert +4k_{\mathrm{lat}}\rangle, \lvert -4k_{\mathrm{lat}}\rangle\}$
n^{th}	$\{\lvert +2nk_{\mathrm{lat}}\rangle, \lvert -2nk_{\mathrm{lat}}\rangle\}$

Time-evolution in momentum space for square lattice pulses

In our experiment we are primarily interested in the time-evolution of a Bose-Einstein condensate initially at rest, i.e. localised in momentum space. The time-evolution after a sudden switch-on (quench) of the lattice potential can be calculated via integrating the time-dependent Schrödinger equation (Eq. 5.18), as before. In this case it will be beneficial to work in the original basis $\{\lvert q=0\rangle, \lvert \pm 2k_{\mathrm{lat}}\rangle, \lvert \pm 4k_{\mathrm{lat}}\rangle, \dots\}$ and not in the Wannier basis. Although the following considerations apply to reciprocal space, it is instructive to keep the Wannier-picture at the back of one's mind. It provides a useful analogy in which momentum states separated by $2k_{\mathrm{lat}}$ correspond to 'neighbouring lattice sites', coupled by a 'tunnelling matrix element' $V_0/4$. This will become clearer in Chapter 6.

The kinetic energy part on the diagonal of $\mathcal{H}_{l,l'}$ (Eq. 5.10) now crucially affects the dynamics of this system. It leads to an effective restoring force that causes the condensate to return to its original state ($\lvert q=0\rangle$). In preparation for the quasicrystalline lattice the basis shall be labelled according to the number of $\pm 2k_{\mathrm{lat}}$ steps in momentum space from $\lvert q=0\rangle$, each step being one 'diffraction order', as shown in table 5.2. This is convenient because the hamiltonian (Eq. 5.10) is symmetric in $q \leftrightarrow -q$ such that all resulting states in the time-evolution obey the same symmetry.

In a one-dimensional periodic lattice[5] the numerical solution to Eq. 5.18 is exact, because only a limited number of orders get populated. This result is shown in Fig. 5.4 (lines), together with experimental data (points). The experimental points are the relative atomic population of each order of q-states.[6]

Agreement between theory and experiment is very good, except for short pulse durations for which a slight 'lag' of the experi-

[5] any periodic lattice, e.g. 2D and 3D simple-cubic, or 2D triangular

[6] The measurement and data-analysis procedures are explained in detail in section 6.5 and 6.2, respectively.

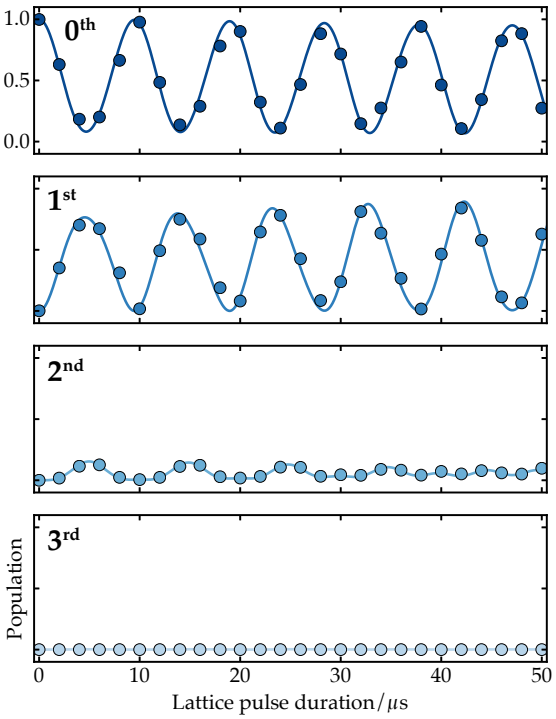

Figure 5.4: Time-evolution of a Bose-Einstein condensate after a sudden lattice quench ($V_0 = 15.7E_{\mathrm{rec}}$) of the D lattice axis (see below for naming convention of axes). The plot shows the time evolution grouped by diffraction order; the 0^{th} order corresponds to the condensate, the 1^{st} order to the satellite peaks at $\pm 2k_{\mathrm{lat}}$. For information on image analysis the reader is referred to section 6.5.

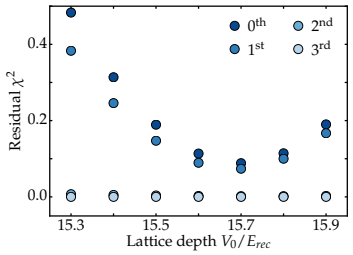

Figure 5.5: Lattice depth calibration using time-evolution following a sudden quench to a given lattice depth V_0. The y-axis shows the squared and summed difference between the experimental values (points in Fig. 5.4) and the numerical calculation using the depths shown on the x-axis. The best fit in this case is obtained with a lattice depth of $V_0 = 15.7E_{\mathrm{rec}}$ (lines in Fig. 5.4).

mental data can be observed. This is due to a finite ramping-up time of the lattice pulse on the order of 1 µs. This effect can be accounted for by making the hamiltonian (Eq. 5.10) time-dependent (see Chapter 6.5) but for now it will be neglected.

Lattice depth calibration

We use the well-understood process described above to calibrate precisely our lattice depth by comparing experiment and theory. In fact, the lines in Fig. 5.4 were calculated using the calibration method summarised in the following. For a given (unknown) experimental value of V_0 a data trace of the type shown in Fig. 5.4 is taken by varying the duration of the (square) lattice pulse. Subsequently, the exact time-evolution is calculated according to the Schrödinger equation for a number of lattice depths and the best fit to the experiment is found via the least-squares method (shown in Fig. 5.5).

The lattice depths of all four lattice axes (see below) are calibrated in this way.

After discussing the properties and dynamics of 1D optical lattice we turn to the description of the full, quasicrystalline lattice.

5.3 *Eightfold optical lattice potential*

The 2D quasicrystalline potential is created using a planar arrangement of four mutually incoherent 1D optical lattices, each formed by retro-reflection of a single-frequency laser beam, as shown schematically in Fig. 5.6. The angle between two neighbouring lattice axes is $45(1)^\circ$, thereby imposing a global eightfold

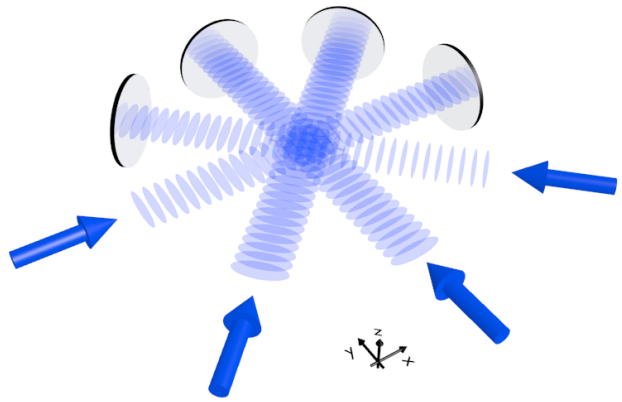

Figure 5.6: Schematic of the eightfold optical lattice. The four lattice axes are mutually incoherent such that the resulting potential is the sum of four 1D lattices. Each 1D lattice is formed by retro-reflection, as shown in the schematic. However, most of the optics involved in the retro-reflection are not shown. In the apparatus, a cat's eye configuration is used in which there are two lenses in between the atoms and the retro-mirror. The distance from the atoms to the retro-mirror should be exactly twice the sum of the individual focal lengths of the lenses in order to ensure approximately equal beam waists at the position of the atoms.

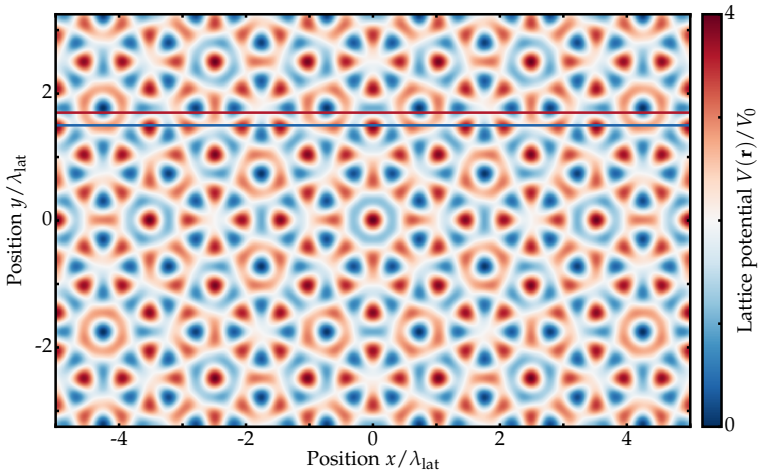

Figure 5.7: Lattice potential resulting from four non-interfering axes (blue-detuned). The phases φ_i have been chosen such that the symmetry point is located at $\mathbf{r} = (0, 0)$ and coincides with a potential maximum (maximally constructive interference). There are roughly as many maxima as there are minima in this potential.

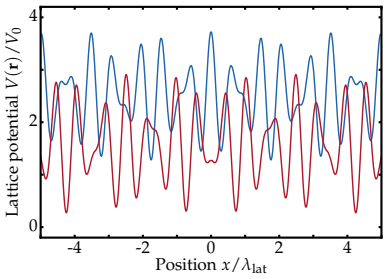

Figure 5.8: Two cuts through the lattice potential shown in Fig. 5.7. The curves are color-coded by the horizontal lines in Fig. 5.7. The distribution of potential maxima and minima is roughly symmetrical around the average potential value ($2\,V_0$).

rotational symmetry in close analogy to the octagonal tiling (section 1.3).

In the following section some basic properties of this eightfold lattice *in real space* are described. For the momentum-space picture, the reader is referred to Chapter 6.

First, we consider the situation of four mutually incoherent lattice beams, which also has been used for all experimental results in Chapter 6. Afterwards, alternative schemes that make use of inter-axis interference are considered.

Incoherent superposition

The sum of four mutually incoherent[7] lattice axes of equal depth V_0 can be written as[8]

$$V(\mathbf{r}) = V_0 \sum_{i=1}^{4} \cos^2\left(\mathbf{k}_i \cdot \mathbf{r} + \varphi_i\right) \quad , \tag{5.20}$$

[7] The terms 'non-interfering' and 'incoherent' only apply to the inter-axis interference in this context. Of course, the 1D lattices themselves are a result of intra-axis interference.

[8] neglecting any anti-confinement

where the individual lattice vectors $\mathbf{k}_i$ are given by

$$\frac{\mathbf{k}_1}{k_{\text{lat}}} = \begin{pmatrix} 1 \\ 0 \end{pmatrix}, \quad \frac{\mathbf{k}_2}{k_{\text{lat}}} = \begin{pmatrix} 0 \\ 1 \end{pmatrix}, \quad \frac{\mathbf{k}_3}{k_{\text{lat}}} = \frac{1}{\sqrt{2}} \begin{pmatrix} 1 \\ 1 \end{pmatrix}, \quad \frac{\mathbf{k}_4}{k_{\text{lat}}} = \frac{1}{\sqrt{2}} \begin{pmatrix} -1 \\ 1 \end{pmatrix} \tag{5.21}$$

and the individual phases $\varphi_1, \varphi_2, \varphi_3, \varphi_4$ are determined by the longitudinal position of the retro-reflecting mirror.[9] The potential Eq. 5.20 is shown in Fig. 5.7 for the case that all $\varphi_i = 0$. Since our lattice is blue-detuned with respect to the D-lines in both ^{87}Rb and ^{39}K, an intensity maximum results in a potential maximum. In this particular choice of phases (all $\varphi_i = 0$), the point $\mathbf{r} = (0, 0)$ corresponds to the point of maximally constructive interference ($V(0,0) = 4V_0$).[10] In addition, the whole potential is eightfold rotationally symmetric around this point.[11] Two cuts through the potential are shown in Fig. 5.8 which correspond to the horizontal lines of the same colour in Fig. 5.7.

If we were to interpret each minimum of $V(\mathbf{r})$ as a 'lattice site', it is immediately clear from Fig. 5.8 that the vast majority of lattice sites (or 'wells') is located at different energies. Moreover, the ground level $\hbar\omega$ of each well in harmonic approximation[12] varies strongly. Since deeper wells tend to have stronger curvatures this effect leads to an even larger spread in energies. For these reasons the potential $V(\mathbf{r})$ cannot exhibit a band structure as in the equivalent single-axis case (section 5.1). In addition, tunnelling is inhibited by the energy offset between neighbouring sites.

[9] The individual lattice axes are created by retro-reflection, resulting in a standing wave. Therefore the phase of the incoming light is exactly cancelled.

[10] The irrationality of $\cos 45° = 1/\sqrt{2}$ ensures that this value of $V(\mathbf{r})$ occurs exactly once and consequently it is the global maximum of the $V(\mathbf{r})$. However, there will always be values of $V(\mathbf{r})$ that are arbitrarily close to the global maximum.

[11] and only around this point

[12] given by the curvature of the well in the x and y directions

Relation to octagonal tiling

It is interesting to compare the resulting potential $V(\mathbf{r})$ to the octagonal tiling (Fig. 1.19). In the easiest case, we choose all phases φ_i to be equal to $\pi/2$ in which case the central point $(0, 0)$ shows maximally destructive interference ($V(0,0) = 0$). This potential bears a close resemblance to the ideal octagonal tiling (Fig. 1.19) with a bond length of approximately $0.6\lambda_{\text{lat}}$. Alternatively, the actual minima of $V(\mathbf{r})$ can be directly connected by lines to reproduce an approximate version of the octgonal tiling. This process is shown in Fig. 5.9 for $\varphi_i = \pi/2$.

The exact knowledge of all phases φ_i is unrealistic in a real experimental setting (see below). However, the octagonal tiling-effect is relatively robust against a random choice of (constant) phases, as shown in Fig. 5.10 in which all phases φ_i have been chosen at random in between 0 and π. The random choice of phases leads to the appearance of 'defects' or closely-spaced 'double wells' which can be seen in Fig. 5.10 upon close inspection. These effects can be interpreted as phasonic excitations, since the manner in which they appear is identical to that of the ideal octagonal tiling (Fig. 1.20). Despite the random choice of phases, the agreement between the potential and the ideal octagonal tiling is very good. Consider, for example, the length of the 'bonds' (black lines connecting the lattice points) and 'gaps' (the shorter diagonal of the rhombus tile), the occurrence of which are plotted in Fig. 5.11 for

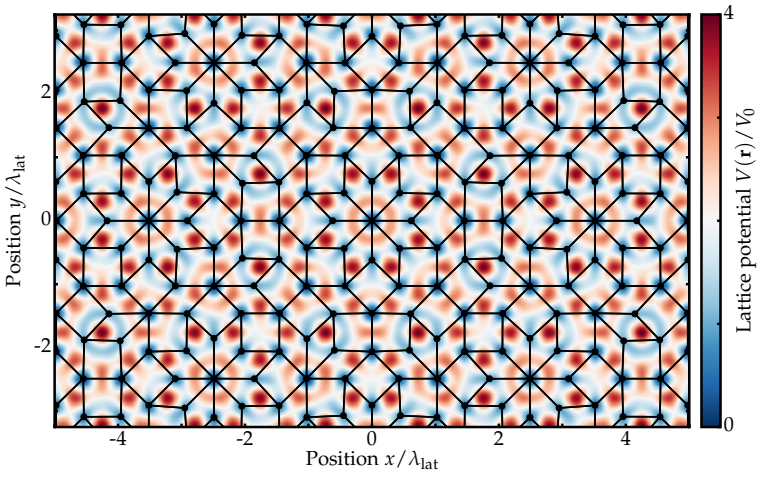

Figure 5.9: Lattice potential resulting from four non-interfering axes, overlaid with the corresponding minima (black points) and 'bonds' (lines). Upon close inspection, the lattice points and bonds can be seen not to exactly represent the octagonal tiling. The phases φ_i have been chosen such that the symmetry point is located at $\mathbf{r} = (0, 0)$ and coincides with a potential minimum (maximally destructive interference). The bonds shown here are not necessarily the physical bonds (shortest distance or largest tunnelling matrix element) between lattice sites but they nicely illustrate the similarity to the octagonal tiling.

the random-phases potential. The ratio between the mean values of the two is remarkably close to the ideal value of the octagonal tiling:

$$\frac{0.478(6)}{0.60(2)} = 0.80(4) \simeq 2\sin\left(\frac{\pi}{8}\right) = 0.765\ldots \quad . \tag{5.22}$$

Sampling from a larger window than Fig. 5.10 would result in an even better agreement.

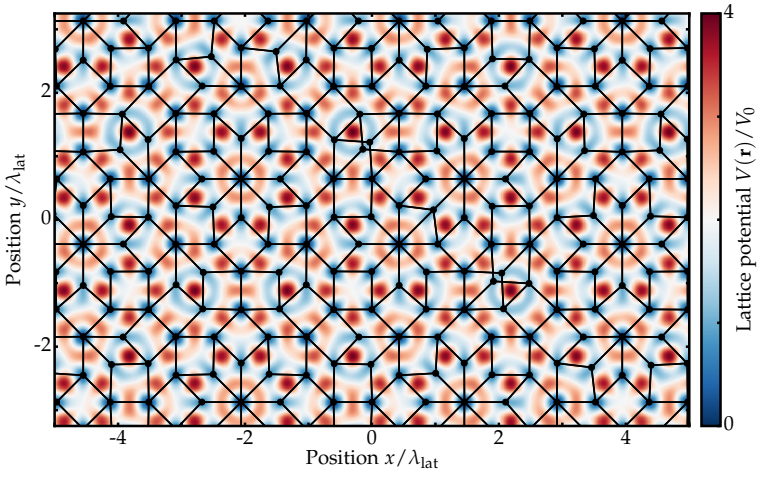

Figure 5.10: Lattice potential resulting from four non-interfering axes. The phases φ_i have been randomly chosen between 0 and 2π.

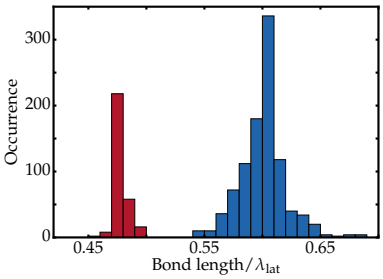

Figure 5.11: Histogram of bond lengths (blue) and gap widths (red) for the random-phases lattice patch shown in Fig. 5.10. The gaps are the short diagonals of the rhombus-like tiles. The mean (standard deviation) of this distribution is $0.60(2)\,\lambda_{\mathrm{lat}}$ and $0.478(6)\,\lambda_{\mathrm{lat}}$, respectively.

So far we have considered static phases φ_i and the resulting potentials $V(\mathbf{r})$ whose overall structure closely resembles the octagonal tiling in introduced in Chapter 1. Further studies are necessary to decide how exactly the eightfold lattice potential can be used to faithfully model the octagonal tiling. Some of these points will be addressed in the Outlook. Experimentally, one very important question is whether or not phase changes during

the course of the sequence will result in strong heating in this eightfold lattice, as discussed in the following.

Phase control

The phase φ of a 1D lattice potential that is created by retro-reflection is effectively determined by the path length from the atoms to the retro-reflecting mirror. If this path length varies with time the phase φ changes accordingly.

Alternatively, the phase of a lattice that is created by the interference of running waves can be controlled by changing the incoming phase of the laser light, e.g. by a phase-locked-loop or by deliberately changing the laser frequency.

[13] achived either by stabilisation or deliberate phase changes

Control over the phase[13] of optical lattices have become a cornerstone in quantum simulation experiments, for example in splitting and combining double-well potentials [192]. However, the application of phase control to quantum gas experiments sometimes shows unexpected subtleties. For instance, the powerful method of engineering a variety of hamiltonians by periodically modulating the lattice phases (Floquet engineering [29, 193]) has often been limited to short measurement times and weakly interacting gases [194] due to heating. Understanding the role of interactions, in particular, in the heating processes of periodically modulated systems is a field of active research [195–197]; the precise control over the bandwidths of the higher-lying Bloch bands might be a way to mitigate heating [25].

In our experimental setting, the question of phase control is particularly subtle. The fundamental reason for this is precisely the aperiodicity of our lattice potential. In contrast to periodic lattices, in which up to two relative phases can be absorbed into the global centre-of-mass motion of the atoms, in our case there are more than two such phases (φ_i).

The non-local effect of changing any of the phases φ_i can be seen by equating an arbitrary-phase potential $V(\mathbf{r})$ with a fixed-phase potential that is displaced by $\mathbf{r}_0 = (x_0, y_0)$, i.e.

$$\sum_{i=1}^{4} \cos^2\left(\mathbf{k}_i \cdot \mathbf{r} + \varphi_i\right) = \sum_{i=1}^{4} \cos^2\left[\mathbf{k}_i \cdot (\mathbf{r} - \mathbf{r}_0)\right]$$

which leads to

$$\begin{aligned}
\varphi_1 &= k_{\text{lat}} x_0 \\
\varphi_2 &= k_{\text{lat}} y_0 \\
\varphi_3 &= -\frac{k_{\text{lat}}}{\sqrt{2}}(y_0 + x_0) \\
\varphi_4 &= -\frac{k_{\text{lat}}}{\sqrt{2}}(y_0 - x_0) \quad .
\end{aligned}$$

Combining these equations yields

$$\varphi_3 = -\frac{1}{\sqrt{2}}(\varphi_2 + \varphi_1) \tag{5.23}$$

$$\varphi_4 = -\frac{1}{\sqrt{2}}(\varphi_2 - \varphi_1) \quad , \tag{5.24}$$

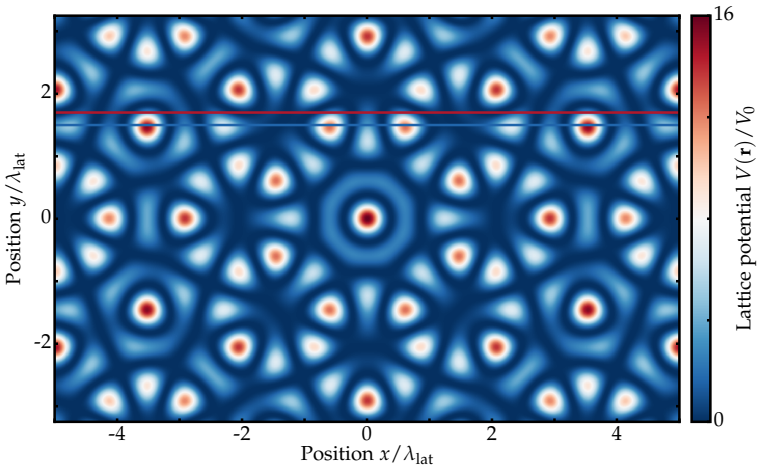

Figure 5.12: Lattice potential resulting from four fully-interfering axes (blue-detuned). The phases φ_i have been chosen such that the symmetry point is located at $\mathbf{r} = (0,0)$ and coincides with a potential maximum (maximally constructive interference). Compared to the non-interfering case, the potential maximum is a factor of four higher in energy.

which defines a plane in $\mathbb{R}^4$ on which the vector $(\varphi_1, \varphi_2, \varphi_3, \varphi_4)$ has to move in order to maintain a simple centre-of-mass motion of the quasicrystalline lattice potential. Any phase changes outside this plane will result in a physical change of the lattice potential. In particular, changing any single phase φ_i without changing the others accordingly, will result in a non-local potential deformation; some sites will disappear and others will appear from nowhere, in close analogy with phasonic excitations mentioned in Chapter 1 that are characteristic for quasicrystals. Therefore it seems likely that the mechanical stability of the retro-reflecting beam path will play a crucial role in the performance of the eightfold optical lattice, particularly once atoms have been loaded into the lattice potential. It would then be very interesting to deliberately excite phasonic modes by slightly displacing one (or several) of the retro-mirrors.

Before we turn to the experimental results in momentum space, the situation of fully-interfering lattice beams will be discussed briefly in the following.

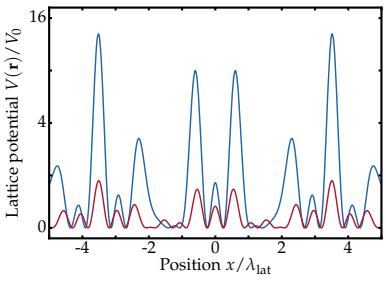

Figure 5.13: Two cuts through the interfering lattice potential shown in Fig. 5.12 color-coded accordingly. In contrast to the non-interfering case, potential maxima are steep and isolated.

Fully-interfering axes

The lattice potential from four interfering lattice axes can be written as[14]

$$V(\mathbf{r}) = V_0 \left[\sum_{i=1}^{4} \cos\left(\mathbf{k}_i \cdot \mathbf{r} + \varphi_i\right) \right]^2 \quad . \tag{5.25}$$

Experimentally, this can be achieved by simply removing the frequency offsets between each lattice beam. If two or more lattice axes interfere with each other, their respective polarisations also crucially affect the resulting potential. Equation 5.25 only covers the situation of out-of-plane polarisation, i.e. the polarisation of each lattice beam being at right angles to the lattice plane. The opposite case (in-plane polarisation) leads to a modification of the

[14] although the potential should, strictly speaking, include eight individual phases, four incoming and four retro-reflected phases. However, for practical purposes in this work it will be sufficient to consider just four independent phases.

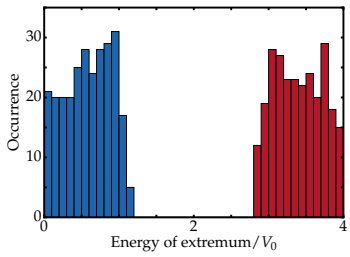

Figure 5.14: Histogram of minima (blue) and maxima (red) of the exact potential shown in Fig. 5.10 (random phases, non-interfering, blue-detuned lattice). The non-interfering case produces roughly equal amounds of minima and maxima, their distribution is approximately symmetric around $2V_0$.

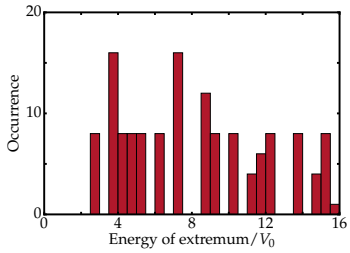

Figure 5.15: Histogram of maxima (red) of the exact potential shown in Fig. 5.12 ($\varphi_i = 0$, fully-interfering, blue-detuned lattice). The minima would all cluster around zero and have thus been omitted from this plot. In comparison the non-interfering case (Fig. 5.14 above) the maxima are spread out more. The eightfold rotational symmetry is reflected in the histogram by the appearance of maxima in groups of eight.

potential but the overall structure remains similar to the out-of-plane configuration.

In comparison to the non-interfering case discussed above (Figs. 5.7 and 5.8), constructive interference between four axes occurs much less frequently. Consequently, the resulting potential landscape (Eq. 5.25) is dominated by steep, isolated maxima, which are surrounded by a 'floor' of minima, as shown in Fig. 5.12. This effect becomes even more apparent when considering cuts through the potential (Fig. 5.13), emphasising the importance of interference in the eightfold lattice (c.f. Fig. 5.8).

Similar to the non-interfering case, the potential in Eq. 5.25 bears strong similarities with the octagonal tiling, a fact that has been discussed extensively by Jagannathan et al. [85, 198–200]. However, in contrast to the non-interfering case, the octagonal tiling only applies to points of maximally *constructive* interference (the isolated maxima discussed above). This means that in order to model the octagonal tiling physically with cold atoms we would have to change the detuning of our lattice from blue- to red-detuned in order to convert the intensity maxima to potential minima. Conversely, the tunnelling between these lattice points (as discussed in ref. [198]) might more closely resemble physical 'tight-binding' bonds between lattice sites, compared to the non-interfering case in which the bonds between lattice sites dictated by the octagonal tiling may or may not correspond to the physically most relevant tunnelling matrix elements. Another drawback of the interfering case is that there are numerous shallow 'local' intensity maxima surrounding the strong 'octagonal' lattice points and it is unclear whether these affect the equilibrium behaviour of a quantum gas in such a lattice. Regarding the 'bands' of energy minima, the non-interfering case comes closer to forming a well-defined band of allowed energies (Fig. 5.14), whereas the fully-interfering case shows maxima distributed over the entire range of the potential (Fig. 5.15).

Partly-interfering axes

The case of partly-interfering lattice axes is particularly interesting since it allows the creation of an separable 2D quasiperiodic potential. If two orthogonal lattice axes are chosen to interfere with each other, whereas the other two axes shall be non-interfering, the potential can be written as

$$V(\mathbf{r}) = V_0 \sum_{i=1}^{2} \cos^2\left(\mathbf{k}_i \cdot \mathbf{r} + \varphi_i\right) + V_0 \left[\sum_{i=3}^{4} \cos\left(\mathbf{k}_i \cdot \mathbf{r} + \varphi_i\right)\right]^2 . \tag{5.26}$$

A potential of this kind is shown in Fig. 5.16, which is quasiperiodic in both x and y direction, but *without* global eightfold rotational symmetry. This potential landscape is similar to the 2D bichromatic lattice employed in ref. [24]. It highlights the flexibility of our eightfold lattice setup, being able to produce both

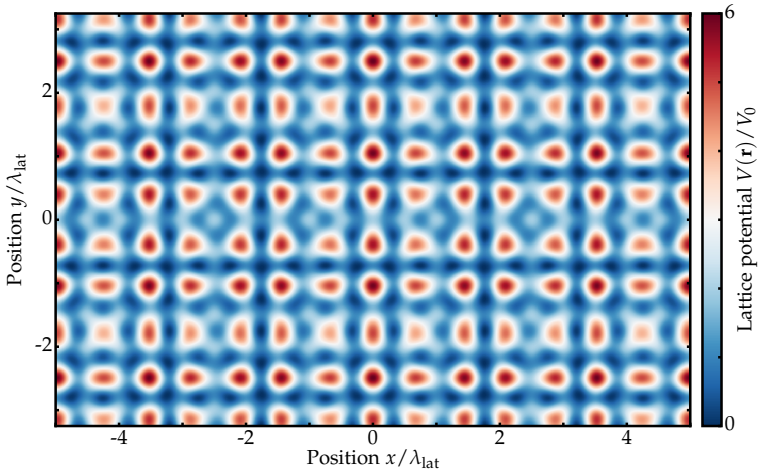

Figure 5.16: Lattice potential resulting from two fully interfering axes and two non-interfering axes (Eq. 5.26. The phases φ_i are chosen to be $(0, 0, \pi/2, \pi/2)$.

separable and non-separable quasiperiodic potentials in two dimensions.

This completes the discussion of attainable real-space potentials. Next, the setup and characterisation of the eightfold lattice (non-interfering case) will be summarised.

5.4 *Setup and characterisation*

The lattice setup is depicted schematically in Fig. 5.17. The axes have been labelled X, Y, D(iagonal), and T(transport). Only the last achromat before the atoms is shown in the schematic.

Laser setup

The lattice beams are derived from one single-frequency Ti:Sa laser[15] at $\lambda_{\mathrm{lat}} = 726\,\mathrm{nm}$ which is far-blue-detuned with respect to the D-lines in ^{39}K, ensuring suppression of single-photon scattering. Cross-interferences between lattice axes are avoided by offsetting their frequencies by more than 10 MHz from each other. Therefore, the corresponding beat notes between the axes oscillate much faster than the atomic kinetic energy scale, given by E_{rec}/h (table 5.1).

[15] Matisse, Sirah Lasertechnik GmbH, max. 7 W with RefCell locking. The Ti:Sa crystal is pumped by a Millennia laser (Spectra Physics) producing 24 W of power at 532 nm.

Beam waists

The choice of lattice beam waists is governed by essentially the same trade-off as for the dipole beam waists.

- Similar to the dipole trap waists, small lattice waists lead to the highest peak intensity and, consequently, the deepest lattice potential. Therefore, the lattice beam waists should be chosen as small as possible, given a certain maximum optical power (on the ordon the order off 200 mW per beam).

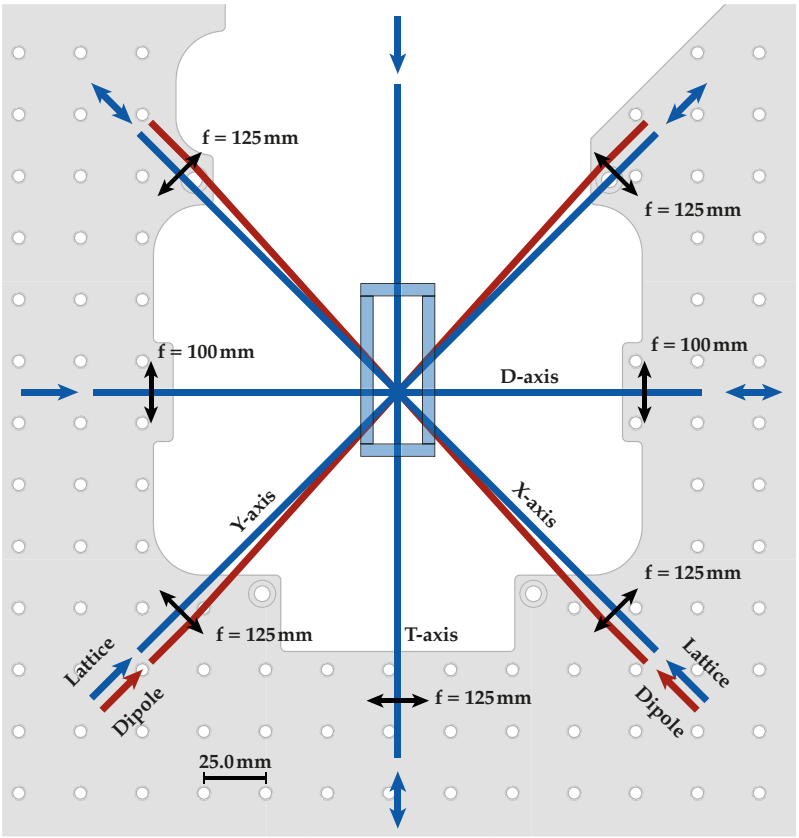

Figure 5.17: Schematic of the science cell optics (lattice in blue and dipole in red). The axes have been labelled X, Y, D(iagonal), and T(transport). The last achromats before the atoms are shown as black double-headed arrows, with their corresponding focal lengths (except for the T-axis for which only one of them is shown). The glass cell is shown in light blue (actual dimensions).

- Conversely, large in-plane lattice waists (compared to the extent of the atomic cloud) are beneficial in order to ensure homogeneity of the lattice potential.[16]

Elliptical beam profiles are a good compromise between the two. The in-plane waists are chosen as large as possible, whereas the vertical waists can be reduced in order to increase the maximum achievable lattice depth. In addition, the retro-reflecting configuration increases the maximum depth (given a certain maximum available beam power) by a factor of two.

In the fully-interfering case, the maximum lattice depth is a factor of four higher in the fully-interfering case (see Fig. 5.12, compared to Fig. 5.7), which could support even larger lattice waists (given a maximum power).

Blue-detuned lattices lead to an overall anti-confinement resulting from the spatially-varying on-site trapping frequencies $\omega_{\text{on-site}}(\mathbf{r})$. The ground state energy in each well is given by the lowest harmonic oscillator energy $E(\mathbf{r}) = \hbar\omega_{\text{on-site}}(\mathbf{r})$ in the two-dimensional case (two lattice beams overlapped in-plane at 90°). The in-plane envelope $E(\mathbf{r})$ is also approximately gaussian.[17] Consequently the anti-confining effect can compensated by weak co-propagating red-detuned dipole beams with larger waists by a factor of $\sqrt{2}$. Alternatively, a single red-detuned laser beam in the vertical direction (also with a factor of $\sqrt{2}$ larger waist) can be used to the same effect.

[16] An overall homogeneous potential is desirable to compare cold-atom quantum simulation experiments to condensed-matter theory, which is often performed in homogeneous lattices. In most lattice experiments the potential envelope is gaussian which necessitates a density-dependent theoretical description of the system. A well-known example is the bosonic or fermionic Mott-insulator. The characteristic 'wedding-cake' density profile can be described by the local-density approximation.

[17] In a 1D lattice the situation is separable and thus the gaussian anti-confinement is exact.

In the eightfold optical lattice these considerations are tricky since the lattice potential is not periodic and it is unclear which of the 'lattice sites' – which are all at different energies, even in the homogeneous case – should be taken into account for the anti-confinement. As a guideline, we aimed at a ratio of in-plane waists between lattice and dipole trap of roughly $\sqrt{2}$. However, spatial and physical constraints (gaussian beam-propagation with certain minimal distances in between the components and limited choices of focal lengths) led to slightly smaller waists than initially intended (see table 5.3). In addition, preliminary calculations taking into account the entire spread of 'lattice sites' show that the eightfold case leads to an anti-confining waist that is *smaller* than the lattice waists by a factor of $2^{1/4}$. We plan to counteract for anti-confining effects using a dedicated dipole trap beam along the z-axis.

The vertical beam waists (table 5.3) are chosen such that the lattice intensity varies as little as possible across the atomic cloud.

Using our maximum power (several hundred mW per beam) we can achieve single-axis lattice depths of at least 40 E_{rec}.

Table 5.3: Experimental values for the in-plane (w_r) and vertical (w_z) lattce beam waists (single waists), measured on cameras that are focussed to the position of the atomic cloud. The T-waists are approximately 15 % larger than the other waists. Probably this is due to the different optical path length on the incoming beam side (40 cm distance between last lens and atoms).

axis	w_r / µm	w_z / µm
D	158	73
Y	153	71
X	161	70
T	184	91

Lattice angles

One of the limiting factors in observing very high momentum states is the angle between lattice beams. By fitting a straight line to diffraction peaks in time-of-flight the angle of each lattice beam with respect to the absorption image axes is determined. From these measurements (table 5.4) we conclude that the relative angles are 45(1)°.

Table 5.4: Relative lattice beam angles used in this work.

axes	angle
TD	89.5°
TX	45.6°
TY	44.0°
XY	91.6°
XD	46.2°
YD	45.4°

Control loops

The intensity of each lattice beam is actively stabilised using a PID feedback loop. Directly after the fibre and the optical isolator (which also acts as a polarisation-cleaning cube) a small ($\simeq$ 4%) proportion of the beam is directed to the 'PID-photodiode' using a wedged glass plate. This constitutes the feedback signal for the control loop, the active stabilisation being performed by the RF-power given to the AOM (before the fibre). The lattice pulse signals are created by waveform generators in order to have sub-µs time-resolution and high reproducibility of the DC voltages. In order to maximise the bandwidth of the control loops all cable lengths have been chosen to be as short as possible; the largest contribution comes from the cable connecting the PID-photodiode with the input of the PID-unit (12 m).

The active control loops have bandwidths on the order of several hundred kHz and consequently µs-risetimes of lattice pulses can be expected. The PID-parameters have been optimised for a given lattice depth ($15E_{\mathrm{rec}}$) such that a square pulse produces a maximal rise time (0% to 90% set voltage) of 1.1 µs, thereby minimising any overshoot. For different pulse shapes and lattice depths the parameters have to be re-optimised for best perfor-

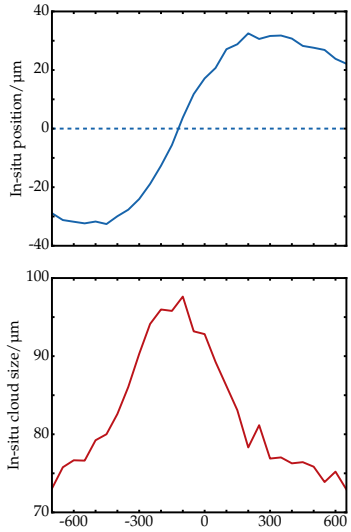

Figure 5.18: Lattice sliding method. The upper plot shows the in-situ position of the condensate on the Z-camera, at right angles to the lattice beam direction. The dashed line corresponds to the unshifted condensate position. The lower plot shows the same scan, but using the Thomas-Fermi radius of the cloud as observable. This data was taken using the horizontal knob of the D-axis piezo mirror.

[18] We showed in section 4.4 that the vertical position of the dipole beam can be discrimiated to within 2 um.

[19] The beam emerging from the fibre coupler (beam diameter roughly 1.2 mm) can never be perfectly collimated. Hence a 1:1 reproduction of beam waists at the position of the atoms is precluded by the laws of gaussian propagation.

mance; as usual, there is a trade-off between short rise times and minimal overshoot.

Setup and alignment

The precise alignment of the lattice beams is similarly critical as that of the dipole trap.[18] In brief, the following alignment steps should be observed.

- The focus of the incoming beam (beam waist) has to be overlapping with the atomic cloud. Similar to the dipole trap, the final achromat before the atoms is translated longitudinally (z-translation stage with µm-skrews) to minimise the beam waist. The beam waist can be measured with a dedicated camera on each lattice axis that has been focussed to the position of the atoms via in-situe absorption imaging. In the case of the X and Y axes, which are shared with the dipole trap, this alignment step is omitted since we trust the achromat to be already well-aligned having minimised the dipole trap waists. This assumes firstly that the focal shift due to the different wavelengths is minimal, and secondly, that the expected beam propagation of the lattice beam (using ABCD-matrices) is faithful. The latter point is assured by measuring the actual beam divergence after the fibre coupler for each individual lattice axis.

- The pointing of the lattice beam can be aligned via the so-called 'lattice sliding method'. It entails blocking the retro-path and shining a relatively weak lattice potential onto an atom cloud which is imaged in-situ along an axis that is at right angles to the lattice beam. Since our lattice is blue-detuned, the beam leads to a repulsive potential. If the lattice beam is off-centre in one direction, the atomic cloud is displaced towards the opposite direction. By taking a scan of vertical and horizontal displacement using a piezo-driven mirror, as shown in Fig. 5.18, the lattice beam can be centrally aligned to within a few µm. Note that due to the anti-symmetric response of the cloud, it is crucial to take an entire scan and find the symmetry point which corresponds to the optimum, i.e. unshifted position. In addition, the repulsive potential leads to a broadening of the atom cloud, providing an additional signature of good alignment (lower half of Fig. 5.18).

- On the retro-path, the transverse position of both lenses in the cats-eye configuration [201] is important in order to ensure good directional overlap between incoming and retro-reflected beam. This can be achieved by placing a pinhole on each lens mount and maximising the transmission. In addition, the longitudial position of the retro-mirror and the lenses is crucial to ensure approximately equal[19] beam waist of incoming and retro-reflected lattice beams. It should be noted that for elliptical beams, there are, in principle, no degrees of freedom in the longitudinal position of both the lenses and the retro-mirror,

because the cat's eye requires the distance between atoms and retro-mirror to be *exactly* twice the sum of the two focal lengths. The achromat on the atoms' side is assumed to be aligned to the in-situ position of the atoms via absorption imaging. The second cat's eye lens is placed in good faith by measuring the distances with a ruler.

- Finally, the directional pointing of the retro-reflected beam at the position of the atoms is relatively insensitive to the angle of the retro-mirror due to the cat's eye configuration. In particular, the diffraction angle (Kapitza-Dirac diffraction [202]) at the position of the atoms does not depend on the angle of the retro-mirror. Nevertheless, the angle can be optimised by maximising the effect of 1D Kapitza-Dirac diffraction.

6
Matter-wave diffraction experiment

This chapter presents the main experimental results of this thesis, namely the matter-wave diffraction experiments. Short lattice pulses (Kapitza-Dirac diffraction [202, 203]) are used to probe the 2D quasicrystalline structure in reciprocal space.

First, the basis of momentum in space of the 2D quasicrystal is described in section 6.1, building on the 1D results from section 5.1. Section 6.2 covers the experimental methods that are used (short lattice pulses). Afterwards, both the static and the dynamic diffraction patterns are described in theory and experiment. The diffraction dynamics, for very short pulses, are shown to represent quantum walks. Finally, our methods of data-analysis are detailed in section 6.5.

6.1 Basis in momentum space

Similar to the indexing method for diffraction pattern of 1D quasicrystals (section 1.2) we are going to write down a method to identify all basis states of the 2D quasicrystalline potential in momentum space using four integers. The basis states in momentum space correspond to the matter-wave diffraction peaks that are going to be observed in the experiment.

As before, the real-space potential of our optical lattice can be written as

$$V^D(\mathbf{r}) = V_0 \sum_{i=1}^{D} \cos^2\left(\frac{\mathbf{G}_i}{2} \cdot \mathbf{r}\right) \quad , \tag{6.1}$$

where $D = 1, 2, 3$, or 4 is the number of mutually incoherent lattice beams and $V_0 = 14.6(2)\, E_{\mathrm{rec}}$ is the individual lattice depth.[1] The reciprocal lattice vectors $\mathbf{G}_i$ are defined as

$$\mathbf{G}_1 = \begin{pmatrix} 1 \\ 0 \end{pmatrix}, \quad \mathbf{G}_2 = \begin{pmatrix} 0 \\ 1 \end{pmatrix}, \quad \mathbf{G}_3 = \frac{1}{\sqrt{2}} \begin{pmatrix} 1 \\ 1 \end{pmatrix}, \quad \mathbf{G}_4 = \frac{1}{\sqrt{2}} \begin{pmatrix} -1 \\ 1 \end{pmatrix} \tag{6.2}$$

where we have switched to dimensionless units in which $2k_{\mathrm{lat}} = 1$ as shown in Fig. 6.1 (right inset). In contrast to a periodic lattice the combination of several $\mathbf{G}_i$ here may give rise to new, smaller momentum scales, as shown the left inset of Fig. 6.1; for example, the combination $-\mathbf{G}_1 + \mathbf{G}_3 - \mathbf{G}_4$ results in a new k-vector (red arrow) that is shorter than the original $\mathbf{G}_1$ by a factor of $1 + \sqrt{2}$ (the silver mean). This process can be repeated ad infinitum and

[1] The lattice wavelength $\lambda_{\mathrm{lat}} = 2\pi/k_{\mathrm{lat}} = 726\,\mathrm{nm}$ is far detuned with respect to the D-lines in ^{39}K, ensuring that single-photon processes are completely suppressed. The value of E_{rec} is listed in table 5.1.

results in a self-similar structure containing arbitrarily small k-vectors, as indicated by the sequence of octagons in Fig. 6.1. Consequently, it is impossible to assign a maximum characteristic length to this quasicrystal, heralding the presence of structure on all scales. Furthermore, the momenta that are reachable from $\mathbf{k}_0 = (0,0)$ form a dense set in the k_x, k_y-plane and any element $\mathbf{G}$ of this set is determined by four integers $(i,j,l,n) \in \mathbb{Z}^4$ as

$$\mathbf{G} = i\mathbf{G}_1 + j\mathbf{G}_2 + l\mathbf{G}_3 + n\mathbf{G}_4 \quad . \tag{6.3}$$

While physical momentum remains two-dimensional, all four integers are nonetheless required to describe a given $\mathbf{G}$, since $\cos(45°) = \sin(45°) = 1/\sqrt{2}$ is irrational and hence incommensurable with unity. In fact, Fig. 6.1 can be viewed as an incommensurate projection of a 4D simple-cubic 'image' lattice to the 2D plane, similar to the 'cut-and-project' scheme for constructing the octagonal tiling (section 1.3). By using fewer than four lattice beams we can control the dimensionality of the image lattice and $\mathbb{Z}^4$ reduces to $\mathbb{Z}^D$ with $D \in \{1,2,3,4\}$.

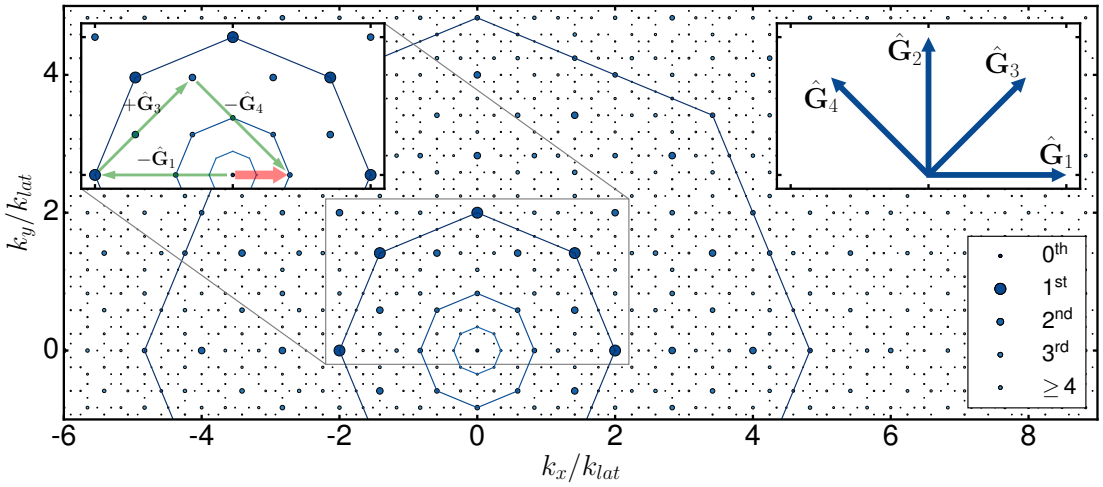

Figure 6.1: Momentum space structure. The first 15 orders of possible diffraction peaks are shown. They are constructed by iteratively adding or subtracting one of the four reciprocal lattice vectors $\mathbf{G}_i$ (inset on the right) to the peaks in the previous order, starting with $\mathbf{k} = (0,0)$. This results in a fractal structure, whose self-similarity is illustrated by a sequence of octagons, which are each scaled by the silver mean $1+\sqrt{2}$ relative to the next. The left inset shows one inflation step (see text).

Basis in momentum space

We can use Eq. 6.3 to express any accessible k-state as an integer-valued vector $\mathbf{b}_i$ in $\mathbb{Z}^D$, where D is the number of active lattice beams. As described for the 1D case in section 5.1 the nth order of this basis is defined as the set of all elements $\{\mathbf{b}_i\}$ with

$$\sum_{j=1}^{D} \mathrm{abs}\left([\mathbf{b}_i]_j\right) = n \tag{6.4}$$

where $[\mathbf{a}]_j$ denotes the jth component of a vector $\mathbf{a}$ and abs() denotes the absolute value. The total number of basis states N up to and including the n^{th} order for $D = 4$ is listed in table 6.1; it can

be written in a closed form as

$$N(n) = \sum_{k=0}^{\min(4,n)} 2^k \binom{4}{k}\binom{n}{k} \quad . \tag{6.5}$$

We will later truncate $\mathbb{Z}^D$ at the nth order, meaning we only take into account states that can be reached by at most n two-photon scattering events.

Table 6.1: Number of basis states up to and including the n^{th} order in the 4D case (eightfold lattice).

n	$N(n)$
0	1
1	9
2	41
3	129
4	321
5	681
...	
11	11969

The in table 6.1 are also known to be the coefficients of the Taylor expansion of the following function [204]

$$\frac{(1+x)^4}{(1-x)^5} \tag{6.6}$$

around $x = 0$.

Projection

For $D = 3$ and $D = 4$ the projection matrices for the states $\mathbf{b}_i$ onto the k_x, k_y–plane are given by

$$M_3 = \begin{pmatrix} 1 & 0 & \frac{1}{\sqrt{2}} \\ 0 & 1 & \frac{1}{\sqrt{2}} \\ 0 & 0 & 0 \end{pmatrix} \tag{6.7}$$

and

$$M_4 = \begin{pmatrix} 1 & 0 & \frac{1}{\sqrt{2}} & -\frac{1}{\sqrt{2}} \\ 0 & 1 & \frac{1}{\sqrt{2}} & \frac{1}{\sqrt{2}} \\ 0 & 0 & 0 & 0 \\ 0 & 0 & 0 & 0 \end{pmatrix}, \tag{6.8}$$

respectively. The third and fourth dimensions are projected to the in-plane diagonals with respect to the first two dimensions. The first two rows of M_3 and M_4 are simply given by the $\mathbf{G}_i$ defined in Eq. 6.2. Note the similarity of M_4 to the rotation matrix for the 4D cut-and-project scheme (Eq. 1.21 in section 1.3).

Fig. 6.1 shows elements of the basis of order 15 for $D = 4$, projected onto the k_x, k_y–plane using the matrix M_4. For $D = 1(2)$ the matrices $M_1(M_2)$ are trivial because here the dimension of $\mathbf{b}_i$ is the same as the physical dimension.

Hamiltonian in momentum space

Having constructed the basis we can write down the hamiltonian $\mathcal{H}^D$ in momentum space

$$\mathcal{H}^D_{i,j} = \begin{cases} V_0/4 & \text{for} \quad |\mathbf{b}_i - \mathbf{b}_j| = 1 \\ 4E_{\text{rec}} \times |M_D \cdot \mathbf{b}_i|^2 + V_0/2 & \text{for} \quad i = j \\ 0 & \text{otherwise} \end{cases} \tag{6.9}$$

Here the norm of a D-dimensional vector $\mathbf{a}$ is given by

$$|\mathbf{a}| = \sqrt{\sum_{j=1}^{D} \left([a]_j\right)^2} \quad . \tag{6.10}$$

The non-zero off-diagonal elements correspond to transition elements for stimulated two-photon scattering events, where atoms scatter photons from one lattice beam into its counterpropagating partner. These transitions connect discrete momentum states separated by $\pm\mathbf{G}_i$ and effectively realise a tight-binding hamiltonian

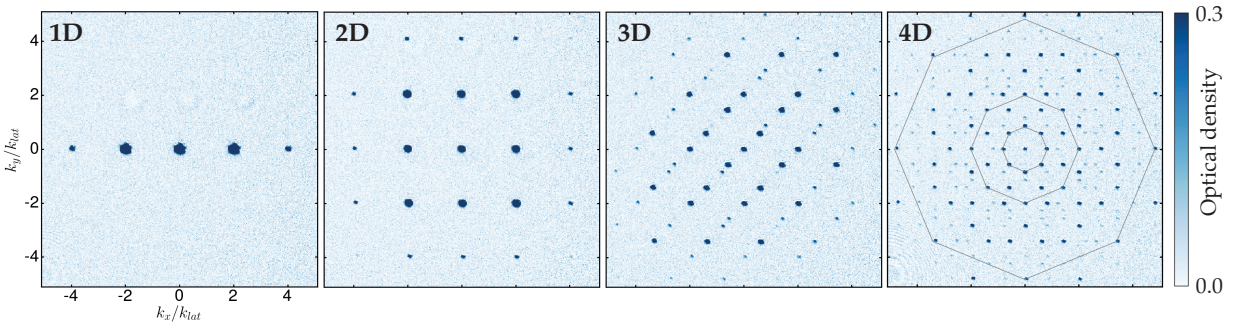

Figure 6.2: Raw time-of-flight images of ^{39}K resulting from four different lattice configurations at fixed lattice pulse duration ($t = 3.5\,\mu$s). Using just one of the lattice axes results in a regular 1D simple-cubic lattice characterized by $\mathbf{G}_1$; adding the perpendicular lattice creates a regular 2D square lattice with $\mathbf{G}_1$ and $\mathbf{G}_2$. By adding the first diagonal lattice we obtain a lattice of 1D quasiperiodic potentials with dense sets of momentum states along $\mathbf{G}_3$ whereas the direction perpendicular to $\mathbf{G}_3$ remains regular (labelled 3D). Finally, using all four axes we create the 2D quasicrystal (labelled 4D); its self-similarity is illustrated by the octagons.

in momentum space [205]. The matrix elements on the diagonal are given by the kinetic energy term, where the prefactor $2^2 E_{\text{rec}}$ arises from the momentum scale $2\hbar k_{\text{lat}}$ of the individual lattices and a constant offset of $V_0/2$ which arises from the $k = 0$ Fourier component of $V^D(\mathbf{r})$ (it has no physical significance since it corresponds to a global shift in energy).

Truncation of basis

As in the 1D case (Eq. 5.10), this hamiltonian is infinite-dimensional and, consequently, we need to make it numerically tractable by truncating it. Since the experiment starts with a pure condensate in the $|\hbar\mathbf{k} = 0\rangle$ state, and we apply only short pulses of lattice light, it is sensible to work with a basis of order $n = 11$. This can be justified a posteriori since even for the longest applied lattice pulses our simulation (using a basis of order 15) shows that the orders $n > 11$ get populated by less than 15 per cent. As before, the time-evolution can be calculated by numerically integrating the time-dependent Schrödinger equation. This is achieved by writing the hamiltonian matrix $\mathcal{H}^D_{i,j}$ in the truncated momentum basis; integration is performed using the `scipy.integrate` library.

6.2 *Method: Kapitza-Dirac diffration*

The experimental sequence starts with the preparation of an almost pure Bose-Einstein condensate of ^{39}K atoms in a crossed-beam dipole trap, as described in Chapters 3 and 4. Using the Feshbach resonance centred at 402.70(3) G (section 4.6) we tune the contact interaction to zero just before we release the condensate from the trap. Then we immediately expose it to the optical lattice for a rectangular pulse of duration t. During this pulse, atoms in the condensate can undergo several stimulated two-photon scattering events (Kapitza-Dirac scattering [206]), which scatter photons from one lattice beam into its counterpropagating partner and transfer quantized momenta of $\pm 2\hbar k_{\text{lat}}$, where $\hbar k_{\text{lat}}$ is the momentum of a lattice photon and $|\mathbf{G}_i| = 2k_{\text{lat}}$. Throughout

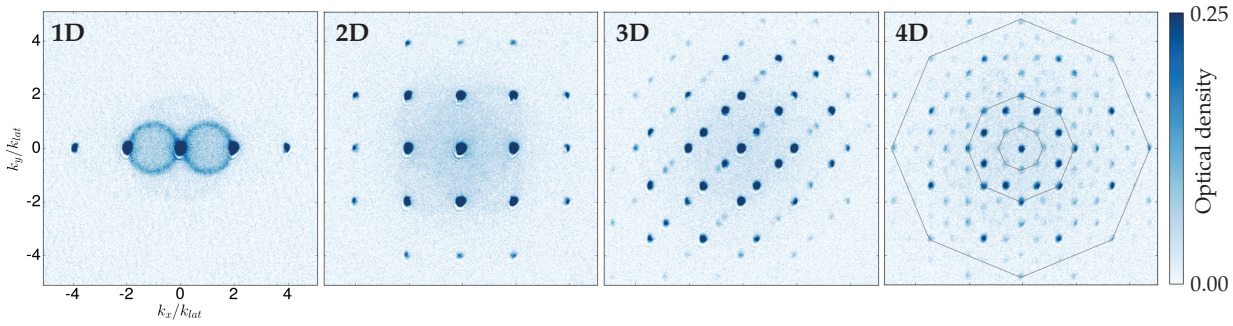

Figure 6.3: Raw time-of-flight images of ^{87}Rb resulting from four different lattice configurations at fixed lattice pulse duration ($t = 5.0\,\mu$s). Compared to Fig. 6.2, which was taken with ^{39}K, the resolution in momentum space is worse. In addition, strongly pronounced 'scattering shells' (see text) appear for ^{87}Rb (scattering length $a = 100\,a_0$) which lead to a diffuse background in the 4D situation.

this chapter, the lattice depth of each individual axis is $14.6(2)E_{\mathrm{rec}}$. Finally, we record the momentum distribution of the atomic cloud by taking an absorption image after $t_{\mathrm{ToF}} = 33\,\mathrm{ms}$ (time-of-flight).

In a first experiment we fix the lattice pulse duration at $t = 3.5\,\mu$s and vary the number of lattice beams, as shown in Fig. 6.2. Starting from the single-axis (1D) case, we subsequently add lattice axes, finally completing the eightfold symmetric case (4D), representing the quasicrystalline structure with its striking self-similarity under $(1+\sqrt{2})$ scaling.

Interaction effects

For diffraction experiments that are carried out with finite contact interactions (e.g. using ^{87}Rb, Fig. 6.3) one finds that the time-of-flight images feature pronounced 'scattering shells' [207, 208] connecting the discrete momentum peaks. These shells appear as characteristic rings on the absorption images and arise from two-body s-wave collisions between parts of the atomic cloud which are moving with respect to each other. In order to eliminate this effect we perform all experiments with ^{39}K and tune the contact interaction to zero by ramping the magnetic field to a value of $351.5(1)\,\mathrm{G}$, just before the optical lattice pulse is applied. However, atomic clouds of ^{39}K at vanishing interactions are optically dense enough to absorb essentially all imaging light, preventing any faithful atom number measurement. Therefore we turn interactions back on (back to the previous value of roughly $280\,a_0$) once the diffraction orders have separated from each other, such that the individual peaks expand and reveal their atom populations.

6.3 *Diffraction dynamics*

The diffraction dynamics offers one of the most striking signature of the aperiodicity of the eightfold optical lattice. During the lattice pulse the condensate explores reciprocal space in discrete steps of $\pm\mathbf{G}_i$, leading to profoundly distinct behaviours in the periodic (2D) and in the quasicrystalline case (4D). Fig. 6.4 shows absorption images for four different values of pulse duration t in

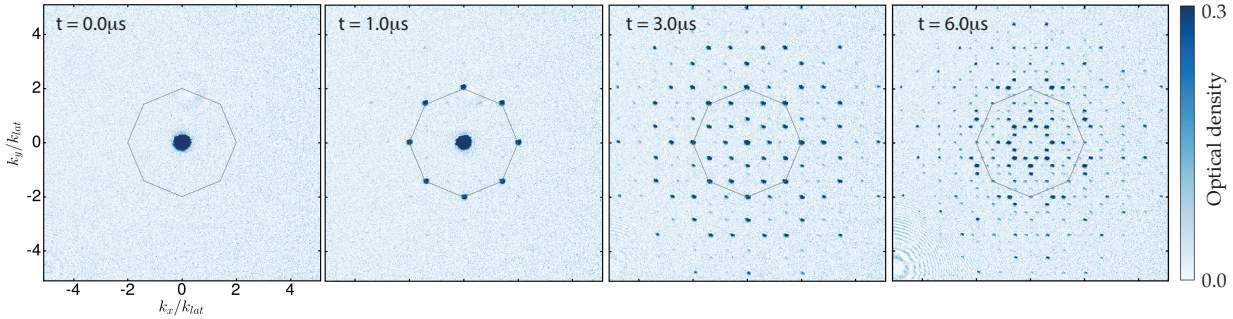

Figure 6.4: Dynamics of Kapitza-Dirac diffraction in the quasicrystalline optical lattice. The figure shows raw absorption images for four different lattice pulse durations. After 1μs, only the first diffraction order has been populated, while longer pulses lead to populations in successively higher orders as the atoms perform a quantum walk in momentum space. Each octagon has a circumradius of $|\mathbf{G}_i| = 2k_{\text{lat}}$, illustrating the fundamental momentum scale due to two-photon processes.

the latter configuration, illustrating the occupation of more and more closely spaced momenta. Using individual fits we extract the number of atoms in every k-state up to the seventh diffraction order, i.e. those momenta reachable by seven or fewer two-photon scattering events. In the 2D simple cubic lattice (Fig. 6.5 on the left) only a few momentum states are accessible, since kinetic energy acts as a harmonic confinement in momentum space. Therefore the dynamics is oscillatory and reminiscent of a simple harmonic oscillator. In the quasicrystalline case, in contrast, the diffraction dynamics is aperiodic (4D, right of Fig. 6.5), since large parts of the population propagate ballistically to progressively higher orders, as illustrated by the light blue 'wave front'. Due to the self-similar momentum space structure, the atoms can access momentum states in successively higher diffraction orders

Figure 6.5: Kapitza-Dirac diffraction dynamics in a periodic (2D) and quasicrystalline (4D) lattice. The normalized populations (coloured dots) of the condensate (0^{th} order) and the first seven diffraction orders are plotted against pulse duration, together with the numerical solution to the Schrödinger equation (lines). The periodic case (2D) is oscillatory as kinetic energy limits the accessible momenta. In contrast, the quasicrystalline lattice (4D) contains a dense set of k-states, c.f. Fig.6.1, enabling the population of higher and higher orders. Correspondingly, the expansion carries on linearly, indicated by the light blue 'wave front' as a guide to the eye. Error bars denote the standard deviations from five realisations of the experiment, and are typically smaller than symbol size.

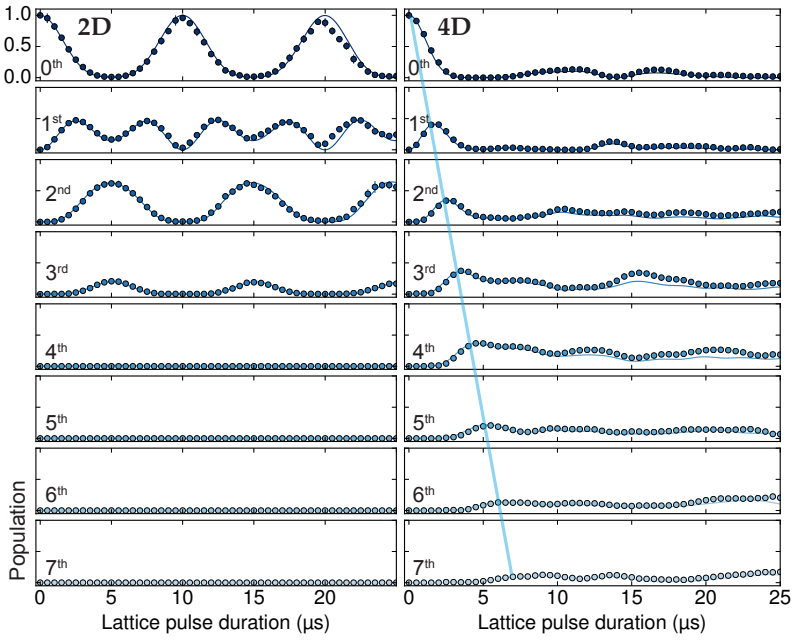

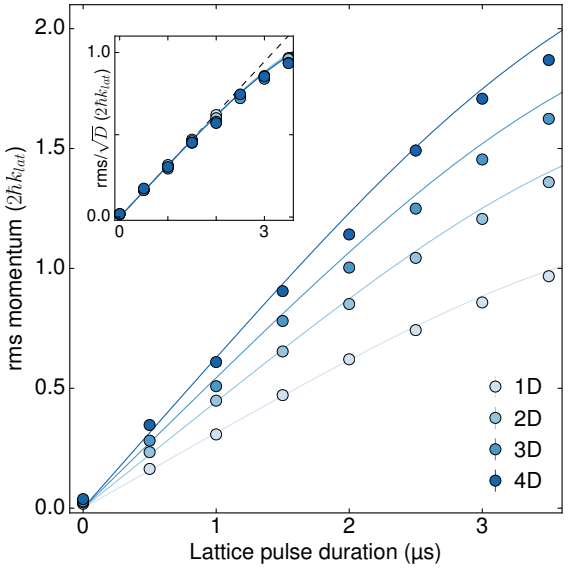

Figure 6.6: Continuous-time quantum walk in momentum space in D dimensions, where D is controlled by the number of lattice beams. Dots represent the measured root-mean-square momentum (see text), while lines represent numerical solutions to the full Schrödinger equation. The inset shows the same data, but scaled by $\sqrt{D}$. Here the dashed line represents the expansion dynamics of a continuous-time quantum walk on a homogeneous D-dimensional tight-binding lattice. The $\sqrt{D}$ scaling (Eq. 5.17) is a direct consequence of the separability of hypercubic lattices. Deviations from the linear behaviour at later times are due to kinetic energy, and the lines would differ from each other at long times. Error bars denote standard deviations from five identical realisations of the experiment.

that correspond to ever smaller momenta. Our data agrees excellently with exact numerical solutions (lines in Fig. 6.5) of the single-particle time-dependent Schrödinger equation in momentum basis.

6.4 *Quantum walks in high-dimensional homogeneous tight-binding lattices*

In the regime of very short pulses kinetic energy can be neglected for all dimensions and the discrete momentum space structure can be mapped onto a homogeneous tight-binding lattice [205]. A hopping event in this effective lattice corresponds to a two-photon scattering event and connects momenta differing by $\pm\hbar\mathbf{G}_i$. In this mapping, the diffraction dynamics is equivalent to the expansion of initially localised particles and gives rise to a continuous-time quantum walk with its characteristic light-cone-like propagation [22, 190, 191]. For a hypercubic lattice in D dimensions, the separability of the tight-binding dispersion relation (section 5.1) leads to an average group velocity proportional to $\sqrt{D}$ (Eq. 5.17). Due to the correspondence between the number of lattice beams and the dimension of the tight-binding hamiltonian, we are able to extend the dynamics to up to four dimensions. Using the appropriate form of Eq. 6.3 in $\mathbb{Z}^D$, we extract the effective root-mean-square momentum in D dimensions, e.g. $\sqrt{\langle i^2 + j^2\rangle}$ in the 2D case and $\sqrt{\langle i^2 + j^2 + l^2 + n^2\rangle}$ in the 4D case, from the individual populations of all diffraction peaks, and find excellent agreement between the measurements and the analytic result $v_p \propto \sqrt{D}$, as shown in Fig. 6.6. The departure from linear behaviour at longer times is due to kinetic energy and is captured well by the exact numerical solution to the Schrödinger equation (solid lines in

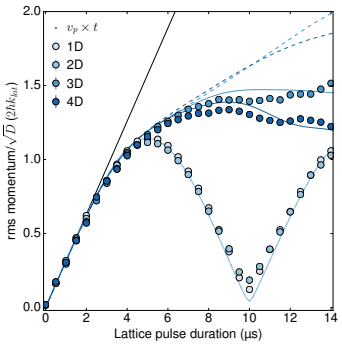

Figure 6.7: Root-mean-square momentum for longer times, scaled by a factor $\sqrt{D}$ as in Fig. 6.6 (inset) in the main text. The dashed black line is the analytic result (Eq. 5.17) in a D-dimensional homogeneous tight-binding model. The dashed blue lines are the solutions to the time-dependent Schrödinger equation, using all states with $n \leq 11$. If we take into account that we only detect atoms up the seventh diffraction order, the expansion is reduced to slightly lower momentum values (solid lines).

Fig. 6.6). The extent of the linear region is controlled by the lattice depth. For even longer times, kinetic energy enforces fundamentally different behaviours for periodic and quasicrystalline lattices, as shown in Fig. 6.5 (and in Fig. 6.7).

6.5 Data analysis

The data analysis procedure for determining the population in each diffraction peak is described in the following. First, we determine the position of the condensate, find the angle of one lattice axis relative to the camera axes, and calibrate the magnification using reference images showing only zeroth and first order diffraction peaks. With this information we can calculate the expected position of each momentum peak. Around each calculated peak position we perform an individual fit to a 2D Thomas-Fermi profile (Eq. 4.14) in a square bin of 28×28 pixels (56×56 for the central condensate). In order to mitigate effects of imaging saturation, the fit ignores pixels with optical densities above 2.0. The corresponding atom population of each basis element $p_i(t)$ is proportional to the integrated Thomas-Fermi profile, the result of which is in Fig. 6.8 as an example. If the population $p_i(t)$ is below 0.04% of the total population we ignore it in order to avoid counting spurious populations in high diffraction orders, which would otherwise dominate the rms. For Fig. 6.5 we sum all populations in one diffraction order.

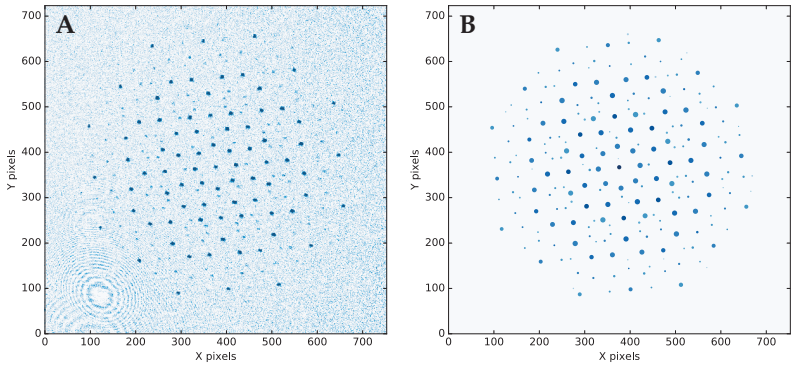

Figure 6.8: Simplified example of the population count. (**A**) The raw absorption image ($D = 4, t = 3\mu$s). At each calculated peak position with $n \leq 7$ we perform an individual fit to a 2D Thomas-Fermi profile. The resulting populations $p_i(t)$ are depicted in (**B**) by the area of the circles.

Root-mean-square extraction

We calculate the root-mean-square momentum in D dimensions as a function of time as

$$\sqrt{\sum_i \frac{p_i(t)}{\sum_j p_j(t)} |\mathbf{b}_i|^2} \quad , \tag{6.11}$$

where $p_i(t)$ are the populations in each diffraction peak $\mathbf{b}_i$ at a given time t. The sums go over all elements of a basis.

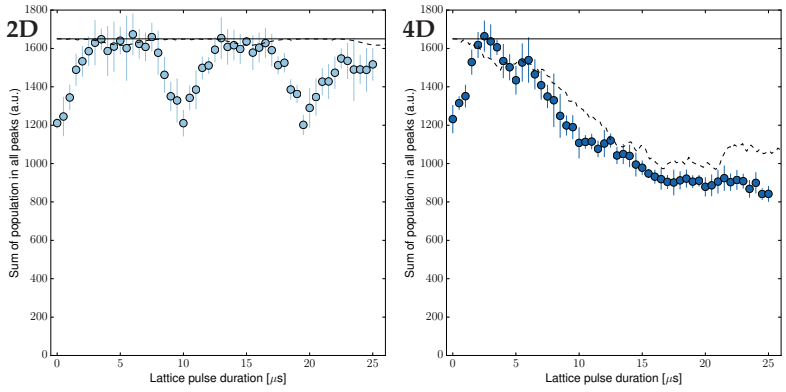

Figure 6.9: Total detected population (a.u.) in all diffraction peaks for the 2D and 4D situations. The solid black lines correspond to the total population and the dashed lines are the simulated populations in peaks up to seventh order and additionally account for peaks that fall below the cutoff. When single peaks (such as the central condensate) are strongly populated we systematically detect too few atoms due to imaging saturation and the finite signal-to-noise ratio of the camera. This effect is reflected by the apparent rise in total detected population during the first few μs. It also explains the subsequent 'dips' in atom number in the 2D case.

Total population

Figure 6.9 shows the total detected population $\sum_j p_j(t)$ summed over all diffraction peaks for the cases $D = 2, 4$. For $D > 2$, the detected population is reduced for longer lattice pulses since more and more peaks are weakly populated and fall below the cutoff. In addition, we underestimate the population of very highly populated peaks, such as the initial condensate, due to the finite signal-to-noise of the camera.

Conclusion

In conclusion, a quasicrystalline potential for ultracold atoms was realised, which can facilitate the creation of ever more complex many-body systems [31]. By observing the occupation of successively closer-spaced momenta, we were able to confirm its self-similar structure in momentum space. In addition, the fundamentally different diffraction dynamics between periodic and quasicrystalline potentials have been verified, in excellent agreement with theory. Finally, we demonstrated the ability to simulate tight-binding models in one to four dimensions, by observing the ballistic spreading of particles in reciprocal space.

Summary and outlook

In summary, this thesis establishes quasicrystalline potentials as a novel platform for ultracold atoms. The eightfold optical lattice is a highly versatile system, allowing investigation of a large variety of lattice potentials. These include several 1D and 2D periodic geometries, 1D quasiperiodic lattices, and 2D quasiperiodic potentials, both separable and non-separable. This work represents the first demonstration of a non-separable, 2D quasicrystalline lattice for ultracold atoms, thereby bringing closer the fields of quasicrystals and ultracold atoms.

The focus of this thesis has been on the experimental realisation of above mentioned platform. Experimental details have been given on initial laser cooling (Chapter 3), the production of quantum gases (Chapter 4), and the setup and characterisation of the eightfold optical lattice (Chapter 5).

In a series of proof-of-principle experiments, two important properties of 2D quasicrystals, namely self-similarity and the connection to higher dimensions, have been demonstrated with ultracold atoms for the first time. These include the direct observation of a quantum walk on a homogeneous tight-binding model in four dimensions.

Next steps

Having established the eightfold lattice potential, there are many interesting steps to be taken from here.

Adiabatic loading

So far, all the experiments described in this thesis have been probing the quasicrystal in momentum space, using transient pulses of laser light. The next obvious step would be to study the system in equilibrium (if this is possible) and load atoms into the potential for longer times. Here, one of the main challenges will be understanding adiabaticity in this aperiodic potential. Preliminary studies show that, for small lattice depths ($V_0 \lesssim 1.5 E_{\mathrm{rec}}$), adiabatic loading of the lattice should indeed be possible. This can be seen by considering triangular lattice pulses as shown in Fig. 6.10. After ramping up the eightfold lattice to a certain value V_0 and subsequently ramping it back down, the fraction of atoms remaining in the condensate (0^{th} diffraction order) is a signature

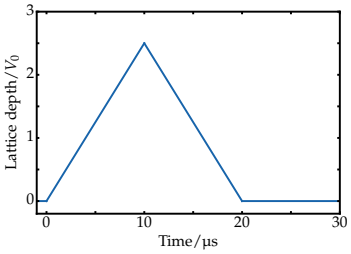

Figure 6.10: Triangular lattice pulse shape, duration 20 μs, lattice depth $2.5\,E_{\mathrm{rec}}$.

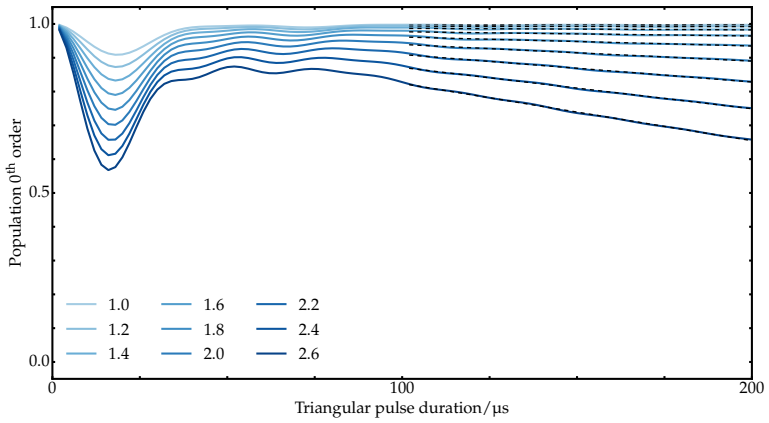

Figure 6.11: Theoretical final population in 0^{th} diffraction order after triangular pulse of duration t (x-axis) for various lattice depths V_0 in the eightfold optical lattice. After an initial dip, the condensate fraction (0^{th} order) recovers to almost unity for shallow lattice depths (light blues). For higher depths (deep blues), the long-term behaviour shows no recovery of the 0^{th} order, which can be interpreted as non-adiabaticity on these timescales. For $t > 100$ µs the curves have been fitted with linear functions, the slopes of which are shown in Fig. 6.12.

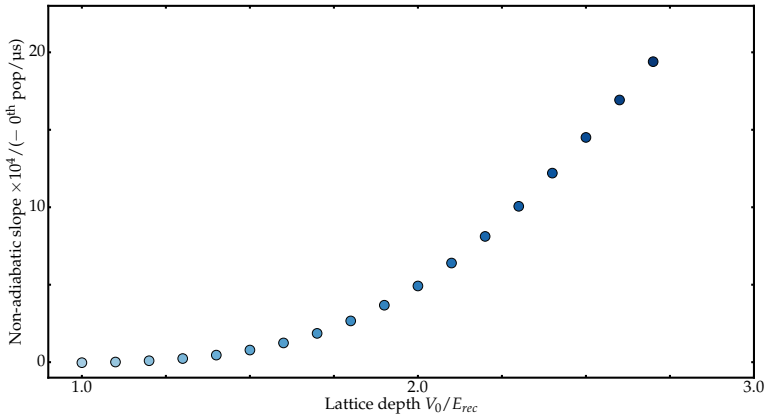

Figure 6.12: Slopes from Fig. 6.11, plotted against lattice depth. Non-zero slopes start to appear above $1.5\,E_{\mathrm{rec}}$ heralding non-adiabatic behaviour.

of adiabaticity [209].

This has been theoretically investigated in Fig. 6.11 for the full eightfold lattice potential (solutions to time-dependent Schrödinger equation). For shallow lattices (faint blues) adiabaticy can be achieved, even in the aperiodic lattice. However, lattice depths higher than $\simeq 1.5E_{\mathrm{rec}}$ (deep blues) show a non-zero slope for longer lattice pulse durations, heralding non-adiabatic behaviour. The slopes have been fitted for $t > 100$ µs as a quantitative estimate of adiabaticity and they show a cross-over behaviour from adiabadic to non-adiabatic (Fig. 6.12).

Experimentally, this behaviour will be very interesting to investigate, in particular as a function of interaction strength.

Topology

One of the great achievements in the field of quantum gases has been the experimental realisation of topologically non-trivial systems [210–212]. In future, aperiodic lattices may find an application in this context. For example, a topological charge pump has been demonstrated experimentally using a 1D photonic quasicrystal [5]. It would be worth pursuing further studies along this

direction in quantum gas systems, particularly in the light of the recent observation of a 4D quantum Hall response in tilted optical superlattices [86].

Many-body localisation

Another application of aperiodic lattices for ultracold atoms has been the observation of many-body localisation [88]. In particular the role of interactions in quasiperiodic media is still poses fundamental open questions in physics [89], and experimental results have only recently become available [24, 88, 90, 91]. So far, all experiments employed either 1D [88, 90, 91] or 2D separable [24] potentials. However, more experimental evidence is needed, for instance, to differentiate between two universality classes of localisation phenomena, namely in random disorder and in aperiodic order [92]. For the latter class, our experiment is an ideal starting point since the lattice potential closely resembles the octagonal tiling (see section 5.3), a paradigmatic 2D quasicrystal.

Moreover, our system will be able to investigate the fate of a Mott-insulator in the presence of a weak aperiodic perturbation in two dimensions. In one dimension, there has been evidence of a Bose-glass phase [213, 214], but the two-dimensional case has not been experimentally investigated so far.

More ideas

In the four-beam lattice the total number of basis states grows very fast with the diffraction order (table 6.1). For example, a basis of order eleven contains almost 12000 states. Therefore it would be interesting to reduce the atom number in the diffraction experiment by some orders of magnitude until it becomes comparable to the number of basis states. Will the discreteness of the population then show in the diffraction dynamics?

A
List of components

Near-resonant laser system ('red table')

	identifier	description	part number	manufacturer
Lasers	K master TA	766.7 nm, 2.0 W, 760-775 nm coarse tuning, 50 GHz mode-hop-free	TA pro 765-3V0	Toptica Photonics AG
	Rb master TA	780.24 nm, 3.0 W, 770-795 nm coarse tuning, 50 GHz mode-hop-free	TA pro 780-3V0	Toptica Photonics AG
	K imaging	766.7 nm, 80 mW	DL pro	Toptica Photonics AG
	Rb repump	780.24 nm, 100 mW, 765-805 nm coarse tuning, 30 GHz mode-hop-free	DL pro 780-3V0	Toptica Photonics AG
	K red loading	767 nm, 2.0 W	BoosTA pro 765-1V0	Toptica Photonics AG
	K blue loading	767 nm, 2.0 W	BoosTA pro 765-1V0	Toptica Photonics AG
	K red MOT	767 nm, 2.0 W	BoosTA pro 765-1V0	Toptica Photonics AG
	K blue MOT	767 nm, 2.0 W	BoosTA pro 765-1V0	Toptica Photonics AG
	Rb loading MOT	780 nm, 3.0 W	BoosTA pro 780-1V0	Toptica Photonics AG
	Rb cooling	780 nm, 3.0 W	BoosTA pro 780-1V0	Toptica Photonics AG
	Rb 780/repump	780 nm, 3.0 W	BoosTA pro 780-1V0	Toptica Photonics AG
Optics	M45	Laser mirror HR 630-900 nm/0-45° s+p, R>99.6%	HR 630-900 nm	Lens-Optics GmbH
	W2	$\lambda/2$ 0^{th} order wave plate	W2Z15-773	Lens-Optics GmbH
	W4	$\lambda/4$ 0^{th} order wave plate	W4Z15-773	Lens-Optics GmbH
	magic-W	$\lambda/2$ at 780 nm and λ at 767 nm 0^{th} order wave plate	W2Z15-L/2@780&L@767	Lens-Optics GmbH
	PBS	1/2 inch polarising beam splitter	PBC12-600/900	Lens-Optics GmbH
	BS50	Non-polarising beam splitter 50:50	BS005	Thorlabs, Inc
	F15	Fibre coupler, $f = 15$ mm APC, 600-1050 nm (used for TA beams)	60FC-4-M15-02	Schäfter-Kirchhoff GmbH
	F15-A	Fibre coupler, $f = 15$ mm APC, 750-1550 nm (used for TA beams)	60FC-4-M15-37	Schäfter-Kirchhoff GmbH
	F8	Fibre coupler, $f = 8.1$ mm APC, 630-980 nm (for all other beams)	60FC-4-M8-10	Schäfter-Kirchhoff GmbH
	WW30	Glass plate beam spliter, fused silica, 30 min of arc, $\lambda/10$ quality	WW1Q	Lens-Optics GmbH
AOMs	80	AOM 80(30) MHz, 700-1100 nm, 1×2 mm^2 active aperture, >2 W RF	MT80-B30A1-IR	AA opto-electronic
	110	AOM 110(50) MHz, 700-1100 nm, 1×2 mm^2 active aperture, >2 W RF	MT110-B50A1-IR	AA opto-electronic
	200	AOM 200(50) MHz, 700-900 nm, 1×2 mm^2 active aperture, >2 W RF	MT200-B50A1-800	AA opto-electronic
Other	Optical fibres	Single-mode polarisation-maintaining fibres	P3-630PM-FC	Thorlabs, Inc
	CoSy K	Fibre-coupled spectroscopy	CoSy	TEM Messtechnik AG
	CoSy Rb	Fibre-coupled spectroscopy	CoSy	TEM Messtechnik AG

Vacuum

part	description	part number	manufacturer
Vacuum chamber	Custom, mostly 316LN (MOT, 20 cm diff. pumping section ⌀ 10 mm, 2 TSPs, knee)	-	PiNK GmbH
Small ion pump	Vacion plus 75 l/s starcell pump	9191440	Agilent Technologies LDA
Large ion pump	Vacion plus 150 l/s starcell pump with installed heaters 220V	9191542	Agilent Technologies LDA
Titanium sublimation pump	TSP filament cartridge	9160050	Agilent Technologies LDA
DN16CF bellow	Bellow between 2D MOT and 3D MOT	MEW0750251C1	Kurt J. Lesker
DN16CF straight valve	Valve between 2D MOT and 3D MOT	48124-CE01-0001	VAT Vacuum Products Ltd
DN16CF angled valve	Valve for potassium and rubidium ampoules	54124-GE02-0001	VAT Vacuum Products Ltd
DN40CF angled valve (high-T)	Angled valve for high-temperature bakeout section (near science cell)	57132-GE02-0005	VAT Vacuum Products Ltd
DN40CF angled valve (low-T)	Angled valve for low-temperature bakeout (all others)	54132-GE02-0001	VAT Vacuum Products Ltd
Lowest-pressure gauge	Pressure gauge for science cell section	Barion-extended	Vacom GmbH
Standard gauge	Pressure gauge for MOT chamber and turbopump	BAT40C	Vacom GmbH
Non-magnetic viewport	DN40CF 316LN steel, viewport used near science cell, BBAR coating 550-1100 nm	XTEMP-FT	Kurt J. Lesker
Standard viewport	DN40CF, BBAR coated (two parts broke under vacuum in 2D MOT)	VPZL-275BBAR	Kurt J. Lesker
Non-magnetic viewport	DN40CF BBAR coated, replacement for above	VPCF40DUVQ-L-BBAR-316L	Vacom GmbH

MOT setup

	part	description	part number	manufacturer
2D MOT	Vacuum chamber	Titanium (grade 2) frame and diff. pumping section (custom made, partly faulty)	S2-CF-5045/5044	Vaqtex S.r.l.
	Window	BK7 optical window, 85 mm × 50 mm, thickness 10 mm, AR 760-790 nm	PL.OF.85.50.760	Pegasus Lasersysteme GmbH
	Polariser	25.0 mm ⌀ linear glass polariser 510-800 nm	LPVISC100	Thorlabs, Inc
	Large $\lambda/4$	Mico retarder $\lambda/4$ wave plate, 70 mm × 35 mm, 780/767 nm	RQM7035-C/RQM7036-C	Knight optical Ltd
MOT	Fibre cluster	2 to 6 port fibre cluster, 767 nm and 780 nm, incl. single-mode fibres and couplers	-	Schäfter + Kirchhoff GmbH
	$\lambda/4$ wave plate	Polymer $\lambda/4$ wave plate (custom made)	WPQ10E-773-SP	Thorlabs, Inc
Fluorescence setup	Rb filter	Laser line filter for 780 nm	FL05780-10	Thorlabs, Inc
	K filter	Laser line filter for 766 nm	65-116	Edmund optics

Dipole trap laser system

part	description	part number	manufacturer
Laser	1064 nm, 55 W, master diode and four integrated amplifiers	Mephisto MOPA 55 W	Coherent Inc
Water-water chiller	1000 W at 20°C (operating) and 15°C (house), 5.6 l/min	P201-16675-WW-S	Termotek AG
Coolant	Cooling mixture P/N 1607-0546L	Nalco® CCL100	Nalco
Optical isolator	1064 nm free-space isolator	IO-5-1064-HP	Thorlabs, Inc
Mirror (M45-1064)	High-power mirror, 45° s+p R> 99.6%, 500 kW/cm^2	M1064	Lens-Optics GmbH
Wave plate (W2-1064)	$\lambda/2$ 0$^{\text{th}}$ order wave plate	W2Z15-1064	Lens-Optics GmbH
Cube (PBS-1064)	1/2 inch polarising beam splitter	PBC12-1064 HP	Lens-Optics GmbH
AOM	80 MHz, 1064 nm, 1×2 mm active aperture, >2 W RF	MT80-A1-1064	AA opto-electronic
Fibre	Photonic crystal fibre, SMA connector, 5 m, E324-443-500	aeroGUIDE POWER-15-PM	NKT photonics A/S
Fibre coupling lens	$f = 18.40$ mm, mounted geltech aspheric lens, AR 1050-1700 nm	C280TMD-C	Thorlabs, Inc
Polariser	Glan-Laser polariser, 10 mm diameter CA, 1064 nm V-coating	GL10-C26	Thorlabs, Inc
Photodiode	InGaAs amplified detector 900-1700 nm	PDA10CS-EC	Thorlabs, Inc
Cylindrical lens	$f = -30$ mm, C-coating 1050-1700 nm	LK1982L1-C	Thorlabs, Inc
Cylindrical lens	$f = 150$ mm, C-coating 1050-1700 nm	LJ1934L1-C	Thorlabs, Inc
Lens	$f = -100$ mm, C-coating 1050-1700 nm	LC1120-C	Thorlabs, Inc
Lens	$f = 125$ mm, C-coating 1050-1700 nm	LA1986-C	Thorlabs, Inc
Piezo mirror mount	1 inch, Picomotor™ piezo clear edge center mount, 2-axis	8821	Newport Spectra-Physics Ltd

Lattice laser system

part	description	part number	manufacturer
Pump laser	532 nm, 25 W, frequency-doubled laser	Millennia EV20S	Spectra-Physics (Newport)
Ti:Sapph laser	700-790 nm, 5.5-8.0 W (in this wavelength range, at 25 W pump)	Matisse 2 TS	Sirah Lasertechnik GmbH
Water/air chiller	Chiller used for Millennia and Ti:Sapph crystal, typ. 20.0°C, 20 psi	6000 Series	PolyScience
Coolant	Cooling mixture P/N 1607-0546L	Nalco® CCL100	Nalco
Mirror (M45)	Laser mirror HR 630-900 nm/0-45° s+p, R>99.6%	HR 630-900 nm	Lens-Optics GmbH
Wave plate (W2-730)	$\lambda/2$ 0$^{\text{th}}$ order wave plate	W2Z15-730/W2Z24-730	Lens-Optics GmbH
Cube (PBS HP)	1/2 inch polarising beam splitter	PBC12-730-HP	Lens-Optics GmbH
Optical isolator	Linos Faraday isolator	FI-730-5SV	Qioptiq Photonics GmbH & Co KG
AOM	110 MHz, 700-1100 nm, 1×2 mm^2 active aperture, >2 W RF	MT110-A1-IR	AA opto-electronic
Fibre	FC/APC to FC/PC connector (custom-made)	TS1754306-PM630-HP	Thorlabs, Inc
Fibre coupler (F8)	$f = 8.1$ mm APC, 630-980 nm (fibre in-coupling)	60FC-4-M8-10	Schäfter-Kirchhoff GmbH
Fibre coupler (FP5)	$f = 5.1$ mm PC, 630-980 nm (fibre out-coupling DYX axes)	60FC-0-M5-10	Schäfter-Kirchhoff GmbH
Fibre coupler (FP15)	$f = 15$ mm PC, 600-1050 nm (fibre out-coupling T axis)	60FC-0-M15-02	Schäfter-Kirchhoff GmbH
Photodiode	Si amplified detector, 350-1100 nm	PDA36A-EC	Thorlabs, Inc
Cylindrical lens (L -40 cyl)	$f = -40$ mm, N-BK7 B-coated cylindrical lens	LK1283L1-B	Thorlabs, Inc
Cylindrical lens (L 100 cyl)	$f = 100$ mm, N-BK7 B-coated cylindrical lens	LJ1567L1-B	Thorlabs, Inc
Achromat (LA100)	1 inch, $f = 100$ mm, B-coated achromatic lens (DT axes)	AC254-100-B	Thorlabs, Inc
Achromat (LA125)	1 inch, $f = 125$ mm, B-coated achromatic lens (YX axes, shared with dipole)	AC254-125-B	Thorlabs, Inc
Achromat (LA400)	1 inch, $f = 400$ mm, B-coated achromatic lens (T axis)	AC254-400-B	Thorlabs, Inc
Achromats (LA XX)	1 inch, $f =$XX mm, B-coated achromatic lens (telescopes)	AC254-XX-B	Thorlabs, Inc
Piezo mirror mount	1 inch, Picomotor™ piezo clear edge center mount, 2-axis	8821	Newport Spectra-Physics Ltd.
Dichroic mirror (M-DICH)	40 mm ⌀, HR725-780 nm HT1064 nm/45° (used on YX axes to split off dipole)	B-14749/B-14687 S-00929	Laseroptik GmbH (Garbsen)

Miscellaneous

	part	description	part number	manufacturer
Cameras	Andor Zyla	Z axis camera, sCMOS 6.5 µm pixel size, 0.5° wedged window, 780 nm	ZYLA-5.5-USB3-9WT	Andor Technologies
	Manta	Imaging on D axis, CMOS 5.86 µm pixel size, Gigabit Ethernet	AV Manta G-235B POE RCG	Allied Vision/Stemmer Imaging
	IDS uEye	Imaging on YXT axes, MOT fluorescence, CMOS 4.5 µm pixel size, USB2.0, global shutter	UI-1252LE-M	IDS Imaging Development Systems GmbH
	Beam cam	Beam profiling applications, CMOS 4.5 µm pixel size, USB2.0, rolling shutter	UI-1542-LE-M	IDS Imaging Development Systems GmbH
Timing	PCIe cards	4× X series multifunction DAQ card, 32 AI, 48 DIO, 4 AO, 1.25 MS/s	NI PCIe-6353	National Instruments
	PC	Black 4U case, 250 GB SSD, Intel Core i5-6500 (3.6 GHz), 8 GB DDR4, Asus intel LGA1151	various	various/World of Computers Ltd
Offset lock	Photodiode	High-bandwidth MSM photodetector	G4176-03	Hamamatsu
	Reference oscillator	7.500 GHz, 50 Ω SMA, custom made	KU LO 7500 RO-587	Kuhne electronic GmbH
	Amplifier with Bias-T	23 dB 1-7000 MHz, 50 Ω SMA (rubidium offset, used directly after PD)	KU LNA BB 0180 A-SMA-BT	Kuhne electronic GmbH
	Amplifier	23 dB 1-7000 MHz, 50 Ω SMA (rubidium offset)	KU LNA BB 0180 A-SMA	Kuhne electronic GmbH
	Amplifier	20 dB 5-1500 MHz, 50 Ω SMA (rubidium offset, used after mixer)	KU LNA BB 0515 A-SMA	Kuhne electronic GmbH
MW setup	Power amplifier	6400-7200 MHz, 40 dBm max. output power	KU PA 640720-10 A	Kuhne electronic GmbH
	Reference oscillator	Programmable oscillator unit	MKU LO 8-13 PLL	Kuhne electronic GmbH
	Circulator	4.5-9.0 GHz, 3-port circulator	CS-20	MCLI MW communications laboratories, Inc
	Antenna	Horn-antenna WG14(WG137), standard gain	14240-20 UAR70	Flann Microwave Ltd
Elements	Rubidium	Rubidium, 99.75% (metals basis)	044214	Alfa Aesar
	Potassium	Potassium-40 enriched 2.98% from potassium chloride, 200 mg	-	-

Acknowledgements

'Experimental science is teamwork.' I cannot imagine a project for which this statement could be more appropriate than ours. In the past three years I have had the great pleasure and honour to work in a team of clever, supportive, creative, curious, and challenging[1] minds.

This team was brought together and led by our supervisor Ulrich Schneider, who managed to convince everyone of us to embark on a long journey into the unknown and build a quasicrystal with ultracold atoms. For me, his deep knowledge of physics has been a never-ending source of inspiration and information. I am very grateful for his continuous support and constant availability to answer questions, even in busy weeks, be it in the office or on the phone, at any time of day or night.

The first members of the team were Matteo Sbroscia, Oliver Brix, Hendrik von Raven, and myself.

Matteo has been the central figure during my PhD. It is not easy to find words that adequately express my feelings towards him, except simply to state that I am extraordinarily grateful for his presence, both as friend and colleague. I could fill pages with anecdotes but still fail to do justice to the role he played in the past three years. Therefore I am going to borrow some phrases from a famous Cavendish alumnus who advised, 'Work with a teammate who is your intellectual equal' and, '[...] bring together the complementary talents of those involved.' While I seriously doubt that I have been, or ever will be, Matteo's intellectual equal, I think we did an O.K. job of profiting from each other's talents.[2]

Oliver was part of the duo, with Hendrik, that had joined us from LMU for a year's Master's project. He won the black belt in the disciplines of Autodesk Inventor and Mathematica, developing our magnetic transport system and designing the cooling block.

Scientists often dismiss supernatural abilities and black magic for not being compatible with the 'laws of nature',[3] but Hendrik's coding abilities certainly fall into these categories. He single-handedly built our timing system while at the same time planning, developing, and testing one of the most-relied-on components in the lab, the DDS board.

Ed Carter joined within the first year of this project, building a phase-stable interferometer for his Part III project. His arrival marked a new era, him being the first truly English person in the group which consisted, at the time, of four Germans and one

[1] 'But why?'

[2] his certainly being the more glamorous

[3] if there is such a thing

Italian.[4] Ed introduced wit and good humour, which, had it not been for Matteo, would have come as a complete novelty to us. Later, having started his PhD in the group, he quickly advanced to playing a vital role in the lab, leading the day-to-day activities and taking the next generation of students under his wing. Among many other accomplishments, Ed perfected the art of writing sequences and lab book entries.[5] I am also grateful for him taking over my position on the grad student committee.

[4] and, rumour has it, two British passports

[5] which sometimes read like crime novels

In the year 2016 we were joined by Max Melchner (from ETH) and Michael Höse (from LMU) for half-year internships. Max designed our dipole trap laser system and performed useful numerical simulations of the adiabatic loading process of the dipole trap. I am grateful for his mathematica scripts, including the trap frequency calculations. Michael, who – by complete coincidence – moved into the same flat share that Oliver had lived in, developed several useful GUIs, completed and characterised our beam shutter design, and implemented the microwave setup.

Jr-Chiun Yu started his PhD one year ago and he quickly absorbed a huge amount of information on how to run the machine. His contributions to the experiments are now indispensable and I am confident Jr-Chiun is going to ensure a bright future of the quasicrystal lab.

In the course of the experiment, we were joined by a number of hard-working project students, namely Callum Stevens, Joannis Koepsell, Attila Szabó, Robin Croft,[6] Shreya Arya, Marius Weber, and Elvinas Ribinskas.

[6] who implemented an evolutionary algorithm that we use to optimise RF evaporation sequences

One year ago, the optical lattice group expanded and quasicrystal's sibling, the Kagome lab, was born. Kagome boasts a fantastic team with Tiffany Harte, Max Melchner, Dan Reed, and Florian Störtz, as well as their former project students Péter Juhász, Greg Chant, and Luca Donini. Now the older sibling is constantly fretting that the younger one will do everything much better and more efficient than herself. Somehow it feels like 'Team Kagome' has been around since day one, and I am grateful for all their contributions to the group, regarding both physics and life outside the lab.

The optical lattice group is embedded in a wider Cavendish-cold-atom community with a strongly collaborative atmosphere. This is thanks to Zoran Hadzibabic and his team, namely Rob Smith, Christoph Eigen, Jay Man, Jake Glidden, Jinyi Zhang, Panos Christodoulou, Julian Schmitt, Lena Bartha, Timon Hilker, Maciej Galka, Milan Kristajic, and Nathaniel Vilas. I am particularly indebted to two former postdocs,[7] Nir Navon and Raphael Lopes, as well as Zoran & Rob, for their continuous support and advice while setting up the apparatus. I owe Zoran a great deal, both professionally and personally, and I am grateful for having been infected by his natural enthusiasm for science. Besides, I believe he is one of the select few[8] who truly share my limitless appreciation for Trinity's Full English.

[7] the lack of postdocs in the quasicrystal lab was partly compensated by an abundant supply in Zoran's group

[8] together with Nir, and Richard Fletcher

Next, I would like to express thanks to Andreas Nunnenkamp,

Tijmen Euser, and Mete Atatüre and his team for their support during my time at the Cavendish.

I am also grateful for the invaluable contributions to our lab by the Cavendish support staff, including Stephen Topliss, Dan Cross, Marzena Kulma, Graham Cox, Alan Turner, Dave Smith, Huw Prytherch, Nigel Palfrey, Kevin Mott, Gary Large, Chris Summerfield, and others. In addition, I would like to thank Pam Smith and the Rutherford Hub for doing a great job in administration.

Let's face it, setting up a new laboratory is a mixed bag. It can be an overwhelming, enjoyable, sometimes frustrating, sometimes rewarding, daunting, both stressful and exhilerating[9] task, but, more than anything else, it is time-consuming. I am deeply grateful to Matteo and our colleagues for sharing so many hours at the lab.[10] Despite those long hours, life outside the lab did exist. Unfortunately, naming all those wonderful people who made my life worth living (and will hopefully continue to do so) would probably lead to a very long and still incomplete list, so I am not going to attempt it. There must be a few exceptions, though. First and most important, I would like to thank my family, my parents Victoria and Christoph, my brothers Johannes and Emanuel, as well as Emanuel's wife Mai and their boys Samuel and Adrian. Emanuel's lot spent half a year in Cambridge, six wonderful months that I will cherish for the rest of my life.

[9] The emotions while seeing the first MOT and the first BEC in the lab could be described as a mixture of childish joy and what I imagine zero-g must feel like.

[10] The total number of hours spent together is comparable to the duration of a typical mission to the ISS.

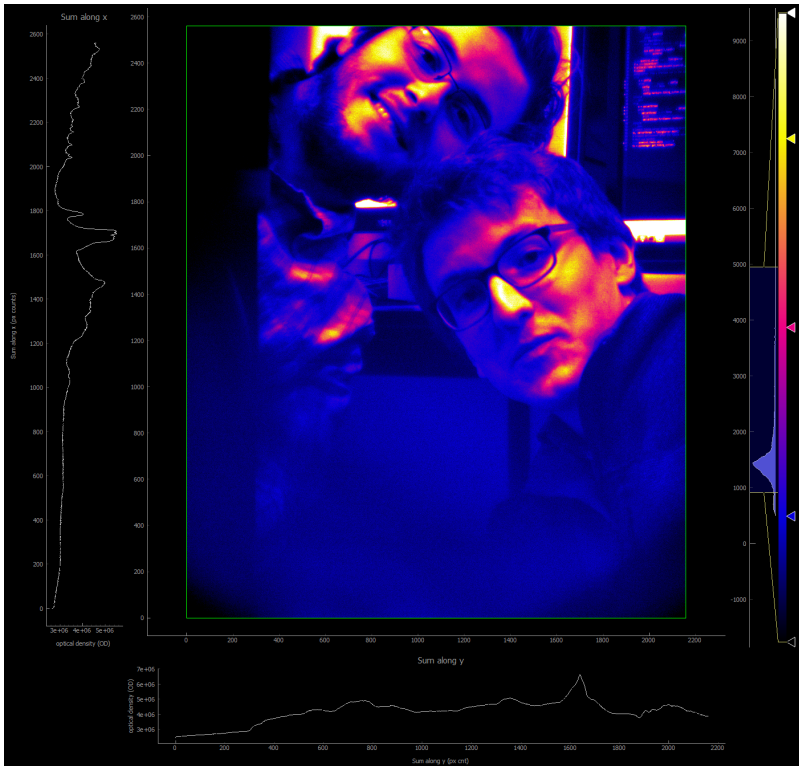

Figure A.1: Typical diffraction-limited image of two single bosons in their excited state.

Then, had Mirjam not saved me, I probably would have devolved during my PhD to an undernourished eydeet,[11] who uses all his energy for pondering physics problems and forgets the animate world around him. Thank you, Mirjam, for being there and being you.

[11] a kind of cave man

Another two consistent figures shall not go unnamed here: Daniel Malz and Angela Wittmann. Apart from being brilliant physicists, Daniel and Angela share my passion for music. And while I am happy that all three of us completed our PhDs,[12] I will sorely miss their frequent company in the future.

[12] within weeks of each other

The same goes for my dear friends at 4 Portugal St, Pearce A, Burrell's E, as well as the Barnwell lerds, EBC rowing, CUCO and CUMSSO, cold-atom football, chamber music sessions in the Frazer room, breakfast at Trinity's, snooker at WT's, the BA society, Pembroke Choir, CMS lunches, lab breakfasts, Trinity evensongs, astronomy board games, and the dihedral group.

I acknowledge financial support from the Cambridge Commonwealth, European & International Trust, as well as the EPSRC. This document was typeset using the `tufte-book` template[13] which is licensed under the Apache License, Version 2.0. I would like to thank Michael Feuerbacher, as well as Michael Baake and Uwe Grimm, for providing figures. I am grateful to Anika Bayer for her Adobe Illustrator skills and her advice on formatting. Finally, I would like to thank Ulrich, Matteo, Ed, Angela, Daniel, and Mirjam for proofreading.

[13] TUFTE-LATEX.GITHUB.IO/TUFTE-LATEX/

Bibliography

[1] D. Shechtman, I. Blech, D. Gratias, and J. Cahn, "Metallic Phase with Long-Range Orientational Order and No Translational Symmetry", Physical review letters **53**, 1951 (1984) (cited on pages 11, 26–27, 30).

[2] D. Levine, and P. J. Steinhardt, "Quasicrystals: a new class of ordered structures", Physical review letters **53**, 2477 (1984) (cited on page 11).

[3] M. Senechal, *Quasicrystals and geometry* (Cambridge University Press, Cambridge, 1995) (cited on pages 11, 27).

[4] H.-R. Trebin, *Quasicrystals: structure and physical properties* (Wiley-VCH, Weinheim; U.K., 2003) (cited on page 11).

[5] Y. E. Kraus, Y. Lahini, Z. Ringel, M. Verbin, and O. Zilberberg, "Topological States and Adiabatic Pumping in Quasicrystals", Physical Review Letters **109**, 106402 (2012) (cited on pages 11, 33–34, 102).

[6] Y. E. Kraus, and O. Zilberberg, "Topological Equivalence between the Fibonacci Quasicrystal and the Harper Model", Physical Review Letters **109**, 116404 (2012) (cited on pages 11–12).

[7] Y. E. Kraus, Z. Ringel, and O. Zilberberg, "Four-Dimensional Quantum Hall Effect in a Two-Dimensional Quasicrystal", Physical Review Letters **111**, 226401 (2013) (cited on page 11).

[8] R. Penrose, "The Rôle of Aesthetics in Pure and Applied Mathematical Research", Bulletin of the Institute of Mathematics and its Applications **10**, 266–271 (1974) (cited on pages 11, 28).

[9] M. Baake, and U. Grimm, editors, *Aperiodic Order. Volume 1: A Mathematical Invitation* (Cambridge University Press, Cambridge, 2013) (cited on pages 11, 15, 23–24, 27–31).

[10] B. Grünbaum, and G. C. Shephard, *Tilings and patterns*, A series of books in the mathematical sciences (W.H. Freeman, New York, 1987) (cited on pages 11, 27–28).

[11] W. Steurer, "Quasicrystals: What do we know? What do we want to know? What can we know?", Acta Crystallographica Section A Foundations and Advances **74**, 1–11 (2018) (cited on pages 11, 15, 18, 24, 30–34).

[12] E. M. Barber, *Aperiodic structures in condensed matter: fundamentals and applications*, Series in condensed matter physics (CRC Press, Boca Raton, London, 2009) (cited on pages 11, 15–16, 18–19, 33).

[13] W. Steurer, and D. Sutter-Widmer, "Photonic and phononic quasicrystals", Journal of Physics D: Applied Physics **40**, R229–R247 (2007) (cited on pages 11, 20, 33).

[14] L. Guidoni, B. Dépret, A. Di Stefano, and P. Verkerk, "Atomic diffusion in an optical quasicrystal with five-fold symmetry", Physical Review A **60**, R4233 (1999) (cited on pages 11, 20, 33).

[15] L. Guidoni, C. Triché, P. Verkerk, and G. Grynberg, "Quasiperiodic optical lattices", Physical review letters **79**, 3363 (1997) (cited on pages 11, 20, 33).

[16] J. Mikhael, J. Roth, L. Helden, and C. Bechinger, "Archimedean-like tiling on decagonal quasicrystalline surfaces", Nature **454**, 501–504 (2008) (cited on pages 11, 20, 33).

[17] J. Mikhael, M. Schmiedeberg, S. Rausch, J. Roth, H. Stark, and C. Bechinger, "Proliferation of anomalous symmetries in colloidal monolayers subjected to quasiperiodic light fields", Proceedings of the National Academy of Sciences **107**, 7214–7218 (2010) (cited on pages 11, 20, 33).

[18] M. Greiner, "Quantum phase transition from a superfluid to a Mott insulator in a gas of ultracold atoms", Nature **415**, 39–44 (2002) (cited on pages 12, 36).

[19] R. P. Feynman, "Simulating physics with computers", International journal of theoretical physics **21**, 467–488 (1982) (cited on page 12).

[20] I. Bloch, J. Dalibard, and S. Nascimbène, "Quantum simulations with ultracold quantum gases", Nature Physics **8**, 267–276 (2012) (cited on page 12).

[21] C. Gross, and I. Bloch, "Quantum simulations with ultracold atoms in optical lattices", Science **357**, 995–1001 (2017) (cited on page 12).

[22] U. Schneider, L. Hackermüller, J. P. Ronzheimer, S. Will, S. Braun, T. Best, I. Bloch, E. Demler, S. Mandt, D. Rasch, and A. Rosch, "Fermionic transport and out-of-equilibrium dynamics in a homogeneous Hubbard model with ultracold atoms", Nature Physics **8**, 213–218 (2012) (cited on pages 12, 77, 97).

[23] J.-y. Choi, S. Hild, J. Zeiher, P. Schauss, A. Rubio-Abadal, T. Yefsah, V. Khemani, D. A. Huse, I. Bloch, and C. Gross, "Exploring the many-body localization transition in two dimensions", Science **352**, 1547–1552 (2016) (cited on page 12).

[24] P. Bordia, H. Lüschen, S. Scherg, S. Gopalakrishnan, M. Knap, U. Schneider, and I. Bloch, "Probing Slow Relaxation and Many-Body Localization in Two-Dimensional Quasiperiodic Systems", Physical Review X **7**, 041047 (2017) (cited on pages 12, 34, 84, 103).

[25] F. Görg, M. Messer, K. Sandholzer, G. Jotzu, R. Desbuquois, and T. Esslinger, "Enhancement and sign change of magnetic correlations in a driven quantum many-body system", Nature **553**, 481–485 (2018) (cited on pages 12, 82).

[26] J. Léonard, A. Morales, P. Zupancic, T. Esslinger, and T. Donner, "Supersolid formation in a quantum gas breaking a continuous translational symmetry", Nature **543**, 87–90 (2017) (cited on page 12).

[27] J.-R. Li, J. Lee, W. Huang, S. Burchesky, B. Shteynas, F. Ç. Top, A. O. Jamison, and W. Ketterle, "A stripe phase with supersolid properties in spin–orbit-coupled Bose–Einstein condensates", Nature **543**, 91–94 (2017) (cited on page 12).

[28] C. Eigen, J. A. P. Glidden, R. Lopes, E. A. Cornell, R. P. Smith, and Z. Hadzibabic, "Universal Prethermal Dynamics of Bose Gases Quenched to Unitarity", arXiv:1805.09802 (2018) (cited on page 12).

[29] A. Eckardt, "Colloquium: Atomic quantum gases in periodically driven optical lattices", Reviews of Modern Physics **89**, 011004 (2017) (cited on pages 12, 82).

[30] A. Acín, I. Bloch, H. Buhrman, T. Calarco, C. Eichler, J. Eisert, D. Esteve, N. Gisin, S. J. Glaser, F. Jelezko, S. Kuhr, M. Lewenstein, M. F. Riedel, P. O. Schmidt, R. Thew, A. Wallraff, I. Walmsley, and F. K. Wilhelm, "The European Quantum Technologies Roadmap", New Journal of Physics **20**, arXiv: 1712.03773, 080201 (2018) (cited on page 12).

[31] T. S. Cubitt, D. Perez-Garcia, and M. M. Wolf, "Undecidability of the spectral gap", Nature **528**, 207–211 (2015) (cited on pages 12, 28, 99).

[32]I. U. of Crystallography, "Quasicrystal", Online Dictionary of Crystallography (2018) (cited on pages 16–17).

[33] IUCr, "International Union of Crystallography Report of the Executive Committee for 1991", Acta Crystallographica Section A Foundations of Crystallography **48**, 922–946 (1991) (cited on page 16).

[34]I. U. of Crystallography, "Crystal", Online Dictionary of Crystallography (2018) (cited on page 16).

[35]R. Lifshitz, "The Definition of Quasicrystals", arXiv preprint cond-mat/0008152 (2000) (cited on pages 16–18).

[36]I. U. of Crystallography, "Incommensurate modulated structure", Online Dictionary of Crystallography (2018) (cited on page 16).

[37]I. U. of Crystallography, "Incommensurate composite crystal", Online Dictionary of Crystallography (2018) (cited on page 17).

[38]I. U. of Crystallography, "Friedel's law", Online Dictionary of Crystallography (2018) (cited on page 17).

[39]H. A. Bohr, "Die Theorie der fastperiodischen Funktionen", Ergebnisse der Mathematik und ihrer Grenzgebiete **I**, 446 (1932) (cited on pages 17–18).

[40] common, "Quasicrystal", Wikipedia (2018) (cited on page 18).

[41]I. U. of Crystallography, "Quasiperiodicity", Online Dictionary of Crystallography (2018) (cited on page 18).

[42]L. Fibonacci, *Fibonacci's Liber abaci: a translation into modern English of Leonardo Pisano's Book of calculation [translated by Laurence Sigler]*, Sources and studies in the history of mathematics and physical sciences (Springer, New York, 2002) (cited on page 19).

[43]C. Janot, *Quasicrystals: primer*, 2nd ed, Monographs on the Physics & Chemistry of Materials Vol.50 (Oxford University Press, Oxford, 1995) (cited on page 19).

[44]D. Levine, and P. J. Steinhardt, "Quasicrystals. I. Definition and structure", Physical Review B **34**, 596 (1986) (cited on pages 19, 22).

[45]E. Schrödinger, *What is life? the physical aspect of the living cell*, Canto edition., Canto classics (Cambridge University Press, Cambridge, 1992) (cited on page 19).

[46]P. Ball, "In retrospect: What Is Life?", Nature **560**, 548–550 (2018) (cited on page 19).

[47]U. Grimm, and M. Schreiber, "Aperiodic Tilings on the Computer", arXiv:cond-mat/9903010 (1999) (cited on pages 20, 29).

[48]W. E. Leland, M. S. Taqqu, W. Willinger, and D. V. Wilson, "On the self-similar nature of Ethernet traffic (extended version)", IEEE/ACM Transactions on Networking **2**, 1–15 (1994) (cited on page 20).

[49]S Havlin, S. V. Buldyrev, A. L. Goldberger, R. N. Mantegna, and S. M. Ossadnik, "Fractals in Biology and Medicine", Chaos, Solitons & Fractals **6**, 171–201 (1995) (cited on page 20).

[50]Y. Baryshev, and P. Teerikorpi, *Discovery of Cosmic Fractals* (World Scientific Press, 2002) (cited on page 20).

[51]T. G. Faticoni, *The mathematics of infinity: a guide to great ideas*, 2nd ed., Pure and applied mathematics (John Wiley & Sons : Unnumbered) (Wiley, Hoboken, N.J., 2012) (cited on page 22).

[52]M. Baake, and U. Grimm, "Kinematic diffraction is insufficient to distinguish order from disorder", Physical Review B **79**, 020203 (2009) (cited on page 24).

[53] W. Steurer, "Why are quasicrystals quasiperiodic?", Chemical Society Reviews **41**, 6719 (2012) (cited on pages 24, 26).

[54] W. Steurer, "Twenty years of structure research on quasicrystals. Part I. Pentagonal, octagonal, decagonal and dodecagonal quasicrystals", Zeitschrift für Kristallographie - Crystalline Materials **219**, 391 (2004) (cited on pages 24, 31–32).

[55] I. U. of Crystallography, "Aperiodic crystal", Online Dictionary of Crystallography, Online Dictionary of Crystallography (2018) (cited on page 24).

[56] M. de Boissieu, "Phonons, phasons and atomic dynamics in quasicrystals", Chemical Society Reviews **41**, 6778 (2012) (cited on page 25).

[57] W. Scherrer, "Die Einlagerung eines regulären Vielecks in ein Gitter.", Elemente der Mathematik **1**, 97–98 (1946) (cited on page 26).

[58] M. Baake, and U. Grimm, "Mathematical diffraction of aperiodic structures", Chemical Society Reviews **41**, 6821 (2012) (cited on page 27).

[59] H. Wang, "Proving theorems by pattern recognition — II", The Bell System Technical Journal **40**, 1–41 (1961) (cited on page 27).

[60] H. Wang, *Games, Logic and Computers. In: Computation, Logic, Philosophy. Mathematics and its Application (China Series), vol 2.* (Springer, Dordrecht, 1965) (cited on page 27).

[61] R. Berger, "The undecidability of the domino problem", Memoirs of the American Mathematical Society **66**, 1–72 (1966) (cited on page 27).

[62] A. M. Turing, "On Computable Numbers, with an Application to the Entscheidungsproblem", Proceedings of the London Mathematical Society **s2-42**, 230–265 (1937) (cited on page 27).

[63] H. Wang, "Notes on a class of tiling problems", Fundamental Mathematics **82**, 295–305 (1975) (cited on page 27).

[64] E. Winfree, F. Liu, L. A. Wenzler, and N. C. Seeman, "Design and self-assembly of two-dimensional DNA crystals", Nature **394**, 539–544 (1998) (cited on page 28).

[65] U. Grimm, "Aperiodic tilings on Mathematica", webpage (2014) (cited on page 29).

[66] A. Mackay, "Crystallography and the Penrose pattern", Physica **114A**, 609–613 (1982) (cited on pages 30, 33).

[67] M. Baake, and D. Joseph, "Ideal and defective vertex configurations in the planar octagonal quasilattice", Physical Review B **42**, 8091–8102 (1990) (cited on page 31).

[68] N. Wang, H. Chen, and K. H. Kuo, "Two-dimensional quasicrystal with eightfold rotational symmetry", Physical Review Letters **59**, 1010–1013 (1987) (cited on page 32).

[69] A.-P. Tsai, ""Back to the Future"-An Account Discovery of Stable Quasicrystals", Accounts of Chemical Research **36**, 31–38 (2003) (cited on page 32).

[70] J. Dolinšek, "Electrical and thermal transport properties of icosahedral and decagonal quasicrystals", Chemical Society Reviews **41**, 6730 (2012) (cited on page 32).

[71] D. P. Varn, and J. P. Crutchfield, "Chaotic Crystallography: How the physics of information reveals structural order in materials", arXiv:1409.5930 (2014) (cited on page 33).

[72] J. H. E. Cartwright, and A. L. Mackay, "Beyond crystals: the dialectic of materials and information", Philosophical Transactions of the Royal Society A: Mathematical, Physical and Engineering Sciences **370**, 2807–2822 (2012) (cited on page 33).

[73]L. Bindi, P. J. Steinhardt, N. Yao, and P. J. Lu, "Natural Quasicrystals", Science **324**, 1306–1309 (2009) (cited on page 33).

[74]L. Bindi, C. Lin, C. Ma, and P. J. Steinhardt, "Collisions in outer space produced an icosahedral phase in the Khatyrka meteorite never observed previously in the laboratory", Scientific Reports **6**, 38117 (2016) (cited on page 33).

[75]R. Merlin, K. Bajema, R. Clarke, F. Y. Juang, and P. K. Bhattacharya, "Quasiperiodic GaAs-AlAs Heterostructures", Physical Review Letters **55**, 1768–1770 (1985) (cited on page 33).

[76]X. Zeng, G. Ungar, Y. Liu, V. Percec, A. E. Dulcey, and J. K. Hobbs, "Supramolecular dendritic liquid quasicrystals", Nature **428**, 157–160 (2004) (cited on page 33).

[77]K. Hayashida, T. Dotera, A. Takano, and Y. Matsushita, "Polymeric Quasicrystal: Mesoscopic Quasicrystalline Tiling in A B C Star Polymers", Physical Review Letters **98**, 195502 (2007) (cited on page 33).

[78]D. V. Talapin, E. V. Shevchenko, M. I. Bodnarchuk, X. Ye, J. Chen, and C. B. Murray, "Quasicrystalline order in self-assembled binary nanoparticle superlattices", Nature **461**, 964–967 (2009) (cited on page 33).

[79]S. Fischer, A. Exner, K. Zielske, J. Perlich, S. Deloudi, W. Steurer, P. Lindner, and S. Förster, "Colloidal quasicrystals with 12-fold and 18-fold diffraction symmetry", Proceedings of the National Academy of Sciences **108**, 1810–1814 (2011) (cited on page 33).

[80]N. K. Efremidis, S. Sears, D. N. Christodoulides, J. W. Fleischer, and M. Segev, "Discrete solitons in photorefractive optically induced photonic lattices", Physical Review E **66** (2002) 10.1103/PhysRevE.66.046602 (cited on page 33).

[81]B. Freedman, G. Bartal, M. Segev, R. Lifshitz, D. N. Christodoulides, and J. W. Fleischer, "Wave and defect dynamics in nonlinear photonic quasicrystals", Nature **440**, 1166–1169 (2006) (cited on page 33).

[82]B. Freedman, R. Lifshitz, J. W. Fleischer, and M. Segev, "Phason dynamics in nonlinear photonic quasicrystals", Nature Materials **6**, 776–781 (2007) (cited on page 33).

[83]A. Dareau, E. Levy, M. B. Aguilera, R. Bouganne, E. Akkermans, F. Gerbier, and J. Beugnon, "Revealing the Topology of Quasicrystals with a Diffraction Experiment", Physical Review Letters **119**, 215304 (2017) (cited on page 33).

[84]S. J. Ahn, P. Moon, T.-H. Kim, H.-W. Kim, H.-C. Shin, E. H. Kim, H. W. Cha, S.-J. Kahng, P. Kim, M. Koshino, Y.-W. Son, C.-W. Yang, and J. R. Ahn, "Dirac electrons in a dodecagonal graphene quasicrystal", Science **361**, 782–786 (2018) (cited on page 33).

[85]N. Macé, A. Jagannathan, and M. Duneau, "Quantum Simulation of a 2d Quasicrystal with Cold Atoms", Crystals **6**, 124 (2016) (cited on pages 33, 84).

[86]M. Lohse, C. Schweizer, H. M. Price, O. Zilberberg, and I. Bloch, "Exploring 4d quantum Hall physics with a 2d topological charge pump", Nature **553**, 55–58 (2018) (cited on pages 34, 103).

[87]M. Aidelsburger, "Artificial Gauge Fields with Ultracold Atoms in Optical Lattices", LMU Munich **PhD Thesis** (2016) (cited on page 34).

[88]M. Schreiber, S. S. Hodgman, P. Bordia, H. P. Lüschen, M. H. Fischer, R. Vosk, E. Altman, U. Schneider, and I. Bloch, "Observation of many-body localization of interacting fermions in a quasirandom optical lattice", Science **349**, 842–845 (2015) (cited on pages 34, 103).

[89]M. Žnidarič, and M. Ljubotina, "Interaction instability of localization in quasiperiodic systems", Proceedings of the National Academy of Sciences, 201800589 (2018) (cited on pages 34, 103).

[90] H. P. Lüschen, P. Bordia, S. S. Hodgman, M. Schreiber, S. Sarkar, A. J. Daley, M. H. Fischer, E. Altman, I. Bloch, and U. Schneider, "Signatures of Many-Body Localization in a Controlled Open Quantum System", Physical Review X **7**, 011034 (2017) (cited on pages 34, 103).

[91] H. P. Lüschen, P. Bordia, S. Scherg, F. Alet, E. Altman, U. Schneider, and I. Bloch, "Observation of Slow Dynamics near the Many-Body Localization Transition in One-Dimensional Quasiperiodic Systems", Physical Review Letters **119**, 260401 (2017) (cited on pages 34, 103).

[92] V. Khemani, D. N. Sheng, and D. A. Huse, "Two Universality Classes for the Many-Body Localization Transition", Physical Review Letters **119**, 075702 (2017) (cited on pages 34, 103).

[93] C. Chin, R. Grimm, P. Julienne, and E. Tiesinga, "Feshbach resonances in ultracold gases", Reviews of Modern Physics **82**, 1225–1286 (2010) (cited on pages 35–36, 69–70).

[94] J. I. Cirac, and P. Zoller, "Quantum Computations with Cold Trapped Ions", Physical Review Letters **74**, 4091–4094 (1995) (cited on page 35).

[95] J. G. Bohnet, B. C. Sawyer, J. W. Britton, M. L. Wall, A. M. Rey, M. Foss-Feig, and J. J. Bollinger, "Quantum spin dynamics and entanglement generation with hundreds of trapped ions", Science **352**, 1297 (2016) (cited on page 35).

[96] G. Pupillo, A. Micheli, H. P. Büchler, and P. Zoller, "Condensed Matter Physics with Cold Polar Molecules", arXiv:0805.1896 (2008) (cited on page 36).

[97] M. H. Anderson, J. R. Ensher, M. R. Matthews, C. E. Wieman, and E. A. Cornell, "Observation of Bose-Einstein Condensation in a Dilute Atomic Vapor", Science **269**, 198–201 (1995) (cited on pages 36, 72).

[98] K. B. Davis, M.-O. Mewes, M. R. Andrews, N. J. Van Druten, D. S. Durfee, D. M. Kurn, and W. Ketterle, "Bose-Einstein condensation in a gas of sodium atoms", Physical review letters **75**, 3969 (1995) (cited on page 36).

[99] C. C. Bradley, C. A. Sackett, J. J. Tollett, and R. G. Hulet, "Evidence of Bose-Einstein condensation in an atomic gas with attractive interactions", Physical Review Letters **75**, 1687 (1995) (cited on page 36).

[100] H. Bernien, S. Schwartz, A. Keesling, H. Levine, A. Omran, H. Pichler, S. Choi, A. S. Zibrov, M. Endres, M. Greiner, V. Vuletić, and M. D. Lukin, "Probing many-body dynamics on a 51-atom quantum simulator", Nature **551**, 579 (2017) (cited on page 36).

[101] A. G. Truscott, K. E. Strecker, W. I. McAlexander, G. B. Partridge, and R. G. Hulet, "Observation of Fermi Pressure in a Gas of Trapped Atoms", Science **291**, 2570 (2001) (cited on page 36).

[102] B. DeMarco, and D. S. Jin, "Onset of Fermi degeneracy in a trapped atomic gas", Science **285**, 1703–1706 (1999) (cited on page 36).

[103] G. Roati, M. Zaccanti, C. D'Errico, J. Catani, M. Modugno, A. Simoni, M. Inguscio, and G. Modugno, "K 39 Bose-Einstein Condensate with Tunable Interactions", Physical Review Letters **99**, 010403 (2007) (cited on pages 36, 42).

[104] T. Esslinger, "Fermi-Hubbard Physics with Atoms in an Optical Lattice", Annual Review of Condensed Matter Physics **1**, 129–152 (2010) (cited on page 36).

[105] D. Greif, T. Uehlinger, G. Jotzu, L. Tarruell, and T. Esslinger, "Short-Range Quantum Magnetism of Ultracold Fermions in an Optical Lattice", Science **340**, 1307–1310 (2013) (cited on page 36).

[106] A. Mazurenko, C. S. Chiu, G. Ji, M. F. Parsons, M. Kanász-Nagy, R. Schmidt, F. Grusdt, E. Demler, D. Greif, and M. Greiner, "A cold-atom Fermi–Hubbard antiferromagnet", Nature **545**, 462–466 (2017) (cited on page 36).

[107]Y. Takasu, K. Maki, K. Komori, T. Takano, K. Honda, M. Kumakura, T. Yabuzaki, and Y. Takahashi, "Spin-Singlet Bose-Einstein Condensation of Two-Electron Atoms", Physical Review Letters **91**, 040404 (2003) (cited on page 36).

[108]T. Fukuhara, Y. Takasu, M. Kumakura, and Y. Takahashi, "Degenerate Fermi Gases of Ytterbium", Physical Review Letters **98**, 030401 (2007) (cited on page 36).

[109]S. Stellmer, M. K. Tey, B. Huang, R. Grimm, and F. Schreck, "Bose-Einstein Condensation of Strontium", Physical Review Letters **103**, 200401 (2009) (cited on page 36).

[110]Y. N. M. de Escobar, P. G. Mickelson, M. Yan, B. J. DeSalvo, S. B. Nagel, and T. C. Killian, "Bose-Einstein Condensation of Sr 84", Physical Review Letters **103**, 200402 (2009) (cited on page 36).

[111]S. Stellmer, R. Grimm, and F. Schreck, "Production of quantum-degenerate strontium gases", Physical Review A **87**, 013611 (2013) (cited on page 36).

[112]M. Lu, N. Q. Burdick, S. H. Youn, and B. L. Lev, "Strongly Dipolar Bose-Einstein Condensate of Dysprosium", Physical Review Letters **107**, 190401 (2011) (cited on page 36).

[113]M. Lu, N. Q. Burdick, and B. L. Lev, "Quantum Degenerate Dipolar Fermi Gas", Physical Review Letters **108**, 215301 (2012) (cited on page 36).

[114]K. Aikawa, A. Frisch, M. Mark, S. Baier, A. Rietzler, R. Grimm, and F. Ferlaino, "Bose-Einstein Condensation of Erbium", Physical Review Letters **108**, 210401 (2012) (cited on page 36).

[115]K. Aikawa, A. Frisch, M. Mark, S. Baier, R. Grimm, and F. Ferlaino, "Reaching Fermi Degeneracy via Universal Dipolar Scattering", Physical Review Letters **112**, 010404 (2014) (cited on page 36).

[116]M. Greiner, I. Bloch, T. W. Hänsch, and T. Esslinger, "Magnetic transport of trapped cold atoms over a large distance", Physical Review A **63**, 031401 (2001) (cited on page 37).

[117]M. Greiner, "Magnetischer Transfer von Atomen - ein Weg zur einfachen Bose-Einstein-Kondensation", Diploma thesis (LMU Munich, Germany, 2000) (cited on pages 37, 53–54).

[118]T. Rom, "Bosonische und fermionische Quantengase in dreidimensionalen optischen Gittern", PhD thesis (LMU Munich and MPQ Garching, Germany, Oct. 2009) (cited on pages 37, 51).

[119]L. Duca, "Probing topological properties of Bloch bands with ultracold atoms in a honeycomb optical lattice", PhD thesis (LMU Munich, Germany, July 2015) (cited on pages 37, 49).

[120]T. Li, "Probing Bloch band geometry with ultracold atoms in optical lattices", PhD thesis (LMU Munich, Germany, May 2016) (cited on pages 37, 49, 51, 53).

[121]T. Stöferle, "Exploring Atomic Quantum Gases in Optical Lattices", PhD thesis (ETH Zurich, Switzerland, 2005) (cited on page 37).

[122]J. I. Gillen, "The Quantum Gas Microscope", PhD thesis (Harvard University, Cambridge, Massachusetts, Oct. 2009) (cited on page 37).

[123]T. Badr, D. B. Ali, J. Seaward, Y. Guo, F. Wiotte, R. Dubessy, H. Perrin, and A. Perrin, "Comparison of time profiles for the magnetic transport of cold atoms", arXiv:1809.07096 (2018) (cited on page 37).

[124]M. Sbroscia, "Towards an optical quasicrystal with ultracold atoms", First-year report (University of Cambridge, Cambridge, Jan. 2016) (cited on pages 38, 48–50, 52, 54).

[125]W. Ketterle, D. S. Durfee, and D. M. Stamper-Kurn, "Making, probing and understanding Bose-Einstein condensates", arXiv preprint cond-mat/9904034 **5** (1999) (cited on pages 41, 48, 57).

[126]H. J. Metcalf, and P. Van der Straten, *Laser cooling and trapping*, Graduate texts in contemporary physics (Springer, New York, 1999) (cited on pages 41, 48).

[127]C. Foot, *Atomic physics*, Oxford master series in atomic, optical and laser physics (Oxford University Press, Oxford, 2005) (cited on pages 41, 43–44, 48, 50, 53, 61).

[128]C. B. Alcock, V. P. Itkin, and M. K. Horrigan, "Vapour Pressure Equations for the Metallic Elements: 298–2500k", Canadian Metallurgical Quarterly **23**, 309–313 (1984) (cited on page 41).

[129]C. Eigen, A. L. Gaunt, A. Suleymanzade, N. Navon, Z. Hadzibabic, and R. P. Smith, "Observation of Weak Collapse in a Bose-Einstein Condensate", Physical Review X **6**, 041058 (2016) (cited on page 42).

[130]R. J. Fletcher, R. Lopes, J. Man, N. Navon, R. P. Smith, M. W. Zwierlein, and Z. Hadzibabic, "Two- and three-body contacts in the unitary Bose gas", Science **355**, 377–380 (2017) (cited on pages 42, 70).

[131]R. L. D. Campbell, R. P. Smith, N. Tammuz, S. Beattie, S. Moulder, and Z. Hadzibabic, "Efficient production of large K 39 Bose-Einstein condensates", Physical Review A **82**, 063611 (2010) (cited on pages 42, 65–66).

[132]J. P. Ronzheimer, M. Schreiber, S. Braun, S. S. Hodgman, S. Langer, I. P. McCulloch, F. Heidrich-Meisner, I. Bloch, and U. Schneider, "Expansion Dynamics of Interacting Bosons in Homogeneous Lattices in One and Two Dimensions", Physical Review Letters **110**, 205301 (2013) (cited on page 42).

[133]G. Salomon, L. Fouché, S. Lepoutre, A. Aspect, and T. Bourdel, "All-optical cooling of K 39 to Bose-Einstein condensation", Physical Review A **90**, 033405 (2014) (cited on pages 42, 56).

[134]L. Wacker, N. B. Jørgensen, D. Birkmose, R. Horchani, W. Ertmer, C. Klempt, N. Winter, J. Sherson, and J. J. Arlt, "Tunable dual-species Bose-Einstein condensates of K 39 and Rb 87", Physical Review A **92**, 053602 (2015) (cited on page 42).

[135]M. Gröbner, P. Weinmann, F. Meinert, K. Lauber, E. Kirilov, and H.-C. Nägerl, "A new quantum gas apparatus for ultracold mixtures of K and Cs and KCs ground-state molecules", Journal of Modern Optics **63**, 1829–1839 (2016) (cited on pages 42, 51, 53).

[136]C. R. Cabrera, L. Tanzi, J. Sanz, B. Naylor, P. Thomas, P. Cheiney, and L. Tarruell, "Quantum liquid droplets in a mixture of Bose-Einstein condensates", Science **359**, 301–304 (2018) (cited on page 42).

[137]D. Nath, R. K. Easwaran, G. Rajalakshmi, and C. S. Unnikrishnan, "Quantum-interference-enhanced deep sub-Doppler cooling of 39 K atoms in gray molasses", Physical Review A **88**, 053407 (2013) (cited on page 42).

[138]G. Salomon, L. Fouché, P. Wang, A. Aspect, P. Bouyer, and T. Bourdel, "Gray-molasses cooling of ^{39} K to a high phase-space density", EPL (Europhysics Letters) **104**, 63002 (2013) (cited on page 42).

[139]D. A. Steck, *Rubidium 87 D line data* (2001) (cited on pages 43, 45).

[140]T. G. Tiecke, "Properties of potassium", University of Amsterdam, The Netherlands, Thesis (2010) (cited on pages 43, 45, 59).

[141]C. J. Bordé, "Spectroscopie d'absorption saturée de diverses molécules au moyen des lasers à gaz carbonique et à protoxyde d'azote", CR Acad. Sc. Paris **271**, 371–374 (1970) (cited on page 44).

[142]P. Smith, and T. Hänsch, "Cross-Relaxation Effects in the Saturation of the 6328-A Neon-Laser Line", Physical review letters **26**, 740–743 (1971) (cited on page 44).

[143]T. Hänsch, M. Levenson, and A. Schawlow, "Complete Hyperfine Structure of a Molecular Iodine Line", Phys. Rev. Lett. **26**, 946–949 (1971) (cited on page 44).

[144]A. L. Schawlow, "Spectroscopy in a new light", Reviews of Modern Physics **54**, 697 (1982) (cited on page 44).

[145]E. D. Black, "An introduction to Pound–Drever–Hall laser frequency stabilization", American Journal of Physics **69**, 79–87 (2001) (cited on page 44).

[146]U. Schünemann, H. Engler, R. Grimm, M. Weidemüller, and M. Zielonkowski, "Simple scheme for tunable frequency offset locking of two lasers", Review of Scientific Instruments **70**, 242–243 (1999) (cited on page 46).

[147]T. W. Hänsch, and A. L. Schawlow, "Cooling of gases by laser radiation", Optics Communications **13**, 68–69 (1975) (cited on pages 48–49).

[148]K. Dieckmann, R. Spreeuw, M. Weidemüller, and J. Walraven, "Two-dimensional magneto-optical trap as a source of slow atoms", Phys. Rev. A **58**, 3891 (1998) (cited on page 49).

[149]J. Schoser, A. Batär, R. Löw, V. Schweikhard, A. Grabowski, Y. B. Ovchinnikov, and T. Pfau, "Intense source of cold Rb atoms from a pure two-dimensional magneto-optical trap", Physical Review A **66**, 023410 (2002) (cited on page 49).

[150]S. Chaudhuri, S. Roy, and C. S. Unnikrishnan, "Realization of an intense cold Rb atomic beam based on a two-dimensional magneto-optical trap: Experiments and comparison with simulations", Physical Review A **74**, 023406 (2006) (cited on page 49).

[151]T. G. Tiecke, S. D. Gensemer, A. Ludewig, and J. T. M. Walraven, "High-flux two-dimensional magneto-optical-trap source for cold lithium atoms", Physical Review A **80**, 013409 (2009) (cited on page 49).

[152]V. Gokhroo, G Rajalakshmi, R. K. Easwaran, and C. S. Unnikrishnan, "Sub-Doppler deep-cooled bosonic and fermionic isotopes of potassium in a compact 2d $^+$ –3d MOT set-up", Journal of Physics B: Atomic, Molecular and Optical Physics **44**, 115307 (2011) (cited on page 49).

[153]T. Y. Li, "An Apparatus for Probing Fermions in Quasi-Two-Dimensional Geometry", Master's thesis (LMU Munich, 2011) (cited on page 49).

[154]M. Boll, "A 2d+ -3d MOT system for producing laser-cooled K-Rb mixtures", Diploma thesis (MPQ Garching and Johannes Gutenberg Universität Mainz, Germany, Nov. 2011) (cited on page 49).

[155]L. G. Marcassa, G. D. Telles, S. R. Muniz, and V. S. Bagnato, "Collisional losses in a K-Rb cold mixture", Physical Review A **63**, 013413 (2000) (cited on page 50).

[156]J. Goldwin, S. B. Papp, B. DeMarco, and D. S. Jin, "Two-species magneto-optical trap with 40 K and 87 Rb", Physical Review A **65**, 021402 (2002) (cited on page 50).

[157]W. Ketterle, K. B. Davis, M. A. Joffe, A. Martin, and D. E. Pritchard, "High densities of cold atoms in a dark spontaneous-force optical trap", Physical review letters **70**, 2253 (1993) (cited on page 51).

[158]C. S. Adams, H. J. Lee, N. Davidson, M. Kasevich, and S. Chu, "Evaporative Cooling in a Crossed Dipole Trap", Physical Review Letters **74**, 3577–3580 (1995) (cited on page 51).

[159]W. Petrich, M. H. Anderson, J. R. Ensher, and E. A. Cornell, "Behavior of atoms in a compressed magneto-optical trap", Journal of the Optical Society of America B **11**, 1332 (1994) (cited on page 51).

[160] N. Tammuz, "Thermodynamics of ultracold 39k atomic Bose gases with tuneable interactions", PhD thesis (University of Cambridge, Cambridge, 2011) (cited on pages 51, 53, 72).

[161] T. Hilker, "Laser Cooling of Bosonic and Fermionic Lithium", Diploma thesis (MPQ Garching and Technische Universität München, Germany, Sept. 2012) (cited on page 51).

[162] A. D. Tranter, H. J. Slatyer, M. R. Hush, A. C. Leung, J. L. Everett, K. V. Paul, P. Vernaz-Gris, P. K. Lam, B. C. Buchler, and G. T. Campbell, "Multiparameter optimisation of a magneto-optical trap using deep learning", arXiv:1805.00654 (2018) (cited on page 51).

[163] P. J. Ungar, D. S. Weiss, E. Riis, and S. Chu, "Optical molasses and multilevel atoms: theory", Journal of the Optical Society of America B **6**, 2058 (1989) (cited on page 51).

[164] P. D. Lett, W. D. Phillips, S. L. Rolston, C. E. Tanner, R. N. Watts, and C. I. Westbrook, "Optical molasses", J. Opt. Soc. Am. B **6**, 2084–2107 (1989) (cited on page 51).

[165] J. Dalibard, and C. Cohen-Tannoudji, "Laser cooling below the Doppler limit by polarization gradients: simple theoretical models", Journal of the Optical Society of America B **6**, 2023 (1989) (cited on pages 51, 61).

[166] A. L. Migdall, J. V. Prodan, W. D. Phillips, T. H. Bergeman, and H. J. Metcalf, "First Observation of Magnetically Trapped Neutral Atoms", Physical Review Letters **54**, 2596–2599 (1985) (cited on page 53).

[167] O. Brix, "Towards Bose-Fermi Mixtures in Novel Optical Lattices", Master's thesis (LMU Munich, Germany, 2016) (cited on pages 53–55).

[168] A. L. Gaunt, T. F. Schmidutz, I. Gotlibovych, R. P. Smith, and Z. Hadzibabic, "Bose-Einstein Condensation of Atoms in a Uniform Potential", Physical Review Letters **110**, 200406 (2013) (cited on page 54).

[169] H. F. Hess, "Evaporative cooling of magnetically trapped and compressed spin-polarized hydrogen", Physical Review B **34**, 3476–3479 (1986) (cited on page 56).

[170] W. Petrich, M. H. Anderson, J. R. Ensher, and E. A. Cornell, "Stable, Tightly Confining Magnetic Trap for Evaporative Cooling of Neutral Atoms", Physical Review Letters **74**, 3352–3355 (1995) (cited on page 56).

[171] K. B. Davis, M.-O. Mewes, M. A. Joffe, M. R. Andrews, and W. Ketterle, "Evaporative Cooling of Sodium Atoms", Physical Review Letters **74**, 5202–5205 (1995) (cited on page 56).

[172] J. Fortágh, and C. Zimmermann, "Magnetic microtraps for ultracold atoms", Reviews of Modern Physics **79**, 235–289 (2007) (cited on page 56).

[173] H. von Raven, "Direct digital synthesis and integrated experiment control for a novel lattice setup", Master's thesis (LMU Munich and University of Cambridge, Cambridge, Oct. 2016) (cited on page 57).

[174] R. J. Fletcher, M. Robert-de Saint-Vincent, J. Man, N. Navon, R. P. Smith, K. G. H. Viebahn, and Z. Hadzibabic, "Connecting Berezinskii-Kosterlitz-Thouless and BEC Phase Transitions by Tuning Interactions in a Trapped Gas", Physical Review Letters **114**, 255302 (2015) (cited on page 58).

[175] R. Grimm, M. Weidemüller, and Y. B. Ovchinnikov, "Optical dipole traps for neutral atoms", arXiv:physics/9902072 (1999) (cited on pages 61–63).

[176] J. Dalibard, and C. Cohen-Tannoudji, "Dressed-atom approach to atomic motion in laser light: the dipole force revisited", Journal of the Optical Society of America B **2**, 1707 (1985) (cited on page 61).

[177]W. Ketterle, and N. V. Druten, "Evaporative Cooling of Trapped Atoms", *Advances In Atomic, Molecular, and Optical Physics*, Vol. 37, edited by B. Bederson, and H. Walther, (Academic Press, Jan. 1996), pages 181–236 (cited on page 66).

[178]C. J. Myatt, E. A. Burt, R. W. Ghrist, E. A. Cornell, and C. E. Wieman, "Production of Two Overlapping Bose-Einstein Condensates by Sympathetic Cooling", Physical Review Letters **78**, 586–589 (1997) (cited on page 66).

[179]G. Modugno, G. Ferrari, G. Roati, R. J. Brecha, A. Simoni, and M. Inguscio, "Bose-Einstein Condensation of Potassium Atoms by Sympathetic Cooling", Science **294**, 1320 (2001) (cited on page 66).

[180]M. Melchner von Dydiowa, "An optical dipole trap for ultracold atomic gases", Master's thesis (ETH Zurich and University of Cambridge, Cambridge, UK, Apr. 2017) (cited on page 66).

[181] Hamamatsu, "Si photodiodes", Handbook on phododiodes, url (2018) (cited on page 66).

[182]Z. Hadzibabic, S. Gupta, C. A. Stan, C. H. Schunck, M. W. Zwierlein, K. Dieckmann, and W. Ketterle, "Fiftyfold Improvement in the Number of Quantum Degenerate Fermionic Atoms", Phys. Rev. Lett. **91**, 160401 (2003) (cited on page 68).

[183]I. Bloch, W. Zwerger, and J. Dalibard, "Many-body physics with ultracold gases", Reviews of Modern Physics **80**, 885–964 (2008) (cited on pages 69–70).

[184]L. D. Landau, and E. M. Lifshitz, *Quantum mechanics: non-relativistic theory*, 3rd ed., rev. and enl., repr. 1991 with corrections, Course of theoretical physics v. 3 (Butterworth-Heinemann, Oxford, Boston, 1991) (cited on page 69).

[185]R. J. Fletcher, J. Man, R. Lopes, P. Christodoulou, J. Schmitt, M. Sohmen, N. Navon, R. P. Smith, and Z. Hadzibabic, "Elliptic flow in a strongly interacting normal Bose gas", Physical Review A **98**, 011601 (2018) (cited on page 70).

[186]L. P. Pitaevskii, and S. Stringari, *Bose-Einstein condensation*, International series of monographs on physics 116 (Clarendon Press, Oxford, 2003) (cited on pages 70–72).

[187]N. Tammuz, R. P. Smith, R. L. D. Campbell, S. Beattie, S. Moulder, J. Dalibard, and Z. Hadzibabic, "Can a Bose Gas Be Saturated?", Physical Review Letters **106**, 230401 (2011) (cited on page 72).

[188]N. W. Ashcroft, and N. D. Mermin, *Solid state physics* (Brooks/Cole, Thomson Learning, London, 1976) (cited on pages 73, 75).

[189]M. Greiner, "Ultracold quantum gases in three-dimensional optical lattice potentials", LMU Munich, url (2003) (cited on page 73).

[190]C. Weitenberg, M. Endres, J. F. Sherson, M. Cheneau, P. Schauß, T. Fukuhara, I. Bloch, and S. Kuhr, "Single-spin addressing in an atomic Mott insulator", Nature **471**, 319–324 (2011) (cited on pages 77, 97).

[191]P. M. Preiss, M. Ruichao, M. E. Tai, A. Lukin, M. Rispoli, P. Zupancic, Y. Lahini, R. Islam, and M. Greiner, "Strongly correlated quantum walks in optical lattices", Science **347**, 1229–1233 (2015) (cited on pages 77, 97).

[192]S. Fölling, S. Trotzky, P. Cheinet, M. Feld, R. Saers, A. Widera, T. Müller, and I. Bloch, "Direct observation of second-order atom tunnelling", Nature **448**, 1029–1032 (2007) (cited on page 82).

[193]N. Goldman, and J. Dalibard, "Periodically Driven Quantum Systems: Effective Hamiltonians and Engineered Gauge Fields", Physical Review X **4**, 031027 (2014) (cited on page 82).

[194] J. Struck, C. Olschlager, R. Le Targat, P. Soltan-Panahi, A. Eckardt, M. Lewenstein, P. Windpassinger, and K. Sengstock, "Quantum Simulation of Frustrated Classical Magnetism in Triangular Optical Lattices", Science **333**, 996–999 (2011) (cited on page 82).

[195] R. Desbuquois, M. Messer, F. Görg, K. Sandholzer, G. Jotzu, and T. Esslinger, "Controlling the Floquet state population and observing micromotion in a periodically driven two-body quantum system", Physical Review A **96**, 053602 (2017) (cited on page 82).

[196] M. Reitter, J. Näger, K. Wintersperger, C. Sträter, I. Bloch, A. Eckardt, and U. Schneider, "Interaction Dependent Heating and Atom Loss in a Periodically Driven Optical Lattice", Physical Review Letters **119**, 200402 (2017) (cited on page 82).

[197] J. Näger, K. Wintersperger, M. Bukov, S. Lellouch, E. Demler, U. Schneider, I. Bloch, N. Goldman, and M. Aidelsburger, "Parametric instabilities of interacting bosons in periodically-driven 1d optical lattices", arXiv:1808.07462 (2018) (cited on page 82).

[198] A. Jagannathan, and M. Duneau, "An eightfold optical quasicrystal with cold atoms", EPL (Europhysics Letters) **104**, 66003 (2013) (cited on page 84).

[199] A. Jagannathan, and M. Duneau, "The eight-fold way for optical quasicrystals", The European Physical Journal B **87** (2014) 10.1140/epjb/e2014-50164-7 (cited on page 84).

[200] A. Jagannathan, and M. Duneau, "Tight-Binding Models in a Quasiperiodic Optical Lattice", Acta Physica Polonica A **126**, 490–492 (2014) (cited on page 84).

[201] J. J. Snyder, "Paraxial ray analysis of a cat's-eye retroreflector", Applied optics **14**, 1825–1828 (1975) (cited on page 88).

[202] P. L. Gould, G. A. Ruff, and D. E. Pritchard, "Diffraction of atoms by light: The near-resonant Kapitza-Dirac effect", Physical review letters **56**, 827 (1986) (cited on pages 89, 91).

[203] P. L. Kapitza, and P. A. M. Dirac, "The reflection of electrons from standing light waves", Mathematical Proceedings of the Cambridge Philosophical Society **29**, 297 (1933) (cited on page 91).

[204] N. J. A. Sloane, and S. Plouffe, *The encyclopedia of integer sequences* (San Diego, Calif., 1995) (cited on page 93).

[205] B. Gadway, "Atom-optics approach to studying transport phenomena", Physical Review A **92**, 043606 (2015) (cited on pages 94, 97).

[206] S. Gupta, E. Leanhardt, A. Cronin, and D. E. Pritchard, "Coherent manipulation of atoms with standing light waves", C. R. Acad. Sci. Paris **t. 2**, 479–495 (2001) (cited on page 94).

[207] A. P. Chikkatur, A. Görlitz, D. M. Stamper-Kurn, S. Inouye, S. Gupta, and W. Ketterle, "Suppression and enhancement of impurity scattering in a Bose-Einstein condensate", Physical review letters **85**, 483 (2000) (cited on page 95).

[208] M. Greiner, I. Bloch, O. Mandel, T. Hänsch, and T. Esslinger, "Exploring Phase Coherence in a 2d Lattice of Bose-Einstein Condensates", Physical Review Letters **87**, 160405 (2001) (cited on page 95).

[209] J. H. Denschlag, J. E. Simsarian, H Häffner, C McKenzie, A Browaeys, D Cho, K Helmerson, S. L. Rolston, and W. D. Phillips, "A Bose-Einstein condensate in an optical lattice", Journal of Physics B: Atomic, Molecular and Optical Physics **35**, 3095–3110 (2002) (cited on page 102).

[210] M. Atala, M. Aidelsburger, J. T. Barreiro, D. Abanin, T. Kitagawa, E. Demler, and I. Bloch, "Direct measurement of the Zak phase in topological Bloch bands", Nature Physics **9**, 795–800 (2013) (cited on page 102).

[211] G. Jotzu, M. Messer, R. Desbuquois, M. Lebrat, T. Uehlinger, D. Greif, and T. Esslinger, "Experimental realization of the topological Haldane model with ultracold fermions", Nature **515**, 237–240 (2014) (cited on page 102).

[212] L. Duca, T. Li, M. Reitter, I. Bloch, M. Schleier-Smith, and U. Schneider, "An Aharonov-Bohm interferometer for determining Bloch band topology", Science, 1259052 (2014) (cited on page 102).

[213] C. D'Errico, E. Lucioni, L. Tanzi, L. Gori, G. Roux, I. P. McCulloch, T. Giamarchi, M. Inguscio, and G. Modugno, "Observation of a Disordered Bosonic Insulator from Weak to Strong Interactions", Physical Review Letters **113** (2014) 10.1103/PhysRevLett.113.095301 (cited on page 103).

[214] A. M. Rey, I. I. Satija, and C. W. Clark, "Quantum coherence of hard-core bosons: Extended, glassy, and Mott phases", Physical Review A **73** (2006) 10.1103/PhysRevA.73.063610 (cited on page 103).